Detection and Alignment of Vascular Structures in Intravascular Ultrasound using Pattern Recognition Techniques

Marina Alberti

Detection and Alignment of Vascular Structures in Intravascular Ultrasound using Pattern Recognition Techniques

A dissertation submitted by **Marina Alberti** at Universitat de Barcelona to fulfill the degree of **PhD in Applied Mathematics**.

Barcelona, February 2013

Directors	**Dr. Simone Balocco and Dr. Petia Radeva** Dept. Matemática Aplicada i Análisi, Universitat de Barcelona Centre de Visió per Computador
Thesis Committee	**Dr. Miguel Angel González Ballester** Alma IT Systems **Dr. Amin Katouzian** Technical University of Munich **Dr. Laura Igual Muñoz** Dept. Matemática Aplicada i Análisi, Universitat de Barcelona

This document was typeset by the author using LaTeX 2_ε.

The research described in this book was carried out at the University of Barcelona and the Computer Vision Center.

To my family.

Acknowledgements

The research work presented in this thesis is the outcome of a long process of hard work and knowledge sharing, through which I had the opportunity to meet and collaborate with a number of kind and extraordinary people.

First of all, I would like to thank my supervisors, Dr. Simone Balocco and Dr. Petia Radeva. Thanks to Petia for her great support and advice. My thanks to Simone for his guidance, patience and faith that made this work possible.

Thanks to the physicians of the Hospital "Germans Trias i Pujol", for helping me in understanding the clinical challenges in our field and for their hard work that provided us with ideas, data and manual annotations. Thanks to Dr. Juan Rigla from Boston Scientific for sharing his views and knowledgeable suggestions on IVUS. I would like to thank Joana Silva from the Coimbra University Hospital, Portugal, for her valuable help and for sharing with me her motivation at the very beginning of my research.

I would also like to thank all the members of the IVUS team at the University of Barcelona and Computer Vision Center. Thanks to Carlo for supervising me during the initial phase of my PhD. Thanks to Francesco for helping me with his comments and suggestions throughout this period.

My thanks to the colleagues at University of Barcelona and Computer Vision Center for their nice company. I will always remember these days.

Allow me this opportunity to thank all the University of Barcelona and Computer Vision Center administrative staff, for helping me with bureaucratic work and allowing me to concentrate on my research.

Finally, my thanks and respect to my family that allowed me to come here and always supported me. Thanks to my parents and my sister Chiara for being always there even from far away. My special thanks to Bhaskar for his love and support and for teaching me so many things.

Abstract

In this thesis, several methods for the automatic analysis of Intravascular Ultrasound (IVUS) sequences are presented, aimed at assisting physicians in the diagnosis, the assessment of the intervention and the monitoring of the patients with coronary disease. The basis for the developed frameworks are machine learning, pattern recognition and image processing techniques.

First, a novel approach for the automatic detection of vascular bifurcations in IVUS is presented. The task is addressed as a binary classification problem (identifying bifurcation and non-bifurcation *angular sectors* in the sequence images). The multiscale stacked sequential learning algorithm is applied, to take into account the spatial and temporal context in IVUS sequences, and the results are refined using *a-priori* information about branching dimensions and geometry. The achieved performance is comparable to intra- and inter-observer variability.

Then, we propose a novel method for the automatic non-rigid alignment of IVUS sequences of the same patient, acquired at different moments (before and after percutaneous coronary intervention, or at baseline and follow-up examinations). The method is based on the description of the morphological content of the vessel, obtained by extracting temporal morphological profiles from the IVUS acquisitions, by means of methods for segmentation, characterization and detection in IVUS. A technique for non-rigid sequence alignment - the Dynamic Time Warping algorithm - is applied to the profiles and adapted to the specific clinical problem. Two different robust strategies are proposed to address the partial overlapping between frames of corresponding sequences, and a regularization term is introduced to compensate for possible errors in the profile extraction. The benefits of the proposed strategy are demonstrated by extensive validation on synthetic and *in-vivo* data. The results show the interest of the proposed *non-linear* alignment and the clinical value of the method.

Finally, a novel automatic approach for the extraction of the luminal border in IVUS images is presented. The method applies the multiscale stacked sequential learning algorithm and extends it to 2-D+T, in a first classification phase (the identification of lumen and non-lumen regions of the images), while an active contour model is used in a second phase, to identify the lumen contour. The method is extended to the longitudinal dimension of the sequences and it is validated on a challenging data-set.

Resumen

En esta tesis, se presentan varios métodos para el análisis automático de secuencias de Ultrasonido Intravascular (IVUS), destinados a ayudar a los médicos en el diagnóstico, la evaluación de la intervención y el seguimiento de los pacientes con enfermedad coronaria. La base para los métodos desarrollados son técnicas de aprendizaje automático, reconocimiento de patrones y procesamiento de imagen.

En primer lugar, se presenta un nuevo método para la detección automática de las bifurcaciones vasculares en IVUS. La tarea se aborda como un problema de clasificación binaria (identificando los sectores angulares de bifurcación y de no-bifurcación en las imágenes de la secuencia). Se aplica el algoritmo de multiscale stacked sequential learning, para tener en cuenta el contexto espacial y temporal de las secuencias de IVUS, y los resultados se refinan utilizando información a priori acerca de las dimensiones de las ramificaciones y su geometría. El rendimiento obtenido es comparable es comparable a la variabilidad intra- e inter-observador.

A continuación, se propone un nuevo método para la alineación automática no rígida de secuencias de ecografía intravascular del mismo paciente, adquiridas en diferentes momentos (antes y después de la intervención coronaria, o al inicio del estudio y en exámenes de seguimiento). El método se basa en la descripción del contenido morfológico del vaso, que se obtiene mediante la extracción de perfiles temporales morfológicos de las adquisiciones de IVUS, por medio de métodos para la segmentación, caracterización y detección en IVUS. Una técnica para la alineación no rígida de secuencias - el algoritmo de Dynamic Time Warping - se aplica a los perfiles y se adapta al problema clínico específico. Se proponen dos diferentes estrategias robustas para hacer frente a la superposición parcial entre los frame de las secuencias correspondientes, y se introduce un término de regularización, para compensar por posibles errores en la extracción de los perfiles. Los beneficios de la estrategia propuesta se demuestran por una amplia validación en datos sintéticos e in vivo. Los resultados mostran el interés de la alineación no lineal propuesta y el valor clínico del método.

Finalmente, se presenta un enfoque novedoso para la extracción automática de la frontera luminal en imágenes de IVUS. El método aplica el algoritmo de aprendizaje multiscale stacked sequential learning y lo extiende en 2-D+T, en una primera fase de clasificación (la identificación de regiones de lumen y no-lumen de las imágenes), mientras que un modelo de contorno activo se utiliza en una segunda fase, para identificar el contorno luminal. El método se extiende a la dimensión longitudinal de las secuencias y se valida en un conjunto de datos desafiante.

Resum

En aquesta tesi, es presenten diversos mètodes per a l'anàlisi automàtic de seqüències de Ultrasò Intravascular (IVUS), destinats a ajudar els metges en el diagnòstic, l'avaluació de la intervenció i el seguiment dels pacients amb malaltia coronària. La base per als marcs desenvolupats són tècniques de aprenentatge automàtic, reconeixement de patrons i processament d'imatge.

En primer lloc, es presenta un nou mètode per a la detecció automàtica de les bifurcacions vasculars en IVUS. La tasca s'aborda com un problema de classificació binària (identificant els sectors angulars de bifurcació i no-bifurcació en les imatges de la seqüència). S'aplica l'algorisme de aprendizaje de multiscale stacked sequential learning, per tenir en compte el context espacial i temporal de seqüències de IVUS, i els resultats es refinen utilitzant informació a priori sobre les dimensions i la geometria de les ramificacions. El rendiment obtingut és comparable a la variabilitat intra- i inter-observador.

A continuació, es proposa un nou mètode per a la alineació automàtica no rígida de seqüències de ecografia intravascular del mateix pacient, adquirits en diferents moments (abans i després de la intervenció coronària, o a l'inici de l'estudi i en els exàmens de seguiment). El mètode es basa en la descripció del contingut morfològic del vas, que s'obté mitjançant l'extracció de perfils temporals morfològiques de les adquisicions de IVUS, per mitjà de mètodes per a la segmentació, caracterització i detecció en IVUS. Una tècnica per l'alineació no rígid de seqüències - l'algoritme de Dynamic Time Warping - s'aplica als perfils i s'adapta al problema clínic específic. Es proposen dos diferents estratègies sòlides per fer front a la superposició parcial entre els frame de les seqüències corresponents, i s'introdueix un terme de regularització, per compensar per possibles errors en l'extracció dels perfils. Els beneficis de l'estratègia proposada es demostran per una àmplia validació en dades sintètiques i in vivo. Els resultats mostran l'interès de la alineació no lineal proposta i el valor clínic del mètode.

Finalment, es presenta un enfocament nou per a l'extracció automàtica de la frontera luminal en imatges de IVUS. El mètode aplica el algorisme d'aprenentatge multiscale stacked sequential learning i l'estén a 2-D+T, en una primera fase de classificació (la identificació de regions de lumen i no-lumen de les imatges), mentre que un model de contorn actiu s'utilitza en una segona fase, per identificar el contorn luminal. El mètode s'estén a la dimensió longitudinal de les seqüències i es valida en un conjunt de dades desafiador.

Contents

List of Tables

List of Figures

Chapter 1

Introduction

In the last decades, the technological advances have made numerous and sophisticated image acquisition modalities available to physicians. The interior of the human body can be captured and the information can be stored in the form of digital images. Medical image analysis is the study of such digital images, performed using computational tools, aimed at facilitating measurement and visualization. Medical imaging assists the diagnosis, the planning, guidance and evaluation of interventions and the monitoring of the patient recovery.

The currently available imaging modalities can be divided into two categories: anatomical and functional. Anatomical modalities, i.e., depicting morphology, include X-ray, Computed Tomography (CT), Magnetic Resonance Imaging (MRI) and Ultrasound (US). Functional modalities, i.e., depicting information on the metabolism of the underlying anatomy, include scintigraphy, Single-Photon Emission Computed Tomography (SPECT), Positron Emission Tomography (PET) and functional MRI (fMRI).

In this thesis, we are focusing on developing methods to assist physicians in the treatment of coronary disease by using Intravascular Ultrasound (IVUS) images. IVUS is a catheter-based imaging technique that provides accurate tomographic images of vascular structures. This goal is achieved by using machine learning, pattern recognition and image processing techniques that will be described in the following chapters.

In this first chapter, coronary disease and coronary interventional procedures will be described. Then, the role of IVUS in the diagnosis, intervention and monitoring of the patients with coronary disease will be explained and the challenges in IVUS image analysis will be posed. Finally, the contributions of this thesis and the thesis structure will be described. Please note that in the thesis we will introduce several medical imaging terms that are summarized in the glossary in Appendix A.

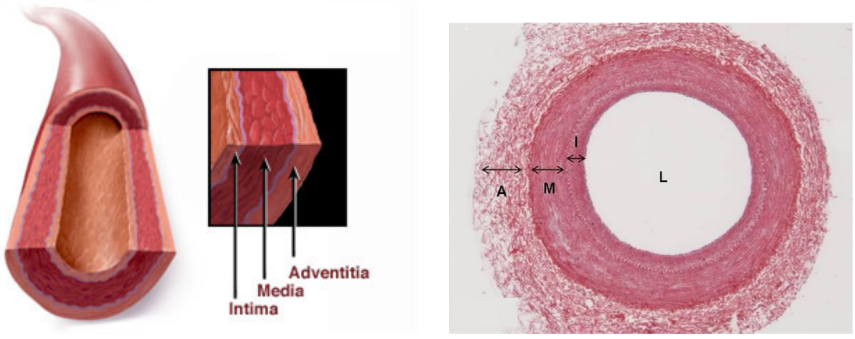

(a) (b)

Figure 1.1: The structure of the coronary artery. (a) Scheme representing the intima, media and adventitia layers in a cross-sectional view of the artery and (b) histology slide from a post-mortem coronary artery, indicating the lumen region (L) and the intima (I), media (M) and adventitia (A) layers.

1.1 Medical Context

The structure of healthy coronary arteries and the evolution of the atherosclerotic disease will be first introduced. Then, IVUS images from diseased coronary arteries will be analyzed.

1.1.1 Coronary Circulation

The coronary arteries are the vessels providing blood to the heart muscle (myocardium). The three main vessels that deliver oxygen-rich blood to the myocardium are the Left anterior descending, Left Circumflex, and Right coronary arteries, and they originate from the left side of the heart, at the beginning of the aorta.

The structure of coronary arteries is composed of three stratifications: the inner layer (tunica intima or intima), the muscular layer (tunica media or media) and the outer layer (tunica adventitia or adventitia), as illustrated in Figure 1.1. The cavity within the vessel, in which the blood flows, is called the lumen (see Figure 1.1(b)). The tunica intima, in direct contact with the blood, is lined by the endothelium, a layer composed of simple squamous epithelial cells. The endothelium forms a flat slick surface inside the vessel, minimizing the friction with the blood. The tunica media, which separates the intima from the adventitia, is composed of smooth muscle cells and elastic tissue and it is characterized by a low collagen content. The tunica adventitia is mainly composed of loose collagen and elastic tissue.

The structure of the coronary tree is characterized by vascular bifurcations, which can be defined as the sites where an artery diverges into two daughter vessels: the main branch and the side branch.

1.1.2 Coronary Disease

The coronary arteries can be affected by coronary artery disease (CAD), also called coronary heart disease, which is the leading cause of mortality and morbidity in the developed countries [90]. CAD results from a complex process known as atherosclerosis, a chronic progressive condition evolving toward the formation of multiple plaques inside the vessel wall.

Atherosclerosis starts with the pathological process of inflammation, leading to endothelial activation and monocyte recruitment [44]. As a result, the endothelium becomes damaged (see Figure 1.2(a)), allowing cholesterol and other cellular waste products to accumulate in the inner layer of the arterial wall. The lipid deposits are mainly localized in large and medium-sized coronary arteries, and are usually focal and irregularly distributed. These deposits eventually evolve into fibrosis and calcification. The formation of atherosclerotic plaque results from the proliferation and successive destruction of intimal fibrosis tissue, leading to the formation of an atheroma, i.e., a thickening of the intimal-medial segments and an overall thickening of the vessel wall.

The atherosclerotic condition causes a narrowing of the arterial lumen, which restricts the blood and oxygen flow to the heart and is the main cause of the chronic ischemic manifestation of coronary heart disease. Moreover, plaques containing a soft atheromatous core are unstable and may rupture [26, 36], i.e., the fibrous cap (represented in Figure 1.2(a)) which separates the core from the lumen may disintegrate, so that the highly thrombogenic gruel is suddenly exposed to the flowing blood. Such disrupted plaques are the main responsible for the acute coronary syndromes of unstable angina, myocardial infarction, and sudden death [34].

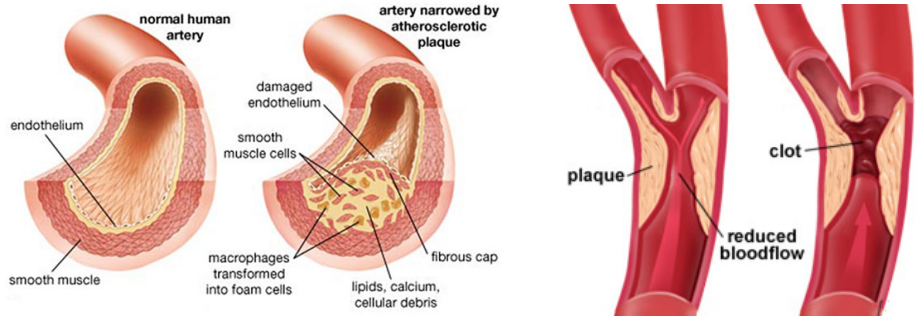

(a) (b)

Figure 1.2: (a) Atherosclerosis progression: healthy artery (left) and artery narrowed by atherosclerotic plaque (right). (b) Vascular bifurcation are critical locations for plaque growth.

Bifurcations are critical vascular locations from the clinical point of view, since they are typical sites for atherosclerotic lesions. Wall thickenings and plaque formation in coronary arteries are frequently localized on the outer wall of one or both daughter vessels at major bifurcations [4], as illustrated in Figure 1.2(b). Moreover, the rupture

of vulnerable plaque may depend on anatomic parameters such as the proximity of bifurcations. In particular, the presence of a bifurcation before and especially after the lesion is a marker of an increased risk of plaque rupture and subsequent thrombosis [53].

1.1.3 Percutaneous Coronary Intervention (PCI)

The process of lumen narrowing, described in the previous section, can be treated by intervention. Percutaneous coronary intervention (PCI), commonly known as coronary angioplasty, is a non-surgical procedure used to open narrowed or blocked arteries to improve blood flow. PCI is an alternative to a pharmacological treatment and to major surgery. The PCI procedure involves the cardiac catheterization of the patient. PCI can be performed during a diagnostic catheterization, if a blockage is identified, or it may be scheduled, after a previous catheterization has confirmed the presence of coronary artery disease. Different types of interventional procedures are commonly performed: balloon angioplasty, stent deployment, roto-ablation and cutting balloon.

- **Balloon angioplasty** (also called PCI or Percutaneous Transluminal Coronary Angioplasty (PTCA)): a small balloon at the tip of the catheter is inserted near the blocked or narrowed area of the coronary artery. When the balloon is inflated, the fatty plaque or blockage is compressed against the artery walls and the diameter of the blood vessel is dilated to increase blood flow. This procedure is sometimes complicated by restenosis, i.e., the recurrence of the vessel narrowing.

- **PCI with stenting**: in most cases, balloon angioplasty is performed in combination with the stenting procedure. A stent is a (metal or bio-absorbable) mesh tube that acts as a scaffold inside the coronary artery. A balloon catheter, placed over a guide wire, is used to insert the stent into the narrowed artery. Once in place, the balloon is inflated and the stent expands to the size of the artery and holds it open. The balloon is then deflated and removed in such a way that the stent stays in place permanently.

- **Roto-ablation** (also called Percutaneous Transluminal Rotational Atherectomy or PTRA): a special catheter, with an acorn-shaped, diamond-coated tip, is guided to the point of a narrowing in the coronary artery. The tip spins around at a high speed and grinds away the plaque on the arterial walls.

- **Cutting balloon**: the cutting balloon catheter has a balloon tip with blades. When the balloon is inflated, the blades are activated and score the plaque. Then, the balloon compresses the fatty matter into the arterial wall. This type of balloon may be used to treat the build up of plaque within a previously placed stent (restenosis).

1.2 IVUS

To capture images of the different phases of the percutaneous intervention, angiography was the only imaging modality used until recent years. Angiography is considered as the *gold standard* imaging technique for coronary artery disease, used to detect arterial lesions, to guide percutaneous intervention and to communicate among interventionalists and surgeons. However, angiography has limitations for a precise lumen measurement due to its projective nature, and often fails to detect those lesions prone to thrombosis [98].

In the last decades, IVUS has evolved as a valuable supplement to the angiographic inspection. IVUS is a catheter-based imaging modality that provides high-resolution tomographic images of vascular structures. The procedure for acquiring an IVUS sequence consists in inserting an ultrasonic probe, carried by a catheter, into the arterial vessel. The rotating transducer emits an ultrasound beam, as it is dragged from the proximal to the distal position (pullback), at constant speed, by means of a motorized tool. A sequence of frames is acquired. The procedure is schematized in Figure 1.3.

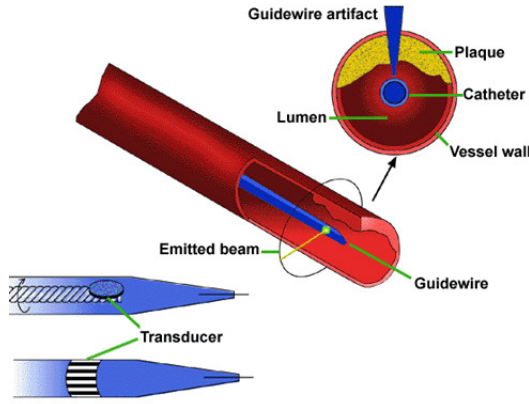

Figure 1.3: Schematic example of the IVUS acquisition procedure (adapted from Kimura *et al.*, Am Heart J, 1995).

The standard IVUS frame is a 360-degree cross-sectional view of the vessel walls, denoted as *short-axis view*, which allows an accurate assessment of vessel morphology and tissue composition [19]. *Longitudinal views* of the sequence can be generated by considering the gray-level values of the sequence along the diameter at a chosen angle. A *longitudinal view* approximates the morphology of the vessel section according to the selected scan orientation. Figure 1.4 shows three IVUS frames, characterized by the presence of vascular bifurcation, plaque, and stent, respectively, and a *longitudinal view* of the sequence, where the frame positions are indicated by vertical lines.

Unlike angiography, which depicts a silhouette of the coronary lumen, IVUS displays tomographic, cross-sectional perspective. This facilitates direct measurements of lumen dimensions, including minimum and maximum diameter and cross-sectional

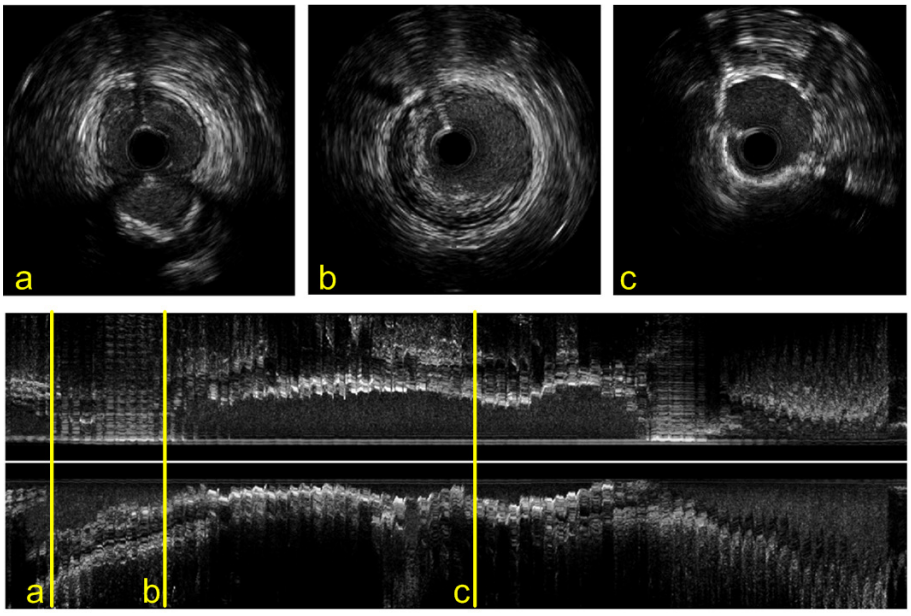

Figure 1.4: Three *short-axis views* of an IVUS sequence, showing (a) bifurcation, (b) plaque and (c) implanted stent, respectively, and a *longitudinal view* of the sequence where the longitudinal location of the three frames is indicated by vertical lines.

area, as well as the characterization of atheroma size, plaque distribution and composition.

IVUS is an important tool for pre/post-intervention and baseline/follow-up analysis. In the clinical practice, IVUS is used for diagnosis to analyze the vessel condition, locate the lesions and their composition and decide on the procedure (stent deployment or pharmacological treatment). During PCI, IVUS acquisitions are performed at pre- and post-intervention. Before the intervention, IVUS can be useful for locating the target lesion and deciding the size and type of the stent to be deployed. After the intervention, a second IVUS sequence allows to evaluate the interventional outcome, to assess blood flow restoration and stent apposition (detecting stent malapposition, stent underexpansion, side-branch occlusion by deployed stent) [69]. Furthermore, IVUS is an effective tool to monitor the status of the disease over the time, in follow-up exams and in clinical research studies. In particular, IVUS is useful to assess regression or progression of atherosclerosis, to identify the evolution of plaque composition, and to monitor restenosis [58].

1.2.1 Challenges in IVUS

Although IVUS is a sophisticated and powerful imaging modality, it is not immune from obstacles. The application of pattern recognition, image processing and machine

learning techniques to automatically analyze IVUS sequences is challenging, because several artifacts hinder the automated IVUS analysis.

The ultrasound beam may be reflected by the guidewire and may result in bright echoes and shadows in the IVUS images. The catheter produces a circular bright artifact known as the "ring-down" effect. Calcifications cause shadows, which hide the vessel morphology. Speckle noise is present. In Figure 1.5, these artifacts are indicated, along with several vessel structures of interest.

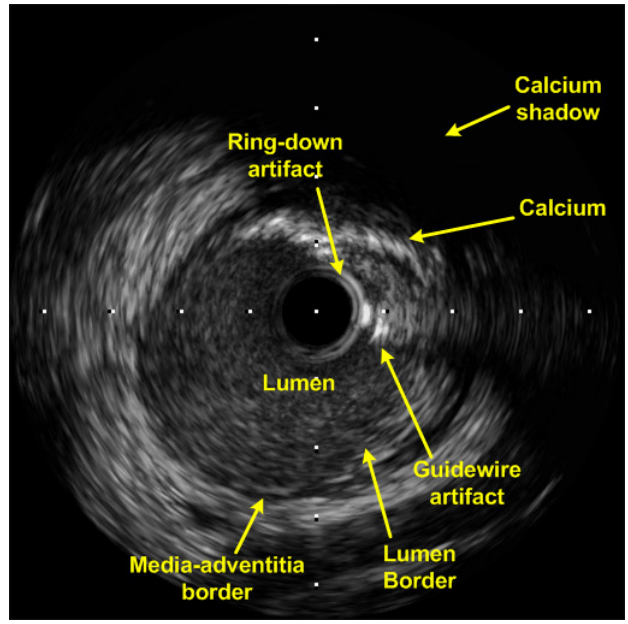

Figure 1.5: Example of IVUS image, where several structures and artifacts are indicated.

Additionally, the catheter movement and the arterial pulsation cause dynamic artifacts. The longitudinal movement of the transducer is affected by a continuous oscillatory movement, causing the same positions in the vessel to be sampled multiple times (see Figure 1.6(a)). The position of the catheter is not fixed with respect to the vessel morphology in the plane orthogonal to vessel (*short-axis*). The rotation of the probe varies with vessel pulsation, therefore successive frames can be axially rotated, resulting in a misalignment (vessel roto-translation), as illustrated in Figure 1.6(a). The catheter may follow different trajectories with respect to the vessel walls (see Figure 1.6(b)), hence the imaged sections are not necessarily orthogonal to the vessel walls. The catheter flexibility causes non-rigid deformations of the pullbacks.

Due to these artifacts, the automatic characterization of IVUS sequences with morphological and pathological information is challenging. The automatic extraction of the vessel boundaries, in particular the lumen and the media-adventitia borders, is useful to evaluate the blood flow and the plaque burden, since plaque is localized

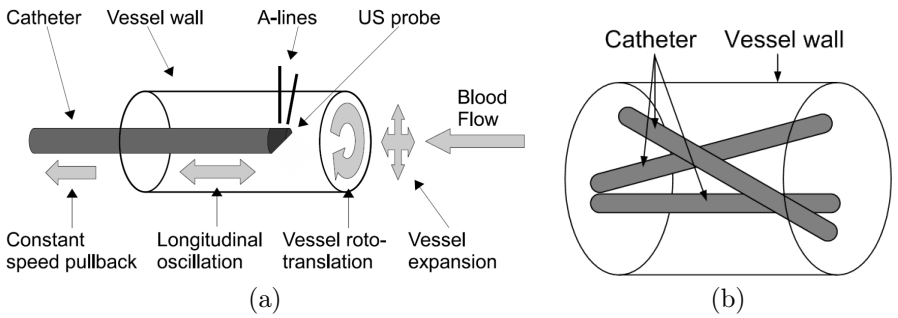

Figure 1.6: (a) Scheme of an IVUS acquisition set-up, where the artifacts due to motion are reported (image from Ciompi *et al.*, 2010 [19]). (b) Schematic showing different possible catheter trajectories.

between luminal and media-adventitia borders. The automatic and semi-automatic segmentation of the luminal border in IVUS has been thoroughly studied in the literature, but it is still an open problem [50], because it is difficult to develop a method robust to different artifacts, clinical conditions, and catheter probes. The detection of vascular bifurcations has never been addressed in IVUS literature before the study presented in this thesis, although the same topic has been investigated in other imaging modalities [123, 117, 56, 67]. Finally, an important aspect, both in clinical practice and clinical research studies, is the temporal comparison of IVUS sequences. This comparison requires the alignment, i.e., the identification of the same vessel sections in different acquisitions. In clinical trials for plaque regression/progression, even when using clear landmarks and identical conditions of the pullbacks during the baseline and follow-up acquisitions, the pullback lengths in terms of number of frames will not be identical in the majority of cases, due to the aforementioned dynamic artifacts [58]. For accurate measurements, corresponding frames are identified manually, by checking the sequences frame by frame.

1.3 Brief Overview of the Thesis

The aim of this thesis is to develop automatic methods that assist physicians in the diagnosis, the evaluation of coronary intervention and the monitoring of the patients, using IVUS images. In this thesis, two approaches for the automatic characterization of the vessel morphology are proposed: a method for the extraction of the lumen border and a method for the detection of vascular bifurcations (identifying their position and extension). On top of these methods, a framework for the automatic alignment of IVUS sequences is proposed, with the goal of identifying the corresponding vessel sections and allowing the comparison of pre/post-intervention and baseline/follow-up cases. The approaches are based on pattern recognition, machine learning and image processing techniques and are validated on *in-vivo* data-sets.

1.4 Contributions

As discussed in the previous section, we contribute to the literature by presenting three methods that overcome the challenges in IVUS described earlier in this chapter.

Automatic Bifurcation Detection

- A fully automatic method for the detection of vascular bifurcations in IVUS is proposed for the first time. The method identifies every bifurcation in an IVUS sequence, the corresponding frames, the angular orientation with respect to the IVUS acquisition, and the extension.
- This goal is reached using the multi scale stacked sequential learning scheme [38]. The results are then successively refined using *a-priori* information about branching dimensions and geometry.
- The method is validated on *in-vivo* sequences and the performance is compared to inter- and intra-observer variabilities.
- A new visualization map for IVUS sequences is presented, summarizing the vessel characteristics in a compact representation.

Automatic Non-rigid Temporal Alignment

- An automatic approach for IVUS alignment, based on the Dynamic Time Warping (DTW) technique [94], is proposed for the first time.
- The non-rigid alignment algorithm is adapted to the specific IVUS alignment task by applying it to multidimensional temporal signals describing the morphological content of the vessel.
- A DTW-based approach is specifically tailored for the clinical task: DTW is embedded into a framework comprising a strategy to address partial overlapping between acquisitions, and a term to regularize non-physiological temporal compression/expansion of the sequences.
- Extensive validation is performed on both synthetic and *in-vivo* data.
- A thoroughly automatic workflow for IVUS sequence alignment is presented, potentially applicable to other image modalities.
- A novel strategy for multidimensional sequence alignment, robust to partial overlapping, is proposed, which can be used in a wider range of alignment problems.

Automatic 2-D+T Lumen Border Extraction

- A method for automatic extraction of the luminal border in IVUS images is presented.
- The multi-scale stacked sequential learning scheme [38] is applied and extended to the three dimensions of an IVUS sequence, including the temporal (longitudinal) dimension. After classification, an active contour model is applied to the binary classification map.
- Validation is performed on data-sets from different echographs.
- The results are qualitatively compared to *state-of-the-art* approaches for lumen segmentation in IVUS.

1.5 Thesis Structure

The thesis is organized as follows:

- Chapter 2 presents an overview of available methods related to the IVUS technology in medical imaging. The IVUS technology is divided into three main areas: IVUS image acquisition techniques, compensation of artifacts due to catheter and heart motion, and methods for automatic IVUS analysis, performed using computer vision techniques.
- Chapter 3 presents the method for automatic bifurcation detection in IVUS sequences.
- Chapter 4 introduces the purpose and the challenges of the temporal alignment of IVUS sequences. The proposed automatic non-rigid alignment method is presented and validated by using both synthetic and *in-vivo* data.
- Chapter 5 describes the proposed method for luminal border extraction in IVUS sequences.
- Chapter 6 documents the conclusions and future work of the thesis.

Chapter 2

Background on the IVUS Technology in Medical Imaging

2.1 Introduction

This thesis is focusing on the automatic analysis of IVUS sequences. In this chapter, several image acquisition and analysis techniques applied to the IVUS image modality will be described.

The chapter is organized in three sections: Section 2.2 describes the image acquisition system, including the IVUS catheter, the catheter pullback device and the image formation. In Section 2.3, preprocessing methods that compensate for the dynamic artifacts due to catheter motion and heart beating are illustrated. Section 2.4 presents methods for IVUS analysis, including generic image processing and pattern recognition methods which are applied in the thesis, and the *state-of-the-art* methods for quantification in IVUS. The approaches for IVUS measurements include the available techniques for providing the lumen and media borders as well as plaque characterization. Moreover, a brief overview on bifurcation detection in medical imaging and on alignment and fusion of data acquired from coronary imaging modalities is given, with main focus on the IVUS technology. Finally, the commercial software available on the main IVUS imaging systems is described. Figure 2.1 describes the schematic of the proposed taxonomy.

2.2 IVUS Image Acquisition Techniques

Until the last decades, angiography was the only technique for planning and guidance of percutaneous interventions. The IVUS technology was developed in the mid-1980s and was first tested on human patients at the end of the 1980s. In the following years, IVUS has become increasingly important in both clinical and research applications.

Images in IVUS are acquired by means of high-frequency, single-use ultrasound probes. The probes are inserted into the vessel by a catheter, which is advanced, along with a guidewire, within the femoral artery towards the site of interest in the

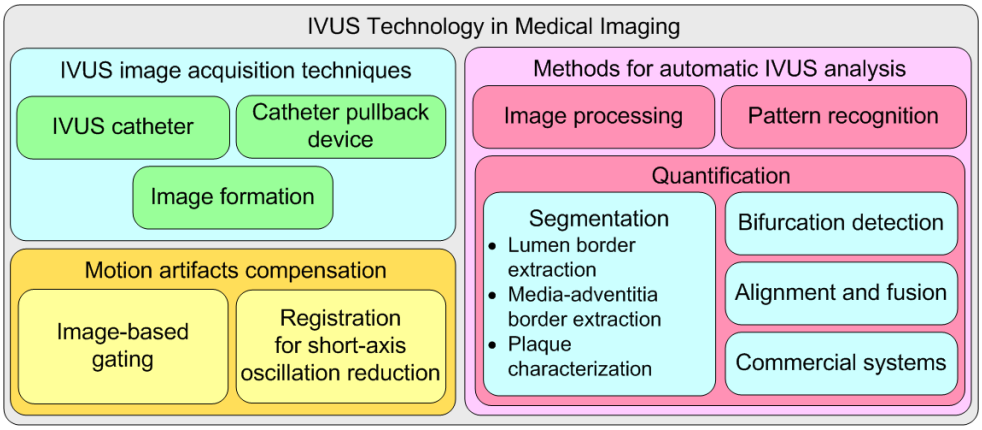

Figure 2.1: Taxonomy of the IVUS technology in medical imaging.

coronary arteries, under angiogram guidance. The catheter is 150 cm long and has a tip size of 3.2–3.5 F (1.2–1.5 mm). The IVUS catheter allows the visualization of segments of coronary arteries over 15 cm long.

Two technical approaches to IVUS catheter design have emerged in the years: (1) single-element mechanically rotating transducers and (2) multi-element phased-array transducers [33], as schematized in Figure 2.2.

The first IVUS catheter system (mechanical system) consists in a single-element mechanically rotating piezoelectric transducer that rotates at approximately 1800 revolutions/min (30 revolutions/sec) [69]. The transducer emits an ultrasound pulse and receives the back-scattered signal, at approximately 1° angular rotation increments. The time delay and amplitude of these pulses provide 256 individual radial scans for each image. An electrical connecting wire needs to pass along the side of the imaging assembly, as shown in Figure 2.2 (top). This wire produces an artifact that occupies approximately 15 degrees of the image cross-section. Ultrasound frequencies are between 12.5 and 40 MHz, although some experimental devices use up to 45 MHz. An example of this type of transducer is the Atlantis SR 40 imaging catheter produced by Boston Scientific.

The second catheter system (electronic system) is a multi-element phased-array catheter (see Figure 2.2-bottom). An electronic board controls a subset of elements that emit synchronized US waves and receive the back-scattered signal. This circular array system uses synthetic aperture processing to produce images with higher lateral resolution (i.e., resolution perpendicular to both the beam and the catheter) than single-element transducers. The used frequency for this type of catheters is in the range of 15-25 MHz. An example is the Eagle Eye Gold imaging catheter produced by Volcano.

In both single element and multi-element systems, it is possible to reconstruct the 360-degree cross-sectional representation of the inner vessel morphology. To form a transverse cross-sectional image of the vessel, the ultrasound beam is rotated at 30 revolutions/sec, leading to 30 images per second. For 20 to 40 MHz IVUS transducers,

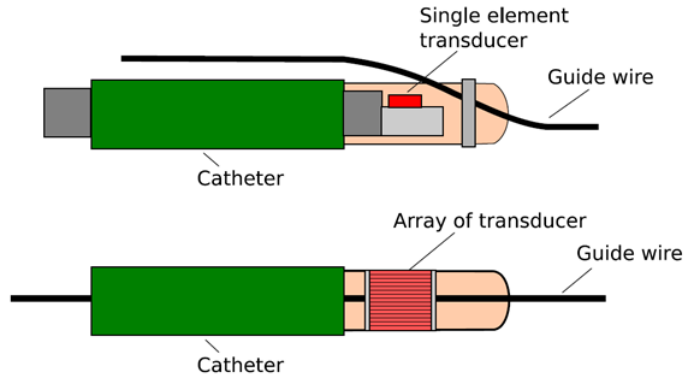

Figure 2.2: Schematic representation of IVUS catheters: single-element mechanically rotating catheter (above) and multi-element phased-array catheter (below).

the typical resolution is 80 microns axially (parallely to the beam) and 200 to 250 microns laterally (perpendicularly to both the beam and the catheter) [69]. The original domain of acquisition is polar (ρ, θ) and the resulting gray-scale image is transformed to cartesian (x, y) coordinates to reconstruct a typical IVUS frame, as shown in Figure 2.3.

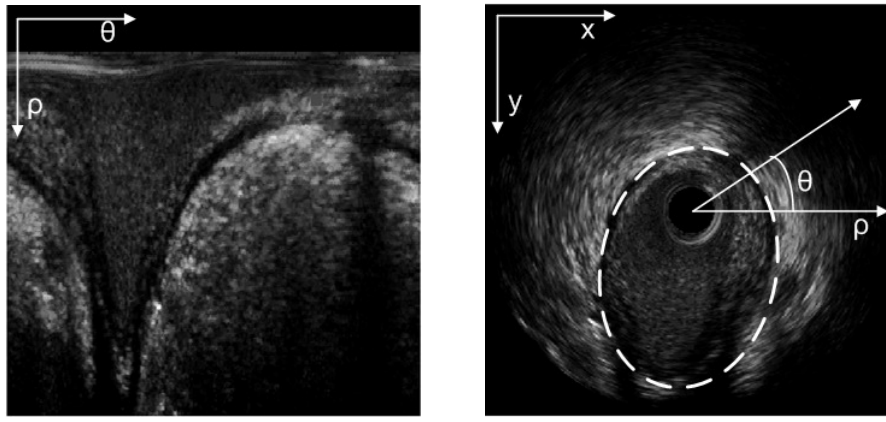

(a) (b)

Figure 2.3: IVUS frame in (a) polar and (b) cartesian representations.

The IVUS probe is connected to a pullback device and a sequence of frames are acquired while the probe is dragged. There are two approaches to the catheter pullback procedure: (1) motorized and (2) manual interrogation [69]. Important advantages of motorized interrogation include steady catheter withdrawal, that avoids imaging any segment too quickly, and the ability to concentrate on the images without having to pay attention to catheter manipulation. Motorized pullbacks permit length and volumetric measurements and provide uniform and reproducible image acquisition

for multi-center and serial studies. However, inadequate examination of important regions of interest can occur, because the transducer does not remain for long at any specific site in the vessel. In both motorized and manual pullback, the acquisition should include uninterrupted imaging of the target segment, generally including at least 10 mm of distal vessel, the lesion sites, and the proximal vessel back to the aorta. Many experts advocate that motorized transducer pullback be performed at a speed of 0.5 mm/sec. Higher pullback speeds (e.g., 1 mm/sec) have the disadvantage of imaging focal pathology too quickly, but they are commonly employed in order to minimize imaging times.

Motorized transducer pullback and digital storage of cross-sectional images allow longitudinal (*L*-mode) imaging. In an *L*-mode display, a set of "slices" are visualized, taken from a longitudinal cut through a stack of cross-sectional IVUS images. The resulting *longitudinal view* of an IVUS sequence approximates the longitudinal morphology and appearance of the artery at a given cut angle (see Figure 1.4).

2.3 Preprocessing in IVUS Pullbacks: Compensation of Motion Artifacts

During the acquisition of an IVUS sequence, the catheter is affected by several artifacts due to the catheter and heart motion, interfering with the visualization, the interpretation and the analysis of the sequence. These artifacts can be compensated by imaging techniques.

Image-based Gating The most relevant artifact is caused by the heart beating, which generates a repetitive oscillation of the catheter along the axis of the vessel (known as swinging effect), resulting in possible multiple sampling of the same vessel positions. The pullback presents an oscillation in the longitudinal direction that can be easily seen in the motorized pullback video.

In order to obtain a unique reconstruction for the transversal sections of the artery, one possible solution is the selection of the frames belonging to the same phase of the cardiac cycle, having similar rotation. Such task can be addressed by using a gating technique. The scope of gating methods is to sample evenly spaced and stable frames. The stability refers to the fact that, after the gating, in subsequent frames the vessel should have a similar position and rotation.

Gating can be performed by exploiting the electrocardiogram (ECG) signal (when it is available) [12]. However, a new promising direction in IVUS gating is to perform an image-based analysis of the pullback data and to infer optimal sampling points without considering the ECG signal. Image-based gating has the advantage of being applicable also in case of arrhythmia. Several methods have been proposed in literature.

The image-based gating algorithm presented in [126] extracts the information on the cardiac cycle by analyzing the variation, along the image sequence, of two properties computed on a region of interest (ROI). The properties are the Average Intensity of the ROI and the Absolute Intensity Difference between ROIs of subsequent frames.

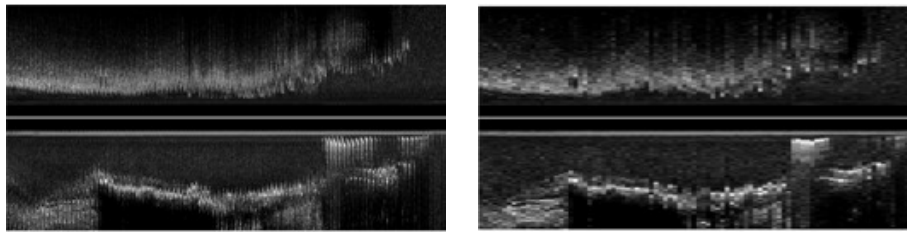

(a) (b)

Figure 2.4: Image-based gating obtained by the method proposed in Gatta *et al.*, 2010 [37]. The same *longitudinal view* is shown (a) before and (b) after the gating processing.

In [30], the authors discuss the results of their Intelligate method, showing that the method performance is comparable to an ECG gating technique.

In [81] and [82], the basic idea of the proposed image-based gating method is to introduce a dissimilarity matrix $\Phi(F_i, F_j)$ that measures the dissimilarity between the frames F_i and F_j of the same IVUS pullback, where i and j represent temporal variables. Once a proper measure is defined, such that $\Phi(F_i, F_j) \geq 0$, a matrix is obtained, that exhibits a repetitive pattern of local minima and ridges of local maxima. The pattern is repeated so that some diagonals represent the loci of local minima, thus representing a specific interval between any two frames that present minimal dissimilarity. The principal diagonal is obviously not considered since $\Phi(F_i, F_j) = 0$. The first diagonal of local minima is displaced a number of columns; this displacement is a clue for detecting the average heart beat along the sequence. To enhance the sharpness of maximal ridges, the matrix Φ is convoluted with an X-shaped inverted Gaussian kernel obtaining a matrix $\hat{D}$. Local maxima on the above defined diagonal identify couple of frames that have a high similarity and minimal inter-frame motion. Then, two algorithms are used to select the best frames in the path on the diagonal that have the highest local maxima in $\hat{D}$.

In [7], the authors propose a method to extract the cardiac phase from IVUS sequences based on the hypothesis that the oscillation of the vessel wall is visible in longitudinal cuts.

In [39], the authors modify the method in [81], to make it more robust and computationally efficient. The improved method uses a textural descriptor for each frame, and computes the dissimilarity matrix in a faster and robust way; moreover, the dynamic programming algorithm has been substituted by a local minima search in a 1-D signal obtained from the dissimilarity matrix.

In [37], a real-time gating algorithm is proposed, based on the analysis of *motion blur* variations during the cardiac cycle. The method is based on the idea that every tissue displacement causes in the image a *motion blur* proportional to the speed of the tissue movement. Figure 2.4 shows an IVUS sequence before and after gating preprocessing, by using [37].

Registration for Short-Axis Oscillation Reduction The second main dynamic artifact that affects IVUS acquisitions is the *short-axis* oscillation and deformation. The variations in the position of the catheter with respect to the center of the vessel and the catheter torsion along the pullback cause a spatial misalignment of consecutive frames. The vessel center is not aligned with the center of the image (i.e., the catheter position) and the arterial axis undergoes in-plane translations along the sequence. Moreover, the periodical rotation in the *short-axis*, due to heart beating, can cause important structures (such as plaques) to appear and disappear periodically in the longitudinal cut. With the aim of minimizing the effect of this artifact on the longitudinal cut appearance, aligning the vessel center in successive images, and compensating for the repetitive roto-translation of the pullback, various computer assisted methods have been presented.

The registration of IVUS frames is challenging for two main reasons: (1) IVUS images suffer from speckle noise and have poor definition of edges, and (2) the vessel shape changes non-rigidly due to heart movement. As a result, the same part of the vessel can look different if sampled at different phases of the heart cycle. Different rigid and non-rigid registration algorithms have been proposed to tackle these two issues.

In [3], the authors present a method for non-rigid alignment of IVUS images based on Generalized Correlograms (GC) [48]. The method applies anisotropic diffusion to the IVUS images and detects the vessel boundary using a snake. Then, the algorithm samples the boundary at different locations to extract a set of local features. The non-rigid transformation is estimated by finding the optimal set of correspondence between landmarks (GC) of two IVUS images. The method has high computational cost and has been conceived to perform non-rigid registration aimed at retrieval.

An alternative method to suppress IVUS image rotation based on a kinematic model is presented in [91]. The model is used to estimate the center of rotation in the *short-axis* by computing the rotation of two ellipses that fit the vessel border in the two compared images. The method requires the detection of the vessel border with sufficient precision using a trained neural network.

In [45], a rigid registration algorithm composed of two steps is presented. Firstly, the method fixes the center of rotation as the center of mass of image gray-scale values. Secondly, it estimates the rotation between the two images by spectral correlation analysis [18]. The main limitation of this method is that the estimation of rigid rotation heavily depends on correct estimation of the center of rotation, and the center of mass, while robust with respect to noise and changes in image texture, may not be a good estimate of the center of rotation.

In [24], the authors present a method based on the scale-space optical flow algorithm with a feature-based weighting scheme. The algorithm is tested on a tissue-mimicking phantom, subjected to controlled amounts of angular deviation. Although interesting, the approach estimates only the catheter rotation, while the point of rotation is fixed in the image center.

In [40], the authors propose a method that aims at registering subsequent IVUS images by first aligning the center of the vessels, based on a modified version of the Fast Radial Symmetry transform [61], and then estimate the relative rotation by spectral correlation analysis [18]. The algorithm is efficient and robust to intra-patient

variations.

2.4 Methods for Automatic IVUS Analysis

The *state-of-the-art* methods on IVUS image analysis (such as lumen border detection, media border detection and plaque characterization methods) use image processing, machine learning and pattern recognition techniques to perform (semi)automated analysis. In order to understand such techniques, it is important to briefly introduce several terminologies and definitions of image processing, machine learning and pattern recognition techniques that will be used throughout the chapter.

Image Processing

- **Filters**: filtering is a class of signal processing, and the defining feature of filters is the complete or partial suppression of some component or feature of the signal. In image processing, filters can be used to extract features of interest from an image.

- **Local Binary Patterns (LBP)**: LBP [79] are texture operators which label the pixels of an image by thresholding the neighborhood of each pixel (for instance, by using the intensity value of the central pixel as a threshold) and by considering the result as a binary number. Examples of different neighborhoods are represented in Figure 2.5. The basic idea for developing LBP operators is that textures can be described by two complementary measures: local spatial patterns and gray-scale contrast. LBP are used to detect uniform texture patterns in circular neighborhoods, with any quantization of angular space and spatial resolution and invariant to brightness variations.

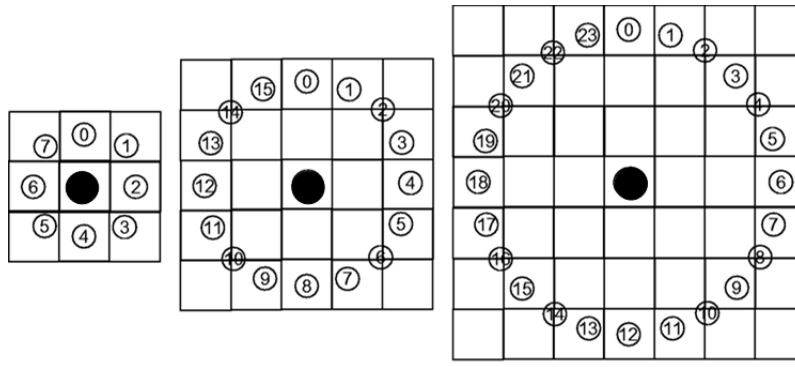

Figure 2.5: Three neighborhoods of a central pixel, used to define a texture and calculate a LBP.

- **Gabor filters**: Gabor filters [10] are a special case of wavelets and can be defined as Gaussian functions modulated by a complex sinusoid. Gabor filters are linear filters that can be helpful for extracting textural features from an

image, according to a particular filter orientation. A graphic representation of a Gabor filter is shown in Figure 2.6.

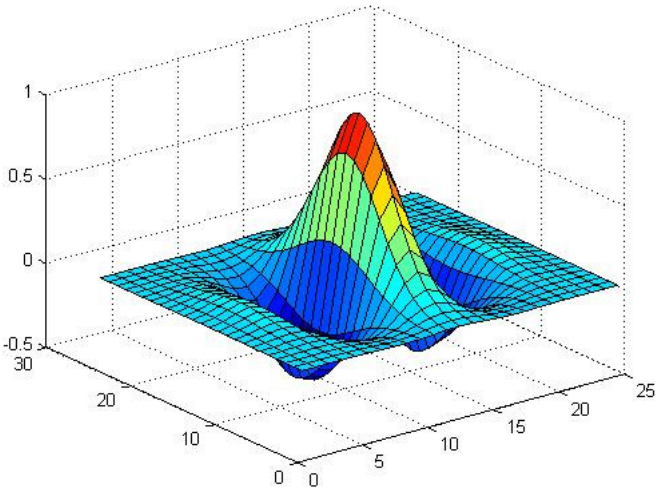

Figure 2.6: Example of a 2-D Gabor filter.

- **Morphological filtering**: mathematical morphology is a theory and technique for the analysis and processing of geometrical structures, based on set theory, lattice theory, topology and random functions. The basic idea is to probe an image with a simple, pre-defined shape, drawing conclusions on how this shape fits or misses the shapes in the image. This simple probe is called structuring element, and it is a binary image [100].

- **Active Contour Models (snakes)**: active contour models [49] are energy-minimizing splines, guided by internal constraint forces and influenced by external forces, used in image segmentation tasks. Given a parametric curve, $C(v) = (x(v), y(v))$, representing the position of the snake having arc length v, the energy function to be minimized is given by the following term:

$$E_{acm} = \int_0^1 E_{int}(C(v)) + E_{ext}(C(v))dv. \tag{2.1}$$

Following the original formulation [49], E_{int} is the internal energy of the snake due to bending :

$$E_{int} = \alpha \left(\frac{\partial C(v)}{\partial v} \right)^2 + \beta \left(\frac{\partial^2 C(v)}{\partial v^2} \right)^2. \tag{2.2}$$

The first-order term $\left(\frac{\partial C(v)}{\partial v}\right)^2$ represents the energy of the contour and makes the snake act like a membrane, while the second-order term $\left(\frac{\partial^2 C(v)}{\partial v^2}\right)^2$ represents the energy of the curvature and makes the snake act like a thin plate. Large values of α will increase the internal energy of the snake as it stretches more, whereas small values of α will make the energy function insensitive to the amount of stretch. Similarly, large values of β will increase the internal energy of the snake as it develops more curves, whereas small values of β will make the energy function insensitive to curves in the snake. The external energy E_{ext} attracts the snakes to salient features in the image, and can include constraint forces, to be defined based on the specific application.

Pattern Recognition Techniques and Classifiers

- **Pattern recognition techniques**: in *pattern recognition* techniques, a function (defined as *classifier*) is firstly trained on a data-set of samples, previously labeled within a given set of classes (training phase). The classifier can be *binary* when only two classes are defined, or *multi-class*. Then, the classifier is used to discriminate among the classes of interest in new samples (test phase). The *ground-truth* consists in a reliable data-set of labeled samples. Numeric information describing each sample is computed by *feature extraction* (i.e., the application of image processing filters to the image). During the training phase, a *learning algorithm* learns the characteristics of the training data by analyzing the extracted features and the corresponding labels, and it produces the trained *classifier*, with a set of parameters learned in the process. As a result, the classifier can analyze new samples and generate their output labels. The performance of the classification can be evaluated by comparing the classifier output labels to the corresponding test labels. The training and test processes are shown in the block diagram in Figure 2.7.

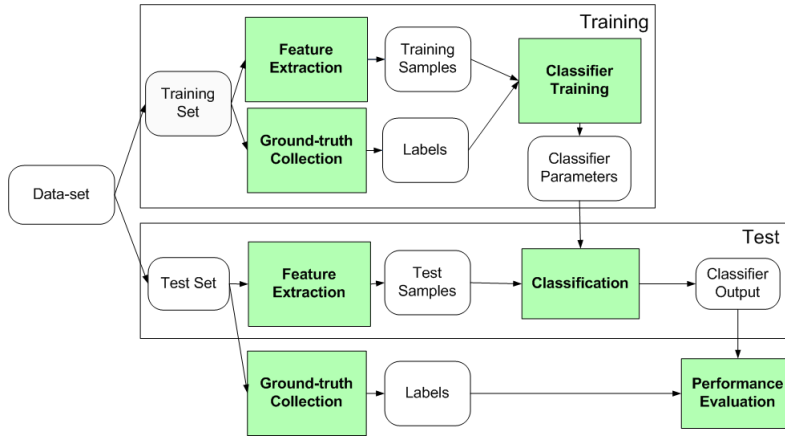

Figure 2.7: Scheme of the training and test phases in classification.

- **Discriminative classifiers**: discriminative classification methods model the dependence of an unobserved variable y on an observed variable x, by modeling the conditional probability distribution $P(y|x)$ which can be used for predicting y from x. Discriminative classifiers try to maximize the quality of the output on a given training set. Examples of discriminative classifiers are AdaBoost, Support Vector Machine and Random Forest.

- **AdaBoost**: the AdaBoost classification algorithm [35] creates a *strong* classifier as a linear combination of *simple weak* classifiers (base learners). An iterative method allows to keep adding base learners, until either the training error becomes lower than a given value or the number of iterations reaches a selected maximum number. An interesting quality of AdaBoost, when the base learner is a decision stump, is its ability to assign a weight to the features during the training stage, which can be related to the feature relevance and can be used to perform feature selection, i.e., to select a subset of relevant features for building a robust model. In fact, the decision stump selects, at each iteration, the single feature which reduced the labeling error the most.

- **Support Vector Machine (SVM)**: the SVM classifier [23] performs binary classification by constructing a N-dimensional hyperplane which optimally separates the samples into two categories. In the simplest case, the hyperplane is a line. Otherwise, when the data to be discriminated are separated by a nonlinear region, instead of fitting nonlinear curves to the data SVM uses a kernel function to map the data into a different space, where a linear hyperplane can be used to separate them. Although SVM is considered an efficient classifier, the training phase in case of large cardinality of the training set usually suffers from high memory usage and computational complexity.

- **Random Forest**: the Random Forest classifier [11] grows an ensemble of classification trees, where each tree votes for a class. The class produced as the output by the forest is the mode of the outputs of all the individual trees. Random Forest can robustly handle a very large number of input features. Like AdaBoost, Random Forest can measure the relevance of the features, based on the idea that randomly changing a relevant feature among those selected for building the tree affects the classification, while changing an irrelevant feature does not affect it.

- **Multiscale Stacked Sequential Learning (MSSL)**: MSSL [38] is a contextual meta-classifier, i.e., an algorithm aimed at enhancing the results of a first stage of classification. Its purpose consists in capturing and exploiting sequential label correlations extended over multiple spatial scales. In the first stage of the MSSL algorithm, classification is based on the assumption that each pixel of the analyzed images is independent of the others. Assuming a binary classification problem, the spatial continuity of the two regions to be discriminated can be additionally taken into account to improve the classifier capabilities. For this reason, the spatial neighborhood relation among the pixels of the images is exploited in a second stage of classification. As depicted in the block diagram of Figure 2.8, this second classification stage makes use of the feature set used

in the first classification stage, $\mathbf{x}$, and of the classification margin provided as an output by the first classifier, mar. For each image, the classification margin values are converted into an estimate of the likelihood that a sample belongs to one of the two classes and organized in a *pseudo-probability map*, $p \in [0, 1]$. In the MSSL scheme, the *pseudo-probability map* is represented according to a multi-scale (multi-resolution) decomposition. In the original bi-dimensional MSSL algorithm [38], given $p(\overrightarrow{q})$ the likelihood at position $\overrightarrow{q} = (x, y)$, the multi-resolution decomposition Φ is defined as follows:

$$\Phi(\overrightarrow{q}, s) = p(\overrightarrow{q}) * G\left(0, \gamma^{s-1}\right), \tag{2.3}$$

where $s \in \{1, 2, \ldots, S\}$ represents the scale, G is a bi-dimensional Gaussian with zero mean and standard deviation $\sigma = \gamma^s$ and γ is the "step" of the decomposition. The multi-resolution decomposition is then sampled following a grid, with regular sampling step, consisting of a set of $N_{displ} = s^2_{sampling}$ displacements. As a result, an additional set of features $\mathbf{z}$ is obtained, of length $S \times N_{displ}$. An extended feature set is created, $\mathbf{x}^{\mathbf{est}} = [\mathbf{x}, \mathbf{z}]$, by joining the original feature set and the additional features from the sampling. Finally, the extended set is analyzed by the second classifier and classification labels are produced. The two classifiers are trained separately and after training they can be applied to new images in the same scheme.

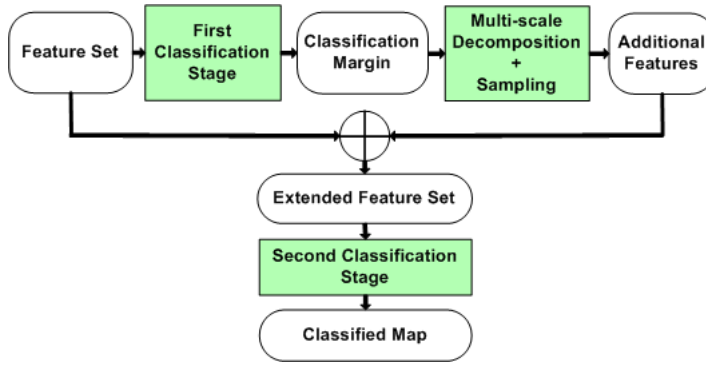

Figure 2.8: Block diagram representing the MSSL scheme.

2.4.1 Morphological Vessel Quantification in IVUS

The preprocessing stages for motion artifact compensation, described in Section 2.3, facilitate the analysis of IVUS sequences and allow meaningful and correct measurements. After preprocessing, several measurements on IVUS images are of interest for diagnosis, planning of intervention and follow-up monitoring. In particular, the extraction of the lumen border allows to derive measurements such as the minimum and maximum lumen diameter and the luminal area stenosis (a measure of luminal compromise relative to a reference lumen, analogous to the angiographic diameter stenosis). The area between the lumen border and the media-adventitia border is the

plaque area. Therefore, the extraction of the two vessel borders allows the measurements of the minimum and maximum plaque thickness and the plaque burden (the area occupied by atheroma, regardless of lumen compromise). Finally, the evaluation of the plaque composition (discriminating the different types of tissue, such as calcified, fibrotic, lipidic and necrotic) allows to assess the vulnerability of plaque. Following, a review of *state-of-the art* segmentation approaches is presented. A brief overview is given, but some of these topics will be addressed in more detail in the following chapters, since the author of this thesis has proposed contributions on these themes.

Lumen Border Extraction in IVUS Several automatic methods for segmentation of the arterial lumen from IVUS images have been proposed. Most of the approaches are based on active contour models (snakes). In [115, 121, 106], pixel intensity and gradient information (edges) combined with computational methods, including graph search, are used. In [57, 55, 85] the authors propose solutions based on active surfaces, active contours and neural networks.

In [16, 13, 116], the gray-level probability density function of the vessel structures, following Rayleigh distribution, is used.

Methods based on discrete wavelet decomposition have also been proposed [84, 51].

Approaches based on a learning process have been presented in [93, 83], where the lumen detection is achieved by means of the classification of blood areas in a supervised learning fashion. The authors in [66] develop a semi-automated approach using a parametrization of the lumen with a mixture of Gaussians PDFs. The sum of such Gaussian functions is deformed by the minimization of a cost function formulated using a probabilistic approach.

In [111], an automated shape-driven approach for the segmentation of the arterial wall is proposed. In a statistical shape space, properly built through PCA by using training data, the lumen contours are constrained to a smooth, closed geometry. In addition to a shape prior, an intensity prior is used through a non-parametric probabilistic energy function, with global image measurements.

A different strategy is explored in [59, 6], where the following phenomenon is exploited: in successive frames of the IVUS sequence, the texture in the lumen region exhibits a large variability of the speckle pattern, due to the blood flow, while the speckle pattern changes slowly in the tissue area. Based on this observation, the de-correlation generated by the blood flow is exploited.

In other approaches, segmentation is accomplished by the use of global region information including texture features [70, 86], gray-level variances to model ultrasound speckle [43, 62], and contrast of regions [125].

In Chapter 5, a contribution to the research on lumen border extraction is presented. A novel method based on supervised binary classification is proposed, which employs a multiscale stacked sequential learning scheme as a meta-classifier, thus taking into account the 2-D+T context of IVUS sequences. In a second phase, the lumen contour is identified by applying an active contour model to the output classification map.

Media-adventitia Border Extraction in IVUS Various techniques have been proposed for the detection of the media-adventitia border in IVUS. Part of these methods rely on the particular appearance of the vessel in proximity of the media layer, by exploiting the gray-level transition (dark-bright) in the media-adventitia interface. Gradient-based operators and edge detectors have been used [46, 106, 85, 111, 108]. The smoothness and continuity of the vessel shape have also been taken into account, by introducing deformable models [55, 125, 85, 42, 41, 108, 16]. In some approaches, the information on the vessel shape and tissue properties is obtained by means of a learning process [111, 42, 70, 22]. Finally, the idea of reproducing the human reasoning while detecting the media-adventitia border has been exploited in [70, 9, 80, 84, 22].

A challenge aimed at comparing the *state-of-the-art* methods for media-adventitia border detection and lumen border detection has been recently held in Toronto, Canada: the "Lumen + External Elastic Laminae (Vessel Inner and Outer Wall) Border Detection in IVUS Challenge" associated with the MICCAI 2011 workshop on Computing and Visualization for (Intra)Vascular Imaging[1].

Plaque Characterization in IVUS An important property of the IVUS imaging modality is its ability to describe the inner morphology of the vessel and its tissue composition. Different tissue types show different acoustic properties and, consequently, different intensities and shapes of the reflected ultrasonic wave. As a result, in the IVUS images, areas corresponding to different tissues exhibit different gray-level intensity and textures.

The plaque characterization task can be addressed as a *pattern recognition* problem. In fact, most of the plaque characterization methods proposed in the last years follow the main steps of a *pattern recognition* scheme: ground truth collection, feature extraction and training of a classifier. In the tissue characterization problem, the classifier learns from examples of different plaque types, such as the calcified, lipidic, fibrotic and necrotic types.

Among the *state-of-the-art* methods on plaque characterization, it is possible to distinguish between texture-based approaches, that rely on tissue appearance [120, 8, 14, 20], and spectrum-based approaches, that rely on the behavior of different tissues in the frequency domain [17, 52]. In both cases, texture and spectral information can be used as features, respectively. Other plaque characterization methods include wavelet-based approaches [68, 72] and elastography-based approaches [27, 97, 29, 64].

2.4.2 Bifurcation Detection

The detection of vascular bifurcations is particularly important in clinical applications, such as the diagnosis of vessel stenosis, surgical planning, and medical image registration, in which branching points can be used as landmarks.

In several studies in medical imaging, bifurcations have been identified as a means to segment and reconstruct the entire coronary tree. For instance, in a study on chest CT images [123], the AdaBoost learning technique is used for an automatic detection of bifurcations, aimed at improving the segmentation of vascular structures. In another paper [117], the Corkscrew segmentation algorithm is extended to identify

[1] https://www.cvc.uab.es/IVUSchallenge2011/

bifurcations in a CT data-set. Similarly, the authors in [67] and [56] address the problem of extraction and analysis of the coronary tree from X-ray angiographies by means of bifurcation identification.

In IVUS, the task of bifurcation identification has never been addressed before the study presented in this thesis. However, a few papers [9, 111] propose general frameworks aimed at the simultaneous segmentation of various structures in IVUS images, in which side branches are identified. In particular in [111], the maximum smoothed intensity for every column of the polar IVUS image is used as a feature, and a simple threshold is applied to identify the branches. In [9], a multi-agent image interpretation system is applied to IVUS images, in which interacting agents are provided manually with a set of rules. The performance of side branch detection is not evaluated. Additionally, both studies consider single image frames neglecting the temporal context.

In Chapter 3, a novel study on bifurcation detection in IVUS sequences is presented. The method identifies every bifurcation in an IVUS sequence, the corresponding frames, the angular orientation with respect to the IVUS acquisition, and the extension. This goal is achieved using the multi scale stacked sequential learning scheme, thus taking into account the 2-D+T context in the IVUS sequence. Each angular sector of the images is classified as belonging to a bifurcation or not. The proposed approach provides a robust tool for the easy and fast review of pullbacks, facilitating the evaluation of the lesion at bifurcation sites.

2.4.3 Alignment and Image Fusion

Multi-modal image registration techniques have been presented among IVUS and other imaging modalities. In particular, the fusion of IVUS and angiography data can be used to obtain a three-dimensional reconstruction of coronary vessels, while three-dimensional reconstruction using only IVUS data is limited by the lack of information on the vessel curvatures and catheter trajectory. Several methods have been developed for the alignment and fusion of IVUS and angiography data.

One of the first studies was the ANGUS system [103, 104]. In this work, the IVUS data are represented as a cylindrical stack of cross-sections. A least-square approximation is used to reconstruct the 3-D path of the catheter axis from two biplane X-ray images. The catheter trajectory is modeled in terms of a Fourier form. Then, the stack of IVUS contours is wrapped along this catheter centerline. To establish the correct rotational position of the slack, the authors make use of landmarks which are visible in angiograms as well as in a simulation of the angiograms derived from the reconstructed 3-D contour.

The method for 3-D reconstruction proposed in [118] combines the information about vessel cross-sections obtained from IVUS with the information about the vessel geometry derived from biplane angiography. First, the catheter path is reconstructed from its biplane projections, resulting in a spatial model. The locations of the IVUS frames are determined and their orientations relative to each other are calculated using a discrete approximation of the Frenet-Serret formulas known from differential geometry. The absolute orientation of the frame set is established utilizing the imaging catheter itself as an artificial landmark.

In [92], the authors present a multimedia workstation which enables the visualization, acquisition and handling of both IVUS and angiograms modalities, on- and off-line. The workstation enables DICOM decompression and browsing, video acquisition, reproduction and storage of IVUS data and angiograms with their corresponding ECG, automatic catheter segmentation in angiography images (using fast marching algorithm), B-Spline models definition for vessel layers on IVUS images, and a validated tool to fuse information. This approach defines the correspondence of every IVUS image with its correspondent point in the angiograms and vice-versa. The 3-D reconstruction of the IVUS catheter/vessel enables real distance measurements as well as three-dimensional visualization showing vessel tortuosity in the space.

In a recent study [110], a robust three-dimensional segmentation and registration approach of X-ray angiography and IVUS/Optical Coherence Tomography (OCT) is presented and validated. The approach starts with standard quantitative coronary angiography of the vessel of interest in the two angiographic views (either biplane or two monoplane views). Then, the vessel of interest is reconstructed in 3-D and registered with the corresponding IVUS/OCT pullback series by a distance mapping algorithm.

Finally, our group contributed to the research in this topic in [5]. In this study, three pairs of angiographic acquisitions are used. The first two pairs of acquisitions allow the reconstruction of the IVUS catheter path, while the third pair is used to visualize the coronary branching and requires contrast injection. The catheter tip is identified by the user. Starting from the user-selected point, catheter segmentation is performed using the fast marching algorithm computed in both angiographic projections of the IVUS catheter. The catheter path is reconstructed. A biplanar spline controlled by control points is fitted to the data following the un-distortion corrections proposed in [15]. In a second phase, the angular rotation of the 3-D local reference system (Frenet-Serret frame) with respect to the catheter path is estimated by computing the angle between the main artery and a second trajectory (bifurcation path) corresponding to a bifurcation artery. The bifurcation path is reconstructed by manually indicating an extreme of one branching artery and applying the fast marching algorithm until intersecting the catheter path. Successively, the user identifies the torsion by selecting the angle in which the bifurcation is visible on the IVUS *longitudinal view*.

The fusion of IVUS sequences with data from other imaging modalities has also been investigated. Compared to traditional imaging modalities, such as X-ray coronary angiography and IVUS, computed tomography angiography (CT) is not invasive and it provides a true 3-D or 3-D+T expression of the coronary tree.

In [63], IVUS images are combined with CT images, to provide a detailed representation of the coronary arteries in the CT images. The two data types are matched using three steps. First, vessel segments are matched using anatomical landmarks. Second, the landmarks are aligned in cross-sectional vessel images. Third, the semi-automatically detected IVUS lumen contours are matched to the CT data, using manual interaction and automatic registration methods.

In [113], the 3-D reconstruction of human coronary arteries is obtained by the fusion of IVUS and coronary CT. The IVUS images, together with IVUS-derived lumen and vessel borders, are positioned on the 3-D centerline, which is derived from

CT. The resulting 3-D lumen and wall contours are transformed into a surface for calculation of shear stress and plaque thickness.

IVUS has large penetration depth but the drawback of this modality is its comparably poor resolution. OCT is a relatively new catheter-based imaging technology that uses light interference to offer a high resolution for a small penetration depth.

In [112], the authors develop a method for image fusion of IVUS and OCT images, to enhance quantitative analysis of coronary arteries. A computer assisted fusion of corresponding frames from IVUS and OCT sequences is developed by a two-phase registration. However, the method is semi-automatic, since the longitudinal correspondences of input pairs from IVUS and OCT pullback volumes are selected manually by the user, and an automatic longitudinal registration of IVUS and OCT pullback sequences is stated as future work.

In Chapter 4, a novel study on temporal alignment between IVUS sequences acquired at different moments is presented. The Dynamic Time Warping non-rigid alignment algorithm is adapted to the specific IVUS alignment task. A fully automatic workflow for IVUS sequence alignment is developed, potentially applicable to other image modalities.

2.4.4 Quantification in Commercial Systems

Commercial products are available for analysis and quantification of IVUS sequences. The two leading companies for the commercialization of IVUS imaging systems and catheters are Boston Scientific and Volcano. Together with their IVUS equipments, these companies provide software for measurement and review of the cases.

Volcano were the first in the market to provide automatic tissue characterization. Volcano imaging systems are equipped with Virtual Histology - VH® [73] (the patented name for Volcano's tissue characterization software). In Virtual Histology, four tissues are discriminated: fibrous, fibro-fatty, necrotic core and dense calcium. The latest Volcano system is the VH® IVUS Imaging System, and it additionally provides automatic border contours for full segment analysis. A screenshot of the user interface is shown in Figure 2.9.

Boston Scientific is currently distributing its most recent iLab® Ultrasound Imaging System. The system is equipped with the iMap software for automatic plaque characterization [96]. Four different types of plaque are distinguished: fibrotic, lipidic, calcified and necrotic. An example of this tissue characterization feature is shown in Figure 2.10. Moreover, the software available on the iLab includes an automatic tracement of the vessel borders (TraceAssist™ software).

Medis QIVUS is a commercial solution for IVUS analysis. The semi-automatic contour detection is aimed at quickly calculating volumetric and plaque characterization data and can be used in large clinical studies.

Finally, Table 2.1 describes the different methods for IVUS analysis using the taxonomy defined in this chapter. The methods presented in this thesis work are also included.

Table 2.1: Overview of the *state-of-the-art* methods, based on our taxonomy on the IVUS technology in medical imaging. In the last rows of the table, the methods presented in the thesis are listed.

Method	*Motion art. comp.*		*Automatic IVUS analysis*				
	Gating	*Reg.*	*Segmentation*			*Bif. det.*	*Align./ Fusion*
			Lumen	*Media*	*Plaque*		
[12, 124, 30, 81, 82, 7, 39, 37]	x						
[3, 45, 24, 39, 91]		x					
[115, 121, 106, 57, 55, 85, 16, 13, 116, 84, 51, 93, 83, 66, 111, 59, 6, 70, 86, 43, 62]			x				
[46, 106, 85, 55, 125, 111, 108, 42, 70, 22, 41, 16, 9, 80, 84]				x			
[120, 8, 14, 20, 17, 52, 68, 72, 27, 97, 29, 64]					x		
[123, 117, 67, 56, 9, 111]						x	
[103, 104, 118, 92, 110, 5, 63, 113, 112]							x
Chapter 3 [2]						x	
Chapter 4 [1]							x
Chapter 5			x				

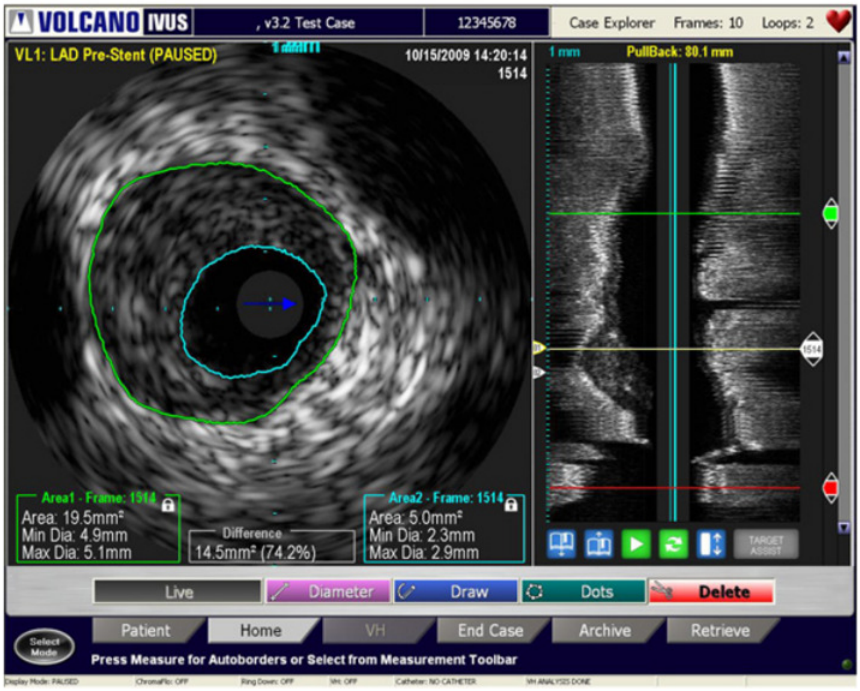

Figure 2.9: Screenshot illustrating the Volcano user interface.

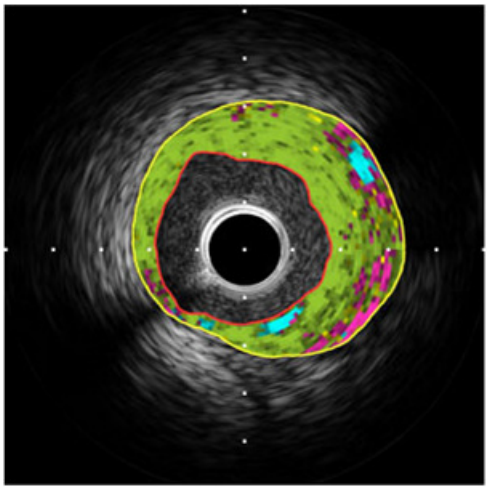

Figure 2.10: Screenshot illustrating the tissue characterization feature in iLab.

Chapter 3

Automatic Bifurcation Detection in IVUS Sequences

3.1 Introduction

Plaque growth and rupture preferentially involve specific vessel sites. An important example are vascular bifurcations, also named vessel branchings. Bifurcations can be defined as the sites where an artery diverges into two daughter vessels, the main branch and the side branch.

Bifurcations are critical vascular locations from the clinical point of view. In fact, it has been shown that arterial hemodynamics plays a relevant role in the progression of atherosclerosis [54]. In particular, the sites of abnormal and disturbed flow, such as vessel branching, are key regions for plaque evolution [119]. Wall thickenings and plaque formation in coronary arteries are frequently localized on the outer wall of one or both daughter vessels at major bifurcations [4]. Additionally, the rupture of vulnerable plaque may depend on anatomic parameters, such as the proximity of bifurcations and the axial bending during the cardiac cycle. In particular, the presence of a bifurcation before and especially after the lesion is a marker of an increased risk of plaque rupture and subsequent thrombosis [53]. This connection with disease formation is confirmed by the fact that a large number of bifurcation lesions undergo PCI [71].

The detection of vascular bifurcations is particularly important in clinical applications, such as the diagnosis of vessel stenosis, surgical planning and medical image registration, in which branching points can be used as landmarks. In several studies, bifurcations have been identified as a means to segment and reconstruct the entire coronary tree. For instance, in a study on chest CT images [123], the AdaBoost learning technique is used for an automatic detection of bifurcations, aimed at improving the segmentation of vascular structures. In another paper, Wette *et al.* [117] extend the Corkscrew segmentation algorithm to identify bifurcations in a CT data-set.

Similarly, Merle *et al.* [67] and Koehler *et al.* [56] address the problem of extraction and analysis of the coronary tree from X-ray angiographies by means of bifurcation identification.

Before the study presented in this chapter, the specific task of bifurcation identification has never been addressed in IVUS. However a few papers [9, 111] previously proposed general frameworks aimed at the simultaneous segmentation of various structures in IVUS images, in which side branches were identified too. In particular in [111], the maximum smoothed intensity for every column of the polar IVUS image is used as a feature, and a simple threshold is applied to identify the branches. In [9], a multi-agent image interpretation system is applied to IVUS images, in which interacting agents are provided manually with a set of rules. The performance of side branch detection is not evaluated. Additionally, both studies consider single image frames neglecting the temporal context.

A typical branching appearance in the IVUS *short-axis view* and *longitudinal view* is illustrated in Figure 3.1(b) and (c), respectively. It is worth mentioning that in the *short-axis view*, in presence of bifurcations, the vessel lumen changes its shape with respect to non-bifurcation transversal sections and the blood region tends to an elliptical profile with higher eccentricity than in other frames (Figure 3.1(a-b)). Moreover, the texture in the radial direction changes considerably in correspondence to bifurcations. In the *longitudinal view*, bifurcations appear as lateral ramifications of the vessel (Figure 3.1(c)).

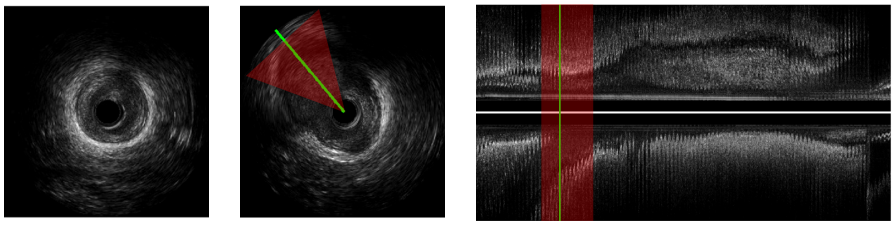

(a) (b) (c)

Figure 3.1: *Short-axis view* of a vessel showing (a) a non-bifurcation and (b) a bifurcation frame and (c) *longitudinal view* of the pullback. The lines in (b) and (c) indicate the angular and longitudinal bifurcation localizations, respectively. The regions displayed in red in (b) and (c) correspond to the angular and longitudinal branching extension, respectively.

In the clinical practice, physicians report the presence of bifurcations in terms of both frame localization and angular extension. Moreover, when analyzing a pullback, the angular position of a bifurcation (i.e., its orientation) with respect to the IVUS acquisition, represented in Figure 3.1(b) by a line, allows the visualization of the *longitudinal view* corresponding to the best cut in which the branching is visible (Figure 3.1(c)).

In this chapter, a study on automatic bifurcation detection in IVUS is presented. The proposed algorithm identifies every bifurcation in a pullback, the corresponding frames, the angular orientation with respect to the IVUS acquisition and the extension, enabling the quick navigation of the pullback only focusing on branches. The goal of bifurcation detection is reached by means of a *pattern recognition* approach, in which a set of features provides a representation of IVUS data in a multidimensional space, where a classifier is trained to solve the binary "bifurcation vs. non-bifurcation" problem. The most suitable set of features for bifurcation detection is obtained by analyzing textural features proposed in IVUS imaging studies [121, 14, 20] for characterizing, detecting and quantifying vessel structures. The results of three discriminative *state-of-the-art* classifiers (AdaBoost, Random Forest, and SVM) are compared. The choice of the best suited classification method for the proposed branching detection framework is discussed in the chapter, along with the selection of the most relevant features. After a first classification phase, a multi-scale stacked sequential learning scheme is used, exploiting contextual information [38]. The first learning level is a basic classifier which is integrated, at the second level, within a contextual classifier. By introducing the spatio-temporal context, the continuity of the bifurcation regions is considered for the refinement of the results. Finally, the classification results are further refined by exploiting *a-priori* information on branching dimensions and geometries.

The validation of the proposed method is presented on a data-set of 22 *in-vivo* IVUS sequences from coronary arteries, acquired from 22 patients. The approach provides a robust tool for the quick review of pullback sequences, facilitating the evaluation of the lesion at bifurcation sites. In this study, a new visualization map for IVUS sequences is presented, summarizing the vessel characteristics regarding the branchings. Finally, the output of the method can be used to extract 1-D temporal profiles describing the structure of the branchings along the analyzed vessel.

3.2 Bifurcation Detection Method

The method for bifurcation detection is divided into three sequential stages, as illustrated in Figure 3.2. First, the IVUS sequence is compensated for the artifacts due to motion. Subsequently, each *angular sector* in the sequence is classified as bifurcation or not, leading to a new visualization of IVUS pullbacks (Figure 3.2, bottom-left). The sequence is organized in a bi-dimensional representation in the space (θ, t), where θ is the angular position (orientation) with respect to the IVUS acquisition in the *short-axis view* and t is the longitudinal (temporal) position along the pullback. Finally, the spatial neighborhood relation among samples is exploited to refine the classification results.

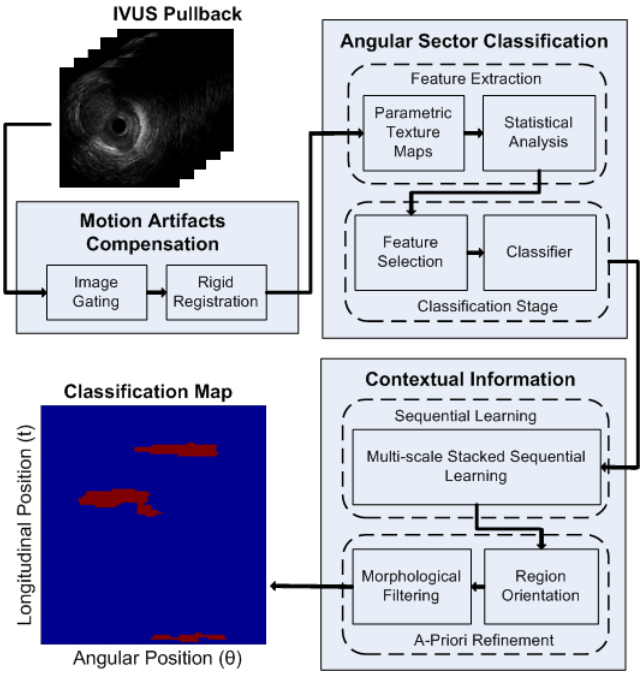

Figure 3.2: Block diagram of the proposed approach. Three main stages compose the workflow: (1) preprocessing for motion artifacts compensation, (2) classification of the *angular sectors* of each image frame, and (3) refinement of the obtained classification maps based on contextual information.

3.2.1 Compensation of Artifacts due to Motion

During the acquisition of an IVUS sequence, the catheter is affected by several artifacts due to the heart and the catheter motion, interfering with the visualization, the interpretation and the analysis of the acquired sequence. In order to compensate for the swinging effect and obtain a unique reconstruction for the transversal sections of the artery, the image-based gating algorithm proposed in [37] is applied, as described in Chapter 2. Moreover, in order to align the vessel center with the center of the image, an IVUS registration method [40] is applied, as detailed in Chapter 2. Figure 3.3 illustrates the results of the two successive stages of the applied artifact compensation. The swinging effect present in Figure 3.3(a) is compensated in Figure 3.3(b) and in Figure 3.3(c) the center of the vessel is aligned with the center of the pullback representation.

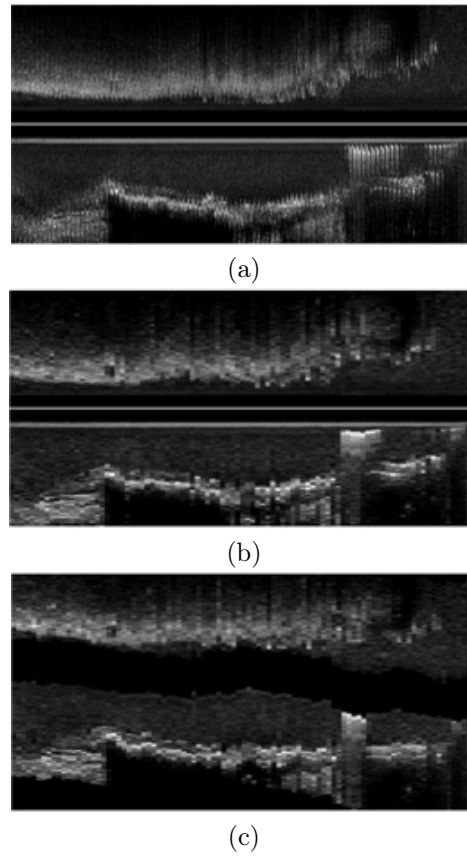

(a)

(b)

(c)

Figure 3.3: Compensation of artifacts due to motion. (a) *Longitudinal view* of an IVUS sequence before motion artifact compensation, (b) after the application of the gating technique and (c) after the successive registration.

3.2.2 Angular Sector Classification

In order to address the bifurcation detection task, a binary classification problem is defined, aimed at distinguishing between bifurcation and non-bifurcation *angular sectors*. The most intuitive analysis of an IVUS frame, inspired by the visual inspection performed by physicians, consists in the study of textural changes along the radial direction of each frame. For this reason, we choose to extract features computed along each *angular sector* of the image.

The approach relies on a *pattern recognition* technique, in which a binary classifier is firstly trained on a data-set of IVUS sequences, previously labeled by physicians (training phase). Then it is used to identify the presence of bifurcations in new sequences (test phase). For each IVUS sequence, the *ground-truth*, consisting in a reliable data-set of labeled samples (separating bifurcation and non-bifurcation samples), is created. Numeric information describing each *angular sector* is computed by

feature extraction.

Feature Extraction In most frames, the lumen has a pseudo-elliptical shape in the *short-axis view*, which typically, in the presence of bifurcations has higher eccentricity than in non-bifurcation frames, as shown in Figure 3.1(a-b). The radial extension of the blood region usually increases in correspondence to bifurcation *angular sectors*, as it happens, for instance, along the line in Figure 3.1(b). This property is exploited by extracting characteristics of the image texture computed along each radius of the IVUS frame. Since the applied rigid registration technique has aligned the center of the vessel with the center of the image (Figure 3.4), homogeneous radial features can be extracted. For this purpose, the region occupied by the catheter circular "ring down" artifact is replaced with a portion of lumen texture extracted from a frame of the sequence, as shown in Figure 3.4(b), (d). Each of the normalized images $I(x,y) \in [0,1]$, which constitutes the sequence $S(x,y,t) \in [0,1]$, is first converted into polar coordinates:

$$\widetilde{I}(\rho,\theta) = I(\rho \cdot \cos\theta, \rho \cdot \sin\theta), \tag{3.1}$$

where x and y are the horizontal and vertical coordinates in the cartesian system, ρ and θ are the radial and angular coordinates in the polar system, t is the longitudinal (temporal) coordinate along the pullback.

Following similar approaches of texture analysis applied to IVUS data [121, 20, 83], a set of N_T texture descriptors is defined. Each descriptor specifies a mapping function:

$$F: \widetilde{I}(\rho,\theta) \mapsto M_j(\rho,\theta), \tag{3.2}$$

where $M_j(\rho,\theta) \in \mathbb{R}$ is the parametric feature map according to the j^{th} textural descriptor, $j = 1, 2, \ldots, N_T$. Successively, in order to extract information on the extension and eccentricity of the blood region, the statistics related to each column θ of the obtained parametric maps is considered. For each *angular sector* (column in Figure 3.4(c), (d), basic statistical features: (i) standard deviation, (ii) mean value, (iii) median value, (iv) maximum value, (v) radial position of the maximum value, and (vi) histogram are computed. To this aim, a second mapping function D is applied:

$$D: M_j(\rho,\theta) \mapsto f_i(\theta), \tag{3.3}$$

where $f_i(\theta) \in \mathbb{R}$, $i = 1, 2, \ldots, N_D$, and N_D is defined as the total number of statistical descriptors.

Two families of texture descriptors are applied, of which the first has demonstrated its capability to characterize the tissue in IVUS images [87, 14], while the second one has been used to characterize the blood region [59, 60]. The first group $(M_j(\rho,\theta)_{tissue})$ is composed of the following maps:

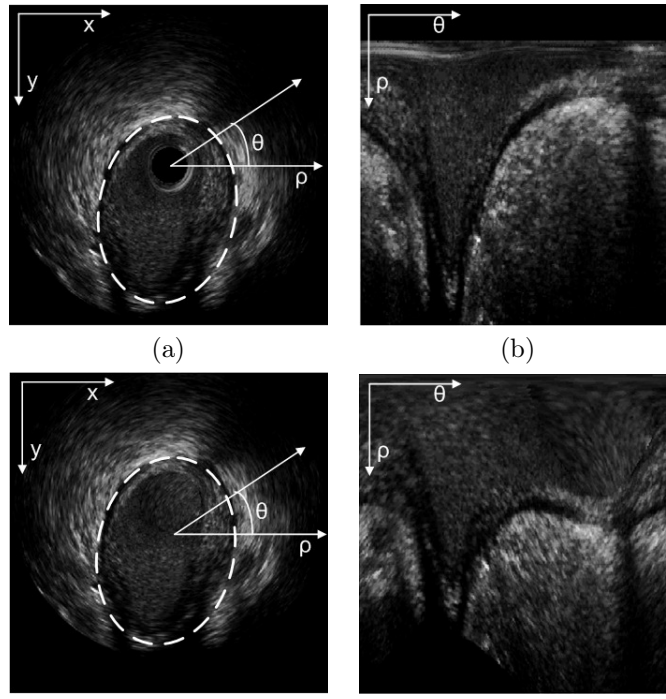

Figure 3.4: *Short-axis view* of a bifurcation frame before the registration phase (a) in the cartesian coordinate system and (b) in the polar representation. View of the same frame after the registration phase and the "ring down" artifact compensation, (c) in cartesian and (d) in polar coordinates. The dotted curves represent an approximation of the typical geometry of the blood region contour in the bifurcation case.

- Gabor filters [10] can extract the textural properties of the image according to a particular filter orientation.
- Local binary patterns (LBP) [79] are used to detect uniform texture patterns in circular neighborhoods, with any quantization of angular space and spatial resolution and invariant to brightness variations.

The second group ($M_j\left(\rho,\theta\right)_{blood}$) consists of six maps including auto-correlation and cross-correlation:

- Auto-correlation and cross-correlation are introduced to exploit the low correlation expected in the blood region with respect to the tissue due to the flow motion [59, 60]. Each of them is used at three scales: 6, 12, and 18 pixels representing 1/3, 2/3, and the size of the speckle on the IVUS image, respectively.

The gray-level image $\widetilde{I}\left(\rho,\theta\right)$ is considered as one of the feature maps, as well, leading to a total of 12 main maps. On the seven parametric maps $\widetilde{I}\left(\rho,\theta\right)$ and $M_j\left(\rho,\theta\right)_{blood}$

two additional transformations are applied [20], leading to the computation of fourteen additional maps $A_{ej}(\rho,\theta)$, and $A_{ij}(\rho,\theta)$ for a total number of 26 parametric maps. The map A_{ej} can be related to a quantification of the blood accumulation in the range $[\rho\ \rho_{MAX}]$, where ρ represents the radial depth, while the map A_{ij} gives information about the amount of blood accumulated in the range $[1\ \rho]$:

$$A_{ej}(\rho,\theta) = \rho \frac{\sum_{m=\rho}^{\rho_{MAX}} M_j(\rho,\theta)}{\rho_{MAX} - \rho} \tag{3.4}$$

$$A_{ij}(\rho,\theta) = \frac{\sum_{m=1}^{\rho} M_j(\rho,\theta)}{\rho} \tag{3.5}$$

where ρ_{MAX} is the maximum value of the radius.

The computation of statistical features $f_i(\theta)$ on all the parametric maps ultimately provides information about the presence of a bifurcation. For instance, the position of the maximum value in the gray-level image usually corresponds to the distance between the vessel center and the vessel border and it increases with the vessel eccentricity; at the same time, the standard deviation and the mean value along the radius typically decrease, due to the presence of external vessel tissue (adventitia) with bright appearance (see Figure 3.4). Each angular sector θ is described by a feature vector $\mathbf{x}(\theta) = [x_1(\theta)\ x_2(\theta)\ \ldots\ x_{N_F}(\theta)]$, where $N_F = 253$ is the total number of considered features.

Classification In the proposed framework, a *supervised* learning approach is chosen, given the availability of ground-truth data and the consequent possibility of learning from examples. A *discriminative* classification method is applied in order to avoid the need to formulate hypotheses on the feature space. A comparison among the results of three *state-of-the-art* discriminative classifiers (AdaBoost, Random Forest, and SVM) is provided, in terms of performance and computational cost. The three algorithms have been described in Chapter 2. Beyond the classifier labeling, an additional output provided by the above mentioned classifiers is the classification margin $mar \in [-\infty, +\infty]$, representing, in the feature space, the distance from a sample to the decision boundary.

3.2.3 Contextual Information

Multi-Scale Stacked Sequential Learning In the learning system described so far, the classification is based on the assumption that each *angular sector* of the IVUS images is independent of the others. However, the continuity of the branchings in pullback sequences can be additionally taken into account to enhance the classifier capabilities. An MSSL scheme [38] is applied, consisting in a contextual meta-classifier in which the first stage of classification is included, as a way of capturing and exploiting sequential correlations extended over multiple spatial scales. The

generic MSSL method has been described in Chapter 2. In this section, we report its application into the bifurcation detection framework.

The MSSL scheme makes use of the feature set used in the previous classification and of the classification margin provided as an output by the first classifier. For each pullback, the classification margin values are converted into an estimate of the likelihood that a sample belongs to the bifurcation class and organized in a bi-dimensional *pseudo-probability map*, $p_b(\theta, t) \in [0, 1]$, being θ the angular polar coordinate and t the longitudinal (temporal) position (Figure 3.5-a). The representation of an IVUS sequence in the space (θ, t) is introduced to exploit the spatial coherence of neighboring pixels. In the MSSL scheme, the *pseudo-probability map* is represented according to a multi-scale (multi-resolution) decomposition. Given $p_b(\overrightarrow{q})$ the likelihood at position $\overrightarrow{q} = (\theta, t)$, the multi-resolution decomposition Φ is defined as follows:

$$\Phi(\overrightarrow{q}, s) = p_b(\overrightarrow{q}) * G\left(0, \gamma^{s-1}\right), \tag{3.6}$$

where $s \in \{1, 2, \ldots, S\}$ represents the scale, G is a bi-dimensional Gaussian with zero mean and $\sigma = \gamma^s$ and γ is the "step" of the decomposition. The multi-resolution decomposition is sampled to obtain a set of features. Wrap-around issues are handled by using a circular padding in the horizontal dimension of the map and by setting the values of the extended set outside the map to 0 in the vertical dimension as the most conservative choice. An extended feature set is created, by joining the original feature set to the additional features from the sampling. Finally, the extended set is analyzed by a second classifier and final classification labels are produced. The two classifiers are trained separately and after training they can be applied to new sequences inside the same scheme. The multi-resolution decomposition allows to recover the homogeneity and regularity of the bifurcation regions at different scales, if such properties are present in the training samples. In Figure 3.5, the binary classification output before (b) and after (c) sequential learning is illustrated for a sequence, together with the corresponding *pseudo-probability map* (a). We can notice an increase in the homogeneity of the classified regions and a decrease in the presence of false positive errors after the second stage of classification.

A-priori Map Refinement After the classification stage, the results are refined, by taking advantage of *a-priori* knowledge about the geometry of the coronary branchings and the characteristic dimensions of the vessels. Different artifacts, such as the guidewire shadow, might be confused with bifurcation regions, since their appearance in the *short-axis view* may be similar. However, since the textural pattern of the guidewire shadow is repeated along several frames of the sequence, it is possible to discriminate between the two structures by discarding from the classification maps the regions in which the longitudinal dimension is much more extended than the angular dimension. The regions forming an angle with respect to the θ-axis, which is superior to a given threshold τ are removed. Subsequently, in order to make the results more homogeneous and exclude regions that are too small to be bifurcations, a morphological filtering is performed with a rectangular structuring element of size

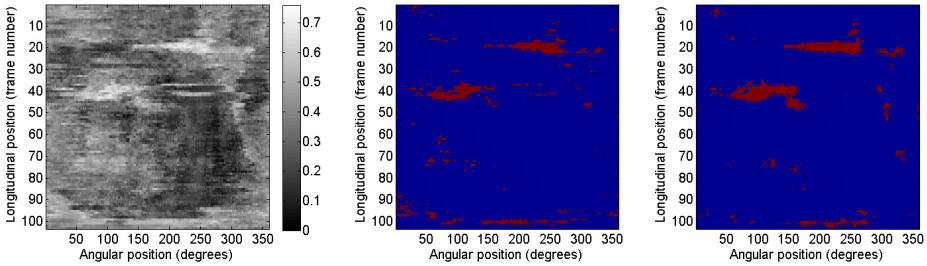

Figure 3.5: (a) *Pseudo-probability map* for a pullback, in which the gray-level expresses the likelihood of bifurcation presence. Corresponding binary label maps, after (b) the first and (c) the second classification stages of the MSSL scheme. The detected bifurcation regions are represented in red. The horizontal and vertical axes represent the angular position with respect to the IVUS acquisition θ and the longitudinal position t, respectively.

$[n_D\ n_F]$, where n_D is the number of angular degrees and n_F is the number of frames. A cross-validation process is applied to tune the model parameters τ, n_F, and n_D.

3.3 Experimental Results

3.3.1 Materials: Reference Data

A set of 22 *in-vivo* pullbacks from human coronary arteries has been acquired from 22 patients by means of iLab IVUS Imaging System (Boston Scientific), using a 40 MHz catheter Atlantis SR 40 Pro (Boston Scientific). The data-set and the ground-truth of bifurcation labels are described in Appendix B. *Angular sector* samples have been labeled as "bifurcation" or "non-bifurcation" samples.

The classification performance is assessed by means of *Leave-One-Patient-Out* (LOPO) cross-validation technique over $N_P = 22$ folds. LOPO can be considered as a special case of N-fold cross-validation, where each fold contains all the data from one patient. Further details about LOPO technique can be found in [19]. For each fold, the training is performed on samples from all the other folds and the trained classifier is tested on the fold itself. The performance is evaluated as an average of the results over the N_P folds in terms of:

$$\begin{array}{rc} \text{Accuracy:} & A = \frac{TP+TN}{TP+TN+FP+FN} \\ \text{Sensitivity:} & S = \frac{TP}{TP+FN} \\ \text{Specificity:} & K = \frac{TN}{TN+FP} \\ \text{Precision:} & P = \frac{TP}{TP+FP} \\ \text{False Alarm Ratio:} & FAR = \frac{FP}{TP+FN} \\ \text{F-measure:} & F = \frac{2PS}{(P+S)} \end{array}$$

where TP = True Positive, TN = True Negative, FP = False Positive, and FN = False Negative.

The positive and negative classes are strongly unbalanced, since the positive class represents 1% of the total amount of samples. In order to achieve a good generalization in the training phase, all the bifurcation samples are used, together with an equal number of randomly selected negative samples. In the test phase, a normalization of the confusion matrix is applied for the computation of all the performance scores with the exception of the accuracy.

It is worth noticing that in a detection problem, the two most significant parameters are sensitivity S and precision P, since in this case S (*true positive rate*) expresses the proportion of actual bifurcation samples, which are correctly identified as such, and P (*positive predictive value*) represents the proportion of samples assigned to the bifurcation class which are correctly classified. Therefore, the F-measure can be used as a single score to assess the overall performance of the method, since it is defined as the harmonic mean of precision and sensitivity.

3.3.2 Bifurcation Classification

The AdaBoost, Random Forest, and SVM classifiers are compared in the bifurcation vs. non-bifurcation classification. Since, among the three methods, AdaBoost and Random Forest are able to handle efficiently a large training set and a high-dimensional feature space, the two classifiers are firstly compared. Once the best performing classification algorithm between the two is identified, the method is compared with SVM using a selected subset of the most relevant features.

AdaBoost vs. Random Forest To ensure its convergence, AdaBoost has been trained up to $N_{iter} = 110$ iterations and the classifier has been noticed to converge after around 80 iterations. The parameters of Random Forest are set to a number of trees $N_{trees} = 1,000$ and a number of input variables determining the decision at each node of the tree $M_{try} = \log_2(N_F) + 1$, as suggested by [11]. In order to corroborate the statistical significance of the achieved results, the Wilcoxon signed-ranks test [28] is performed. With a significance level $\alpha = 0.05$, the null hypothesis that the mean values of the two distributions are equal can be rejected if $z < -1.96$, where z is the value of the Wilcoxon statistics. The last two columns in Table 3.1 illustrate, for each comparison, the difference between the average performance scores of AdaBoost and Random Forest and the value of the z statistics, respectively. The presence of the asterisk in the fifth column denotes statistical significance. For each performance measure, the score of the technique which performs better is typeset in bold.

Random Forest is superior to AdaBoost for most of the considered performance scores (Table 3.1) and has an excellent performance in terms of accuracy (94.85%).

Table 3.1: Performance ($MEAN \pm STD$) of the AdaBoost and Random Forest classifiers.

	AdaBoost	*Random Forest*	$\triangle_\mu$	z
A	$(89.82 \pm 4.51)\%$	$(\mathbf{94.85} \pm 3.49)\%$	$+5.03\%$	$-4.10*$
S	$(\mathbf{76.97} \pm 11.94)\%$	$(63.50 \pm 22.19)\%$	-13.47%	$-2.56*$
P	$(88.57 \pm 4.69)\%$	$(\mathbf{92.56} \pm 5.50)\%$	$+3.99\%$	$-2.71*$
K	$(89.96 \pm 4.55)\%$	$(\mathbf{95.19} \pm 3.51)\%$	$+5.23\%$	$-4.10*$
FAR	$(10.04 \pm 4.55)\%$	$(\mathbf{4.81} \pm 3.51)\%$	-5.23%	$-4.10*$
F	$(\mathbf{81.90} \pm 7.45)\%$	$(73.35 \pm 16.73)\%$	-8.55%	$-2.48*$

However, the sensitivity is lower (63.50% for Random Forest when compared with 76.97% for AdaBoost) leading to a significantly lower F-Measure score. Moreover, the computational complexity of AdaBoost with decision stumps is lower, since it is $O(Tnm)$ in training and $O(T)$ in test, while for Random Forest it is $O(TnM_{try})$ in training and $O(Tn)$ in the worst case, $O(T \log n)$ in average in test, where T is N_{iter} for AdaBoost and N_{trees} for Random Forest, n is the number of training samples, m is the number of features, and $M_{try} < m$ is the random subspace dimensionality. Considering this, it can be stated that the AdaBoost classifier is the best suited for the proposed task.

Feature Selection by Weight Analysis A feature selection study is performed, with the aim of reducing the computational cost of the learning algorithm and possibly enhancing the generalization capability of the classifier. Different learning algorithms may perform better with different feature sets, since there cannot be a unique concept of relevant features [25]. For this reason, feature selection is performed based on the used classification algorithm. The embedded property of AdaBoost with decision stump of assigning a weight to each *weak* classifier (feature) at each training iteration is exploited. Such weights can be used to evaluate the feature relevance. Let us define N_P the number of sequences, N_F the number of initial features, $k = 1, 2, \ldots, N_F$ the index of each feature and α_p^k the weight assigned to the k^{th} feature at the p_{th} LOPO validation fold, corresponding to the p_{th} pullback. The normalized weight assigned by AdaBoost to each feature w_k can be expressed as:

$$w_k = \frac{1}{N_P} \sum_{p=1}^{N_P} \frac{\alpha_p^k}{max\left\{\alpha_p^1, \ldots, \alpha_p^{N_F}\right\}} \tag{3.7}$$

The normalized weights w_k are used to perform feature selection, by keeping only the features whose cumulative weight represents a percentage of the total cumulative weight set to 75%. For this reason, the initial set of $N_F = 253$ features $\mathbf{x} = [x_1\, x_2\, \ldots\, x_{N_F}]$ is ordered from the most to the least relevant descriptor, creating a sorted set $\mathbf{x}_{SORT} = [x_{1S}\, x_{2S}\, \ldots\, x_{N_F S}]$ with corresponding normalized weights $\mathbf{w}_{SORT} = [w_{1S}\, w_{2S}\, \ldots\, w_{N_F S}]$. Subsequently, the feature subset $\widetilde{\mathbf{x}}_{SORT} \subseteq \mathbf{x}_{SORT}$, $\widetilde{\mathbf{x}}_{SORT} = \left[x'_1\, x'_2\, \ldots\, x'_{N_S}\right]$ with corresponding normalized weights $\widetilde{\mathbf{w}}_{SORT} =$

$\left[w'_1\ w'_2\ \ldots\ w'_{N_S}\right]$ is selected, comprising the most relevant N_S features in $\mathbf{x}_{SORT}$ whose partial cumulative weight $cw_p = \sum_{j=1}^{N_S} w'_k$ sums up to 75% of the total cumulative weight:

$$N_S : \sum_{k=1}^{N_S} w'_k = 0.75 \cdot \sum_{k=1}^{N_F} w_{kS} \tag{3.8}$$

resulting in $N_S = 40$ selected features.

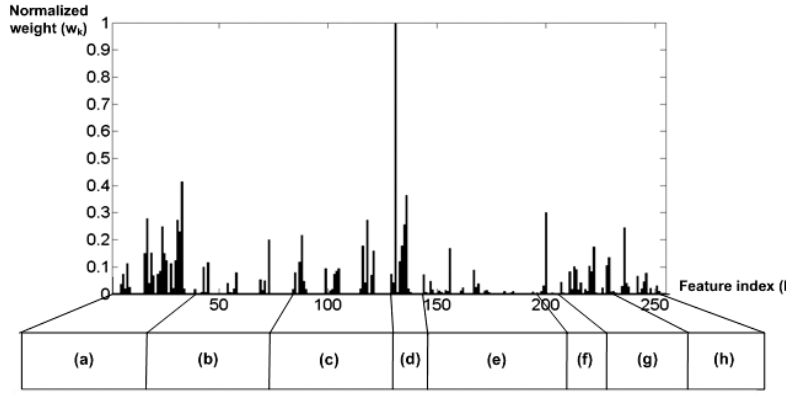

Figure 3.6: Analysis of the normalized weight for each feature. The descriptors are organized into different categories: (a) gray-level image, (b) Auto-correlation, (c) Cross-correlation, (d) Gabor, (e) LBP, (f) shadow transformations on the gray-level image, shadow transformations on the (g) Auto-correlation and (h) Cross-correlation maps.

In Figure 3.6, the normalized weight w_f for each feature in $\mathbf{x}$ is represented, together with a summarized description of the feature categories. Among the most relevant descriptors are: the radial position of the maximum value, both in the gray-level image and in its parametric representations, features computed from the Gabor parametric maps, features computed from the gray-level image and features from the cross-correlation maps.

The AdaBoost algorithm is applied on the extracted subset $\widetilde{F}_{SORT}$, using $N_{iter} = 110$ iterations. In Table 3.2, an overall improvement in the performance after feature selection can be observed. In particular, the statistical analysis proves that the sensitivity, precision and F-Measure scores, which are the most relevant for the considered application, significantly increase. Moreover, the computational complexity in training $O(Tnm)$ decreases.

Table 3.2: Performance ($MEAN \pm STD$) of the AdaBoost classifier ($[a]$) before and ($[b]$) after feature selection.

	$[a]$	$[b]$	Δ_μ	z
A	(**89.82** $\pm$ 4.51)%	(89.79 $\pm$ 4.49)%	-0.03%	-0.82
S	(76.97 $\pm$ 11.94)%	(**81.24** $\pm$ 11.48)%	$+1.27\%$	$-2.56*$
P	(88.57 $\pm$ 4.69)%	(**89.08** $\pm$ 4.47)%	$+0.51\%$	$-2.06*$
K	(**89.96** $\pm$ 4.55)%	(89.90 $\pm$ 4.55)%	-0.06%	-0.82
FAR	(**10.04** $\pm$ 4.55)%	(10.10 $\pm$ 4.55)%	$+0.06\%$	-0.82
F	(81.90 $\pm$ 7.45)%	(**84.56** $\pm$ 6.84)%	$+2.66\%$	$-3.29*$

AdaBoost vs. SVM The training set cardinality and the feature space dimensionality imply a high computational cost for the classification. We choose not to reduce the number of training samples because of the imbalance between the two classes. However, the SVM can be accelerated by applying it after feature selection, reducing the feature space dimensionality. Hence, the performance of AdaBoost and SVM are compared using the $N_S = 40$ selected features. A Radial Basis Function (RBF) kernel is used and the parameters γ and C are tuned as indicated in [89] and in this way set to $\gamma = 0.001$ and $C = 10$. The results of the SVM classifier are compared in Table 3.3 with the results of AdaBoost after feature selection. As it can be observed, the SVM classifier is superior to AdaBoost in terms of sensitivity, but it is significantly inferior in terms of the accuracy, precision, specificity, false alarm ratio scores. The overall performance is comparable, as shown by the F-measure scores. However, the computational complexity of SVM is higher, since it varies between $O(n^2)$ and $O(n^3)$ in training, depending on the number of support vectors and it is $< O(nm)$ in test. Additionally, the accuracy of a SVM model largely depends on the selection of the kernel parameters, which have to be tuned implying a high computational cost during training. By considering these results, it can be concluded that the AdaBoost classifier is the most appropriate technique for the addressed task.

Table 3.3: Performance ($MEAN \pm STD$) of the AdaBoost and SVM classifiers, on the set of selected features.

	$AdaBoost$	SVM	Δ_μ	z
A	(**89.79** $\pm$ 4.49)%	(87.46 $\pm$ 5.51)%	-2.33%	$-3.23*$
S	(81.24 $\pm$ 11.48)%	(**83.26** $\pm$ 12.09)%	$+2.02\%$	-1.23
P	(**89.08** $\pm$ 4.47)%	(87.12 $\pm$ 5.34)%	-1.96%	$-2.77*$
K	(**89.90** $\pm$ 4.55)%	(87.53 $\pm$ 5.57)%	-2.37%	$-3.23*$
FAR	(**10.10** $\pm$ 4.55)%	(12.47 $\pm$ 5.57)%	$+2.37\%$	$-3.23*$
F	(84.56 $\pm$ 6.84)%	(**84.71** $\pm$ 07.37)%	$+0.15\%$	-0.17

Bifurcation Map Refinement After the classification of *angular sectors* as independent samples, a refinement of the results is performed in two stages. First, the contextual information is exploited using the MSSL approach. Then, the guidewire artifact and the small detected regions are removed using *a-priori* information.

It is worth noticing that the MSSL scheme is independent of the classification methods chosen for the two classification stages. The multi-scale decomposition is applied using 5 scales, by setting the decomposition parameters to $\sigma = 2e^{(s-1)}$ and $s = \{1, 2, \ldots, 5\}$ and using a 9 element neighborhood. The sampling leads to 45 additional features, for a total 85 features composing the extended feature set. The AdaBoost classifier is applied to the extended feature set, performing $N_{iter} = 160$ iterations. The parameters of the a-priori refinement τ, n_D, and n_F are tuned by exhaustive search by maximizing the F-Measure score using LOPO cross-validation technique. The parameters are tuned on reasonable ranges of values chosen based on the data analysis. In particular, the threshold τ ranges between 25 degrees and 50 degrees, while the horizontal and vertical dimensions of the structuring element n_D and n_F range between 5 and 20 degrees and 1 to 5 frames, respectively. The obtained optimized parameters are $\tau = 30$ degrees, $n_D = 10$ degrees and $n_F = 1$ frame.

In Table 3.4, the overall incremental results for the successive stages of the method are illustrated, together with inter-observer and intra-observer variability. We can notice a steady improvement of the performance for consecutive phases of the workflow (rows from [*a*] to [*e*]), which is reflected into the increase in the F-Measure score. The second classification stage of the MSSL scheme is apparently in counter trend because the F-Measure slightly decreases. At the same time, the computational complexity additionally includes both (1) the complexity for the multi-scale decomposition + sampling $O(SN_{map} \log N_{map} + 9SN_{map})$, where S is the number of scales, N_{map} is the size of the map, and 9 is the size of the sampling neighborhood, and (2) the complexity for the second classification stage. However, this step produces a significant decrease in the false alarm ratio score (row [*c*]). The a-priori refinement improves the performance (rows [*d*], [*e*]) without being computationally expensive, since the computational complexity is $O(R)$ for the first stage, where R is the number of connected branching regions, and $O(n_D n_F N_{map})$ for the second stage, where N_{map} is the size of the map, and n_D, n_F are the two dimensions of the structuring element.

The automatic method reaches an accuracy of 95.21%, a sensitivity of 80.66%, a precision of 94.60% and an F-Measure of 86.35%. It can be noticed that the sensitivity score, which is critical in a detection problem, is low for inter-observer variability (57.05%): the task of evaluating bifurcation location and extension is particularly challenging also for trained physicians and the results suffer from substantial variability depending on the observer. The F-Measure score reached by the automatic method is higher than for both the intra- and inter-observer variability (+10.17% and 14.72% respectively), showing that the algorithm successfully reaches a compromise between the two segmented ground-truths.

The performance of the method significantly decreases if only the first classifier is used (rows[*h*], [*i*]), because the MSSL scheme helps to find connected regions on which the first stage of refinement is based.

3.4 Discussion

3.4.1 Results Analysis

The identification of vascular bifurcations in IVUS images is considerably challenging due to the high variability in branching dimensions and appearance. Portions of the vessel may look like bifurcations, when the catheter is far from the vessel center, when the probe is close to the ostium and when the vessel is large. Additionally, shadows can hide bifurcations, making the images with deployed stent more difficult to classify. The images in Figure 3.7(a-c) illustrate some challenging frames in which the existing bifurcations are correctly identified. In most cases, the errors of the automatic method can be ascribed to a specific vessel morphology. False positive errors are localized most frequently in correspondence to deployed stents (Figure 3.7(d-f)), in vessel sections close to the ostium (Figure 3.7(g-h)) and when a vein is visible close to the inspected vessel (Figure 3.7(i-j)). Veins might be confused with the extreme frames of the branches where two lumen regions are separated by adventitia. False negative errors are mostly found in case of small bifurcations, such as the one represented in Figure 3.7(k). Finally, the method rarely fails in large bifurcation frames. It is worth mentioning that in several cases the method performs better than the manual labeling, since in some cases one or both experts did not label a branching which is actually present in the sequence, as illustrated in Figure 3.7(l). Indeed, the physicians confirmed the presence of a bifurcation a-posteriori, given the algorithm detection.

3.4.2 Clinical Applicability: Evaluation per Regions

For a clinical use of the proposed method, the main concern for physicians is that a minimum amount of branching regions actually present in the IVUS sequences are misclassified in the automatic detection. In the case of a classification method used as an object detector, each object present in the ground-truth (in this case, a branching) may or may not intersect a detected region. Evaluation can be performed in terms of a "*True Positive detected Object*" (TPO) score, defined as the percentage of labeled ground-truth branchings that intersect a detected region. TPO can be considered as a measure of sensitivity computed using the regions as samples. Maximizing TPO is fundamental in a detection application, especially in a clinical context. The obtained TPO results (90.97%) are superior to the inter-observer TPO score (86.37%) and comparable to the intra-observer score (91.12%), which is extremely encouraging for the clinical applicability of the method. The graphic in Figure 3.8 shows how TPO is influenced by the branching dimension, computed as the angular extension of the

Table 3.4: Incremental performance ($MEAN \pm STD$) of the automatic method, in rows [a] to [e]: ([a]) before feature selection, ([b]) after feature selection, ([c]) at the second classification stage of the MSSL scheme, ([d]) refinement based on region orientation, ([e]) refinement using morphological filtering. ([f]) Inter-observer and ([g]) intra-observer variability. Refinement performance by applying only the first classification stage: ([h]) refinement based on region orientation, ([i]) refinement using morphological filtering.

	A	S	P	K	FAR	F
[a]	$(89.82 \pm 4.51)\%$	$(76.97 \pm 11.94)\%$	$(88.57 \pm 4.69)\%$	$(89.96 \pm 4.55)\%$	$(10.04 \pm 4.55)\%$	$(81.90 \pm 7.45)\%$
[b]	$(89.79 \pm 4.49)\%$	$(\mathbf{81.24} \pm 11.48)\%$	$(89.08 \pm 4.47)\%$	$(89.90 \pm 4.55)\%$	$(10.10 \pm 4.55)\%$	$(84.56 \pm 6.84)\%$
[c]	$(91.88 \pm 3.24)\%$	$(79.40 \pm 15.33)\%$	$(90.68 \pm 4.33)\%$	$(92.02 \pm 3.26)\%$	$(07.98 \pm 3.26)\%$	$(84.00 \pm 10.05)\%$
[d]	$(\mathbf{95.42} \pm 2.05)\%$	$(77.67 \pm 17.08)\%$	$(\mathbf{94.60} \pm 2.61)\%$	$(\mathbf{95.62} \pm 2.05)\%$	$(\mathbf{04.38} \pm 2.05)\%$	$(84.29 \pm 11.42)\%$
[e]	$(95.21 \pm 2.28)\%$	$(80.66 \pm 14.90)\%$	$(\mathbf{94.60} \pm 2.65)\%$	$(95.38 \pm 2.29)\%$	$(04.62 \pm 2.29)\%$	$(\mathbf{86.35} \pm 9.28)\%$
[f]	$(97.01 \pm 1.76)\%$	$(57.05 \pm 10.58)\%$	$(97.76 \pm 1.31)\%$	$(98.48 \pm 0.89)\%$	$(01.52 \pm 0.89)\%$	$(71.63 \pm 8.6)\%$
[g]	$(98.05 \pm 1.37)\%$	$(62.86 \pm 11.84)\%$	$(98.76 \pm 0.82)\%$	$(99.01 \pm 0.69)\%$	$(0.99 \pm 0.69)\%$	$(76.18 \pm 9.91)\%$
[h]	$(93.23 \pm 3.76)\%$	$(69.40 \pm 24.19)\%$	$(86.83 \pm 20.53)\%$	$(93.47 \pm 3.77)\%$	$(06.53 \pm 3.77)\%$	$(79.59 \pm 15.24)\%$
[i]	$(93.48 \pm 4.09)\%$	$(72.69 \pm 25.26)\%$	$(87.44 \pm 20.74)\%$	$(93.68 \pm 4.12)\%$	$(06.32 \pm 4.12)\%$	$(81.85 \pm 15.77)\%$

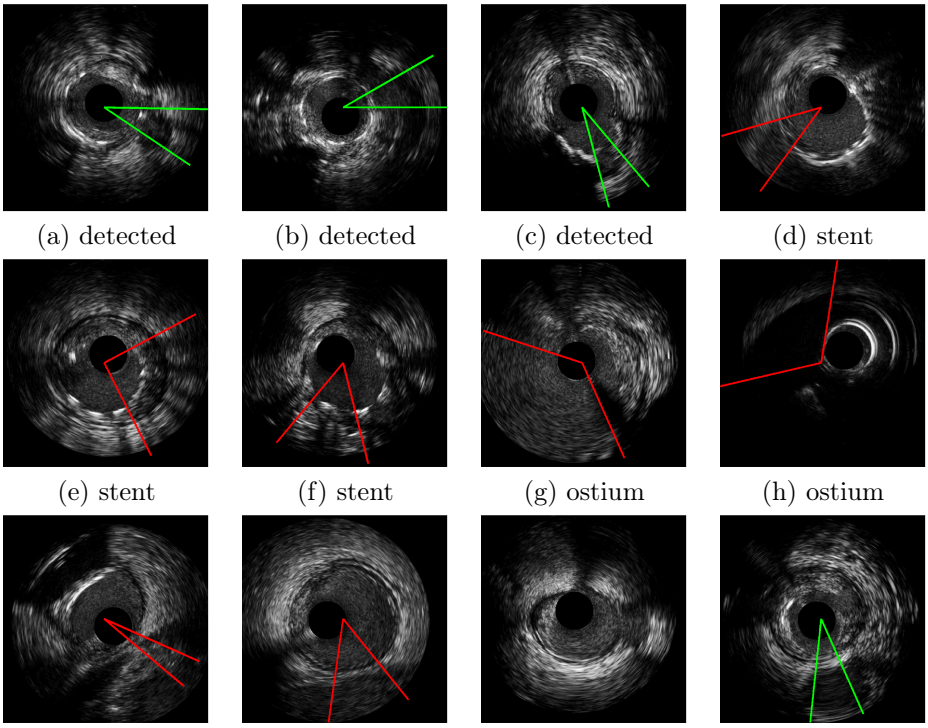

(a) detected (b) detected (c) detected (d) stent

(e) stent (f) stent (g) ostium (h) ostium

(i) vein (j) vein (k) small (l) unlabeled

Figure 3.7: Analysis of bifurcation detection results. The convex angles in green and red correspond to the angular extension of the bifurcation as identified by the algorithm, in case of correct detection and false positive error, respectively.

branching region (*angular sectors*). The score is low for the small bifurcation regions in the data-set, while it reaches a stable 100% for the large branching regions, covering more than 40 *angular sectors.* Therefore, it can be stated that the method is highly reliable for medium and large branchings.

In Figure 3.9, examples of ground-truth labels and corresponding final result maps are illustrated. In most cases the bifurcation regions which are labeled in the ground-truth are correctly detected, while the main limitation lies in the possible identification of false positive branching regions.

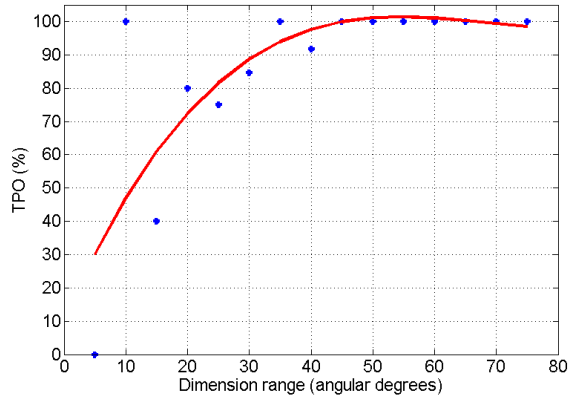

Figure 3.8: Average TPO score for 15 equally spaced ranges of bifurcation angular extension. In the considered data-set, the bifurcation angle ranges between 3 and 72 degrees. The data distribution is approximated as a third-order polynomial, shown in red.

3.4.3 Discussion on Methodology

The use of image-based gating cannot ensure that the scan line followed over the longitudinal view actually represents the same orientation relative to the vessel. However, the measurements of bifurcation angular extension and position relative to the IVUS acquisition are clinically relevant because they are used by physicians to characterize the branches and their position with respect to the plaque location.

The choice of introducing the 2-D+T context in the classification domain instead of in the feature domain is motivated by the fact that along the longitudinal (temporal) dimension of the IVUS sequences, bifurcations can significantly change their appearance, so 2-D+T descriptors would not be coherent. On the contrary, the MSSL scheme does not take into account the appearance, but the *pseudo-probability* of bifurcations.

3.5 From Detection to Signal Extraction

In this chapter, a new 2-D visualization map for IVUS sequences is presented, in the space (θ, t), where θ is the angular position (orientation) with respect to the IVUS acquisition and t is the longitudinal (temporal) position along the pullback. This map summarizes, in a compact representation, the vessel morphological characteristics regarding the branchings.

Additionally, the output of the bifurcation detection framework can be used to obtain 1-D longitudinal profiles which represent the angular amplitude of the branchings, as a function of the position t (i.e., the frame number). Such profiles are obtained

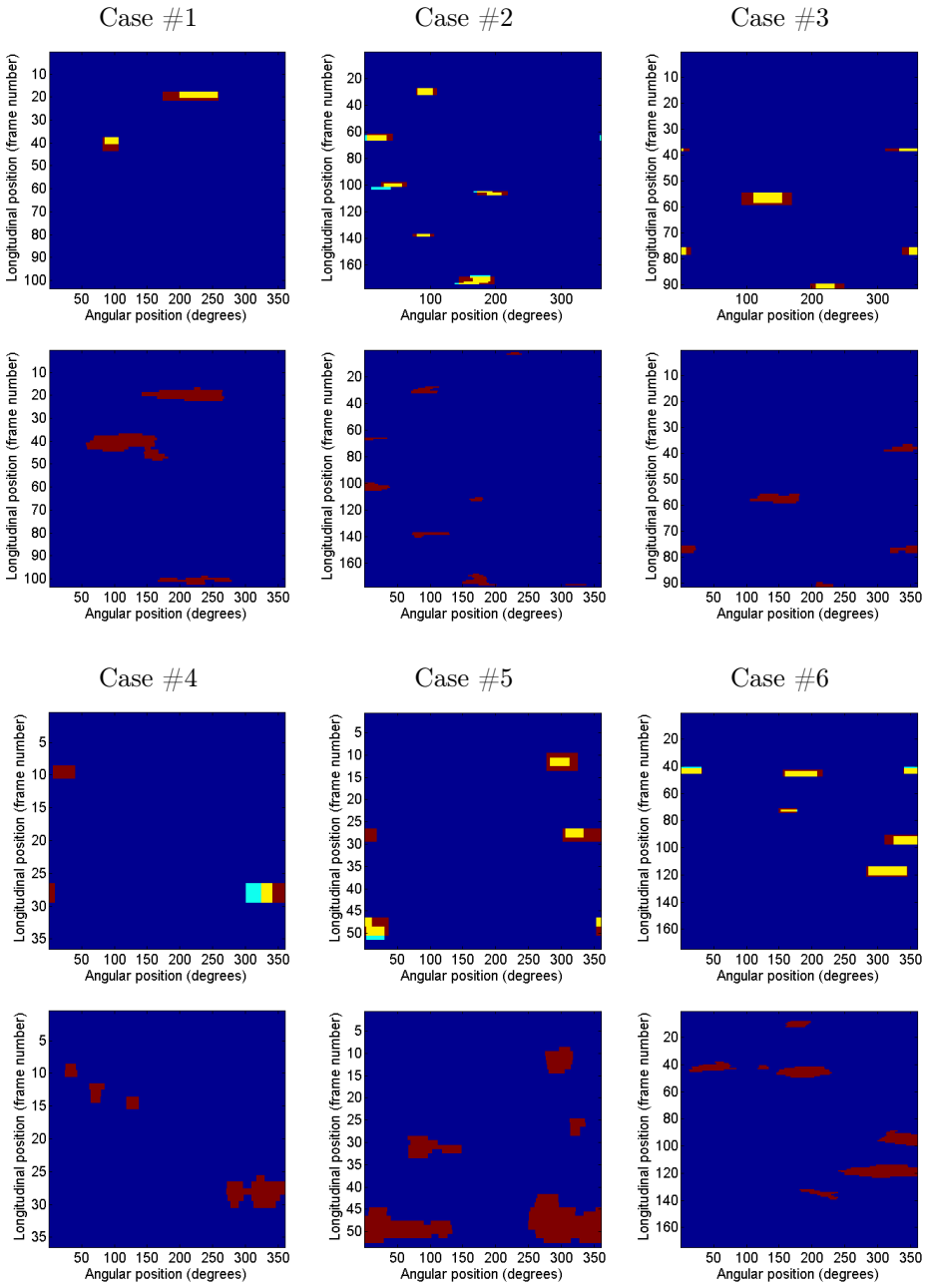

Figure 3.9: Manual segmentations performed by the two medical experts, in red and cyan, respectively, and their intersection, in yellow (first row). Corresponding results of the automatic method, with the detected branchings in red (second row).

by computing, for each longitudinal position, the corresponding total angular extension of the bifurcations. Several examples are illustrated in Figure 3.10. The angular extension of the branchings can be related to the size of the side-branch vessels, therefore these profiles provide a morphological description of the vascular structure. This information will be exploited in Chapter 4, where the proposed alignment method is based on signals describing the vessel morphology.

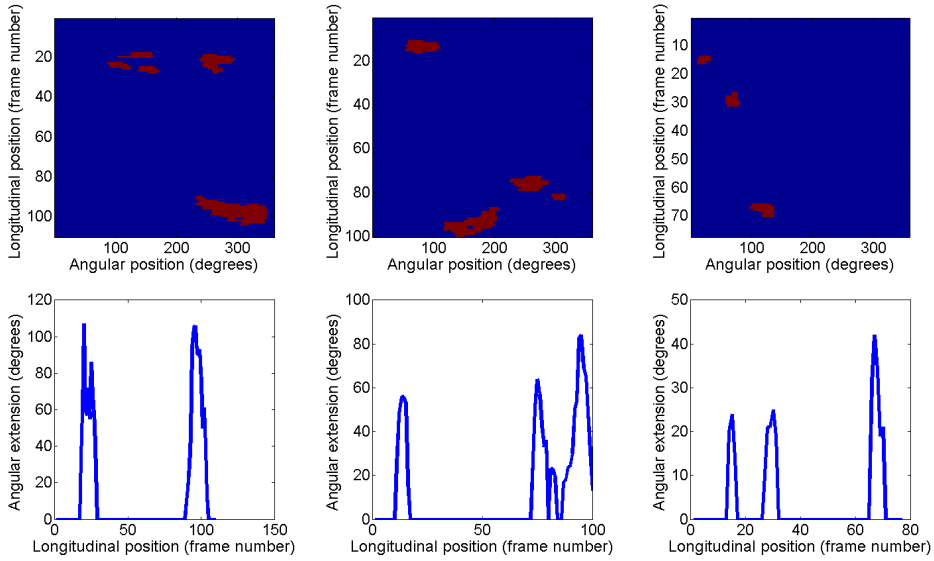

Figure 3.10: Result maps of the automatic method, with the detected branchings in red (first row) and corresponding morphological signals of bifurcation angular extension (second row).

3.6 Conclusions

In this chapter, a fully automatic method for identifying the longitudinal and angular bifurcation position and extension in IVUS sequences is presented. Although the branching detection task is particularly challenging due to the high variability in bifurcation dimensions and appearance, as demonstrated by the F-Measure scores of 71.63% and 76.18% for inter and intra-observer variability respectively, the proposed approach reaches an F-Measure of 86.35% (sensitivity 80.66% and precision 94.60%) and a TPO of 90.97%. Satisfactory results are obtained in most frames, while the performance slightly decreases when stent, vein, ostium and small bifurcation frames are analyzed.

The proposed methodology provides a tool for the quick review of pullback sequences, making bifurcation inspection more intuitive and facilitating the evaluation of the lesion at bifurcation sites. A bi-dimensional visualization of the pullback is in-

troduced. Finally, the output of the method allows to extract longitudinal (temporal) morphological signals which describe the vessel.

Chapter 4

Automatic Non-Rigid Temporal Alignment of IVUS Sequences

4.1 Introduction

The alignment of IVUS pullbacks is required at several stages of the clinical pipeline. First of all, after performing PCI, physicians need to assess the outcome of the intervention (i.e., evaluate final lumen dimensions and blood flow restoration, inspect stent placement and side-branch occlusion by a deployed stent, evaluate the vessel after plaque removal in case of roto-ablation). Then, at follow-up evaluation, pullback alignment is useful to monitor re-stenosis and the evolution of plaque composition.

Despite the numerous advantages of IVUS, the post-operative analysis and the follow-up of the patient are presently limited, because clinicians usually compare two acquisitions by manually searching for the corresponding frames. Moreover, in clinical studies on plaque regression/progression, the longitudinal correspondence of coronary artery segments is currently determined manually, by identifying common landmarks, such as bifurcations [78, 75, 102, 31, 58]. Additionally, a rigid correspondence of the segments adjacent to the landmarks is often assumed [78, 102]. Considering all these, the advantage brought by a technology that automatically and non-rigidly aligns IVUS sequences is noticeable. Despite the constant speed of the catheter, the automatic alignment of IVUS sequences is hampered by several obstacles. IVUS acquisitions are subject to motion artifacts due to the catheter movement and the arterial pulsation, such as the longitudinal swinging of the catheter and the roto-translation of successive frames of the pullback. The vessel cyclically expands and contracts due to pressure changes during the heart cycle, hence in different acquisitions diastole and systole could not correspond to the same physical locations. The rotation of the probe with respect to the vessel can vary and the catheter may follow different trajectories with respect to the vessel walls, hence the imaged sections are not necessarily orthogonal to the vessel walls. The ultrasound beam may be reflected by the guidewire and may

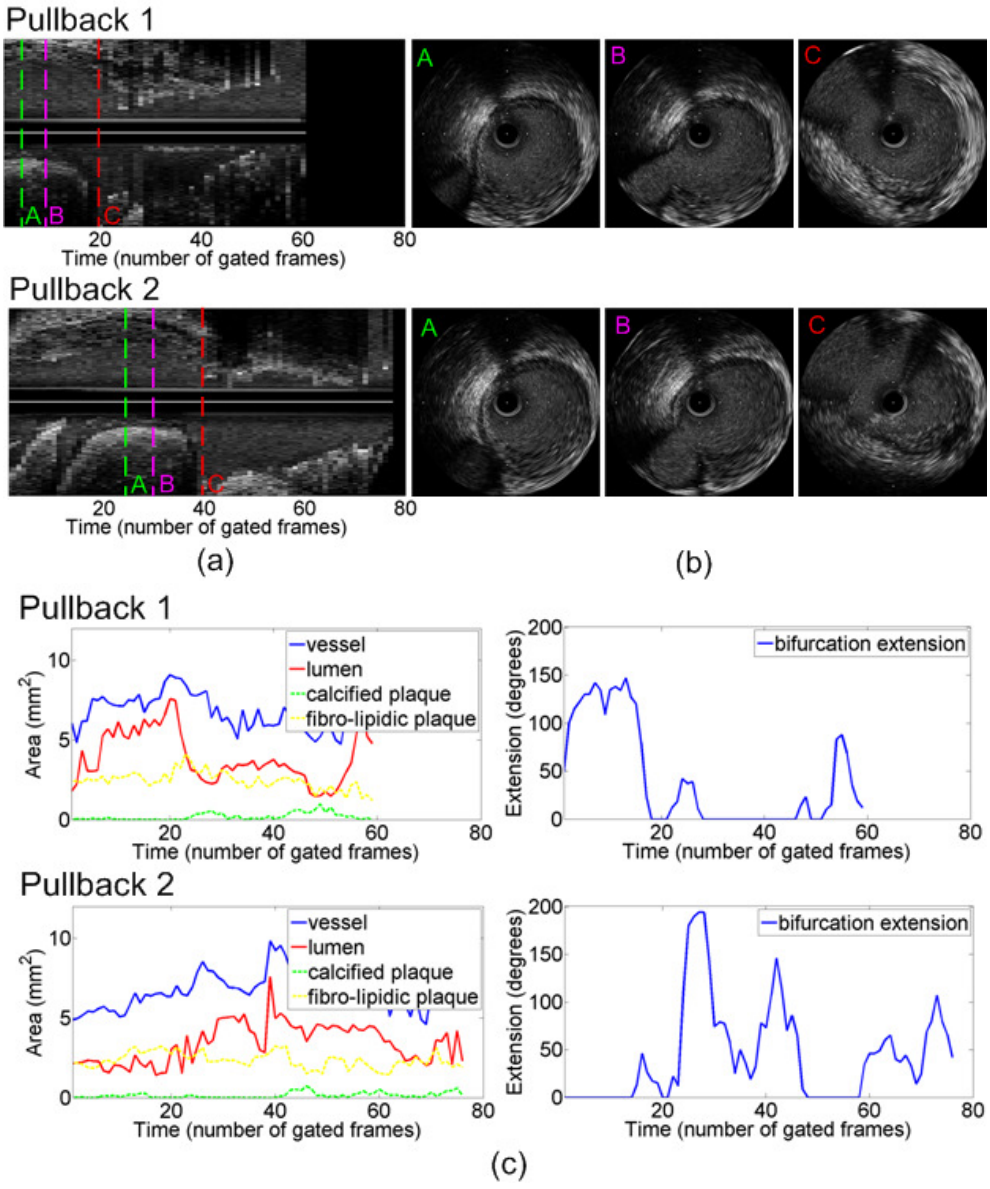

Figure 4.1: Pair of IVUS sequences of the same vessel: (a) *longitudinal views*, (b) *short-axis views* of corresponding frames and (c) morphological signals describing the pullbacks.

result in bright echoes and shadows in the IVUS images [19]. Guidewire artifacts can vary their appearance and orientation in different acquisitions. The catheter flexibility causes non-rigid deformations of the pullbacks. Moreover, the probe can first remain stuck in the vessel for some time and then accelerate. Since the pullbacks may have different initial and final spatial positions along the vessel, the overlapping of corresponding vascular segments is often partial (see Figure 4.1(a)). In fact, two corresponding vessel segments may have different overall lengths (in terms of number of frames) in different acquisitions. Finally, the vessel can undergo significant morphological changes after the intervention (for instance, stent deployment and post dilation change the lumen and vessel area) or evolve at follow-up. As a consequence, a one-to-one correspondence between frames of the two pullbacks cannot be found, making image-based registration approaches inaccurate. Hence, in this chapter the IVUS alignment task is addressed as a feature-based temporal alignment problem, in which the morphological content of the artery is exploited. In the proposed approach the IVUS sequences are described by temporal morphological signals, i.e., side-branch location, vessel, lumen and plaque areas (see Figure 4.1(c)).

In different applications, such as speech recognition, chromatography, activity recognition and shape matching, several methods have been developed for non-rigid signal alignment, like Dynamic Time Warping (DTW), Canonical Time Warping (CTW) and Correlation Optimized Warping (COW) [94, 122, 77]. DTW [94] minimizes the Euclidean distance of corresponding points of the signals. CTW [122] extends DTW by combining it with a Canonical Correlation Analysis step (CCA), which provides a feature weighing mechanism and allows the alignment of signals with different dimensionality. The combined use of DTW and CCA can improve the accuracy of the results, but may also yield worse performance than the baseline DTW [101], and the benefits depend on the application. CTW has higher computational complexity than DTW, due to the iterative use of CCA required by the optimization process. COW [77] is a piecewise data alignment method. Two sequences are aligned by dividing them into segments and allowing limited changes in segment lengths. The final segment lengths are selected so as to optimize the overall correlation between the sequences. The problem is solved as a segment-wise correlation optimization by means of dynamic programming. The solution space is defined by two parameters: the initial segment length Seg and the maximum segment length increase or decrease, $Slack$.

On the other hand, different methods have been proposed for matching of symbolic sequences, i.e., strings of characters. Some examples are the techniques for solving the Longest Common Subsequence (LCSS) and the Approximate String Matching (ASM) problems and the Smith-Waterman algorithm [25, 99, 105]. Given a query and a target strings, LCSS [25, 114] determines their longest common subsequence, i.e., finds subsequences of the query and target that best correspond to each other. The distance between the two sequences is computed based on the ratio between the length of their longest common subsequence and the length of the whole sequence. The aim of ASM methods is to identify the subsequence of a text most similar to a given pattern, i.e., whose Levenstein distance to the pattern is minimal [99, 76]. Levenstein distance measures the difference between two strings as the minimum number of char-

acter insertions, deletions and substitutions needed to make them equal. Finally, the Smith-Waterman algorithm, originally proposed for identification of common molecular subsequences [105], is a local alignment algorithm that matches two sequences by using dynamic programming. Smith-Waterman finds similar subsequences without exhaustive search.

In order to address the non-rigid correspondence between IVUS frames, in this chapter a DTW-based framework is adapted to the specific clinical task. The DTW alignment technique is applied to multidimensional morphological signals. Ad-hoc improvements are introduced into DTW: a regularization term is applied to penalize significant differences in the global temporal expansion/compression of IVUS sequences. To tackle the problem of partial overlapping, two alternative strategies are proposed.

A first strategy consists in the integration of the DTW algorithm into a Sliding Window (SW) approach. The two sequences are iteratively slid one along the other and, for each step, the alignment between the overlapping subsequences is identified. The optimal sliding iteration is selected by minimizing a matching cost. However, The SW approach has two main limitations. First, corresponding IVUS subsequences must have the same length in terms of number of frames. Second, DTW is iteratively applied to different pairs of subsequences in order to identify the optimal corresponding subsequences, resulting in high computational cost. Therefore, the SW approach is improved and completed by proposing a different solution for handling partial overlapping. The developed Extremes of Path Search (EPS) strategy overcomes the rigid constraint forcing the selected matching segments to be of the same length, and it reduces the computational complexity with respect to the SW strategy. The EPS solution combines the DTW and ASM approaches, taking advantage of the most suitable characteristics of both techniques while overcoming their limitations. In fact, on one hand, DTW uses the Euclidean distance as a dissimilarity measure, which is adequate to continuous sequences, while ASM uses the Levenstein distance, originally proposed for strings. Levenstein distance is not directly applicable to numeric sequences, since a threshold is required to determine when two numeric values are equal, and performance will heavily depend on the threshold setting. On the other hand, DTW has the constraint of computing a global matching between the whole sequences, while ASM can handle partial overlapping of sequences through an ad-hoc initialization strategy. EPS exploits an initialization inspired by ASM to tackle partial overlapping, but using the Euclidean distance as a dissimilarity measure, which is adequate to continuous sequences, like DTW. In the EPS strategy, firstly the extremes of the corresponding subsequences are identified on the two sequences. Then, the selected matching subsequences are aligned by means of DTW.

An extensive validation of our IVUS alignment framework is performed, both on synthetic and *in-vivo* data. In the case of the *in-vivo* data, two different sets with different complexity are created, consisting of 42 total IVUS pullbacks acquired from 21 different patients. Qualitative results of the identified pairs of corresponding frames are illustrated and the performance and robustness of the method in case of stent deployment are discussed. To conclude the chapter, the developed tool for

the visualization of the automatic results is described and a sample screen-shot is displayed.

4.2 Method for IVUS Sequences Alignment

4.2.1 Multidimensional Profiles Framework

A pair of corresponding IVUS sequences is described by temporal morphological profiles (i.e., signals describing the evolution of morphological measurements along the vessel) and defined as a pair of time series $X \in \mathbb{R}^{dim \times n_x}$ and $Y \in \mathbb{R}^{dim \times n_y}$, of length n_x, n_y and dimensionality dim. The morphological profiles used in this study are listed in the following paragraphs.

Gating Preprocessing The heart beating generates undesired artifacts in IVUS acquisitions, disturbing the computation of the morphological measurements, such as catheter swinging effect and cyclical vessel pulsation. In this study, an image-based gating technique is applied [37] to select the frames belonging to the end-diastolic phase, as described in Chapter 2. The gated images provide coherent morphological measures, since in end-diastole the arterial tissues are subject to the same blood pressure.

Profile Extraction In this study, the following morphological measurements are proposed: (1) vessel area, defined as the area inside the media-adventitia border, (2) lumen area, (3) area of calcified plaque, (4) area of fibro-lipidic plaque, (5) angular extension of vascular bifurcations. Such signals can be manually or automatically extracted. In this study, the profiles are automatically computed using state-of-the-art algorithms, as follows: the vessel area is computed by means of the method proposed in [22], while the lumen area is computed by exploiting the method proposed in [6]. In the computation of the tissue areas, three classes of plaque can be discriminated using [20]: calcified, fibrotic and lipidic. The identification of the necrotic plaque is still not reliable in IVUS, as demonstrated by [109, 74, 95]. Hence, this class has not been considered in the plaque characterization algorithm. Additionally, since in the analyzed data-sets the lipidic samples are few, inhomogeneous and scattered into the fibrotic area (no lipidic pools are present), the profiles of lipidic plaque would not be reliable and would contain outliers. Therefore, the fibrotic and lipidic areas are combined into a single region, to obtain a consistent representation of the vessel morphology. Finally, a method for the automatic detection of the position and the angular extension of vascular branching in IVUS is applied [2], as described in Chapter 3.

The chosen morphological profiles are invariant to frame rotation, thus making the method independent of the catheter torsion. The use of multiple features is aimed to increase the robustness with respect to 1-D alignment, by capturing different aspects of the vessel morphology, in particular increasing the robustness to modifications due

to surgical intervention. It might be noticed that the proposed alignment framework is independent of the technique employed for the measurements and could potentially be extended by using a different set of morphological profiles.

4.2.2 IVUS Alignment Framework

The DTW algorithm The proposed signal alignment framework is based on the DTW technique. To align two sequences $X = [x_1, x_2, \dots x_{n_x}]$ and $Y = \left[y_1, y_2, \dots y_{n_y}\right]$ DTW builds a matrix $d_{(n_x \times n_y)}$, where $d(i,j)$ represents a dissimilarity measure between $X(i)$ and $Y(j)$ [94]. In the classical DTW formulation, $d(i,j)$ is computed as the Euclidean distance. In the case of a multidimensional alignment, the distance $d(i,j)$ is:

$$d(i,j) = \sqrt{\sum_{idim=1}^{dim} \left(x_i^{idim} - y_j^{idim}\right)^2}, \tag{4.1}$$

where $idim$ is one of the dimensions of X and Y. The different dimensions of the sequences are normalized independently of each other. Successively, the Minimum Cumulative Distance (MCD) matrix D is computed by dynamic programming as follows:

$$D\left(i,j\right) = d\left(i,j\right) + min(D\left(i-1,j\right), D\left(i-1,j-1\right), D\left(i,j-1\right)). \tag{4.2}$$

The first row and the first column of the MCD matrix D are initialized with cumulative values as follows:

$$\begin{cases} D(i,1) = D(i-1,1) + d(i,1), & i \in \{1,2,\dots,n_x\} \\ D(1,j) = D(1,j-1) + d(1,j), & j \in \{1,2,\dots,n_y\} \end{cases} \tag{4.3}$$

The last element of the matrix represents the *matching cost,* i.e., the minimal cumulative distance between X and Y:

$$\Phi\left(X,Y\right) = D(n_x, n_y). \tag{4.4}$$

Finally, the algorithm finds the *warping path* (a mapping of the time axes of X and Y on a common time axis, $\mathbf{wp} = \langle [i(k), j(k)] \,|k = 1, \dots, K\rangle$) by computing a *backtracking* (a path from the bottom-right cell (n_x, n_y) to the top-left cell $(1,1)$ of D by following the minimum values of the neighboring cells), as illustrated in Figure 4.2.

Regularization Cost (RC) In this study, a regularization term is introduced in the DTW alignment framework. Such regularization strategy is inspired by the *band*

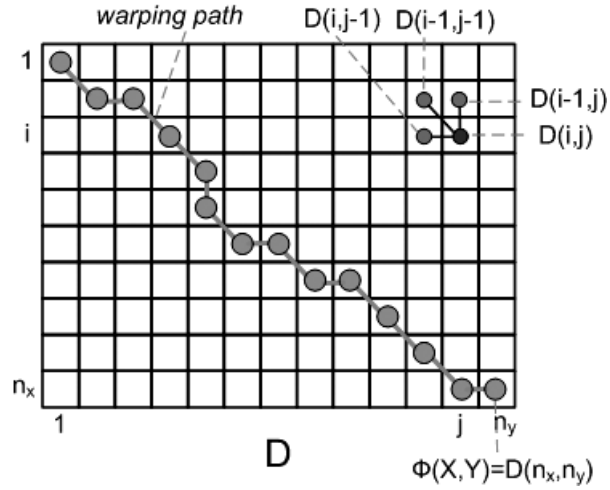

Figure 4.2: Example of MCD matrix D and *warping path* for two sequences of length n_x, n_y.

constraint used in the classical version of DTW [94], where the *warping path* is guided, by limiting its acceptable domain to a band around the diagonal of the dissimilarity matrix. Similarly, in this study, a penalization is applied to non-diagonal transitions in the *warping path* (one-to-many correspondences among frames) [47, 88], to avoid an excessive presence of horizontal and vertical transitions, which would represent non-physiological temporal compression/expansion of the two IVUS sequences. As a result, the smoothness of the output *warping path* increases. With respect to [94], which sets the *band constraint* to a constant width, thus fixing a threshold, in the proposed solution the regularization is directly integrated into the dynamic programming computation: non-diagonal transitions of the path are uniformly given a higher cost (*regularization cost*, RC) in computing the MCD matrix. The MCD leading to the entry (i, j) is aimed to reduce the alignment error when the profiles are affected by noise corruption, as:

$$D(i,j) = d(i,j) + min\{(D(i-1,j) + C, D(i-1,j-1),\ D(i,j-1) + C\}\,, \quad (4.5)$$

where the parameter C represents the direction penalty. The value of C is tuned by cross-folding. The data-set is divided into N subsets (denoted as folds), and for each fold the value of the parameter is optimized over the other (N-1) folds. Then, the optimized value is applied to the considered fold. The proposed regularization is aimed to reduce the alignment error when the profiles are affected by noise corruption, as shown in Figure 4.3.

Partial Overlapping Strategy The typical limitation of the DTW approach is the computation of a global matching between the whole sequences, forcing the extremes

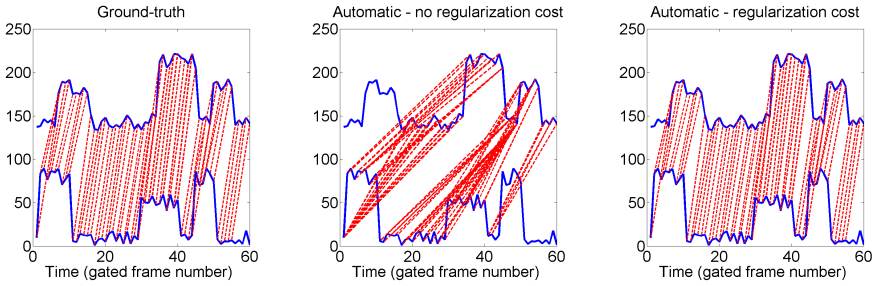

Figure 4.3: Example illustrating the alignment of noise-corrupted signals. In (a) ground-truth, in (b) incorrect alignment obtained by the classical DTW version, in (c) correct alignment obtained by applying RC. The blue lines represent the signals and the red lines represent correspondences between frames.

to correspond in the *warping path* (*boundary condition* constraint) [94]. A potential problem arises when the two sequences partially overlap, i.e., when a sequence matches only to a subsequence of the other sequence. This is the typical condition for IVUS pullbacks, due to the possible variation in the starting and final positions of the probe along the vessel during acquisition (see Figure 4.1). Two strategies are possible to tackle this issue.

Sliding Window (SW) Approach A first strategy is proposed with the goal of increasing robustness to partial overlapping. The solution consists in the integration of the DTW alignment algorithm into a Sliding Window (SW) approach. The two sequences X and Y are iteratively slid one along the other (see Figure 4.4) and for each step the alignment between the overlapping subsequences is identified by means of DTW. The optimal sliding iteration, $iter_{optimal}$, is selected by minimizing a *matching cost*:

$$iter_{optimal} = \underset{iter}{argmin} \Phi_{NORM}\left(X_{iter}, Y_{iter}\right), \tag{4.6}$$

where:

$$\Phi_{NORM}\left(X_{iter}, Y_{iter}\right) = \Phi\left(X_{iter}, Y_{iter}\right) / l_{iter}, \tag{4.7}$$

being X_{iter} and Y_{iter} the overlapping subsequences and l_{iter} the overlapped length, i.e., the length of the overlapping window at the sliding iteration $iter$. It can be observed that the overlapping subsequences are constrained to have the same length on X and Y. In order to decrease the computational cost, the number of iterations N_{slide} is restricted by limiting the subsequence of the shortest sequence which remains outside the window to a maximum length, w_{elast}.

Extremes of Path Search (EPS)

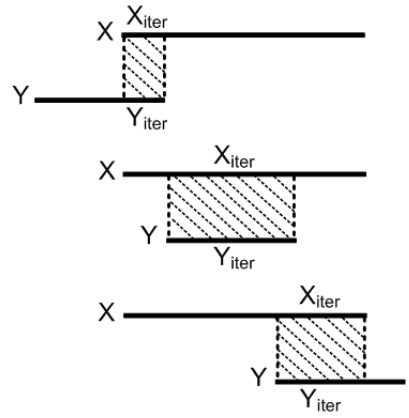

Figure 4.4: Three examples of sliding positions for an idealized couple of sequences (X, Y) (continuous lines). At each iteration *iter*, X_{iter} and Y_{iter} are the overlapping subsequences of X and Y, respectively. The overlapping window is indicated by diagonal traits.

An alternative strategy to handle partial overlapping is proposed. Extremes of Path Search (EPS) integrates an initialization inspired by the ASM techniques [99, 76]. The ASM problem has been originally posed for discrete string matching and consists in identifying the subsequence of a text which is most similar to a given pattern string (as well as the starting position and the extension of the subsequence). In the dynamic programming solution to ASM [99], the first row of the dynamic programming matrix (Equation 4.3), corresponding to the text, is initialized with zeros so that the pattern can start with zero error at any position in the text.

Following the same idea, in the proposed EPS technique, the first row and column of the MCD matrix D (Equation 4.3) are initialized as follows:

$$\begin{cases} D(i,0) = 0, & i \in \{1, 2, \ldots, n_x\} \\ D(0,j) = 0, & j \in \{1, 2, \ldots, n_y\} \end{cases} \tag{4.8}$$

In the classical DTW approach, the *end of match* (i.e., the final point of the *warping path*) corresponds to the last element of the D matrix (n_x, n_y), which represents the *matching cost* $\Phi(X, Y)$ (Equation 4.4). Since in our case the two matching sequences are partially overlapped, the *end of match* can be selected as the minimum value between last row and last column of the matrix D_{NORM}, obtained by normalizing the MCD matrix D by the diagonal distance L (see Figure 4.5):

$$\begin{gathered} \Phi_{EPS}(X, Y) = \underset{i,j}{argmin}(D_{NORM}(i, n_y), D_{NORM}(n_x, j)), \\ i \in \{1, 2, \ldots, n_x\}, j \in \{1, 2, \ldots, n_y\}. \end{gathered} \tag{4.9}$$

In the general case of IVUS images, one of the pullbacks is not completely con-

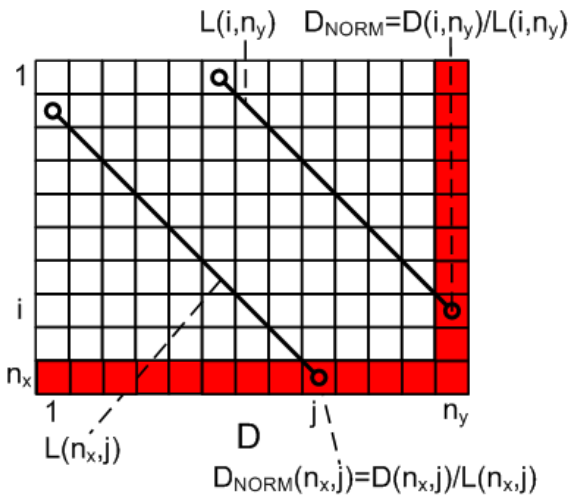

Figure 4.5: Detailed scheme of *end of match* search.

tained in the other, but there is a mutual overlap of two sequences. Both sequences are allowed to match to only a subsequence of the other, and there is no distinction between the roles of the two sequences, such as the text and pattern roles in ASM.

Consequently, the search of the *end of match* is repeated twice, first assessing the final frames $\left(x_{f_x}, y_{f_y}\right)$ of the match between X and Y, then inverting the signals ($X' = [x_{n_x}, x_{n_x-1}, \ldots, x_1]$, $Y' = \left[y_{n_y}, y_{n_y-1}, \ldots, y_1\right]$) and searching for the initial frames $\left(x_{i_x}, y_{i_y}\right)$ of the match, as illustrated in the block diagram in Figure 4.6(a).

Finally, the *warping path* (non-linear alignment) between the selected matching subsequences $X_{sub} = [x_{i_x}, x_{i_x+1}, \ldots, x_{f_x}]$ and $Y_{sub} = \left[y_{i_y}, y_{i_y+1}, \ldots, y_{f_y}\right]$ is obtained by applying the DTW algorithm, as shown in Figure 4.6(b), between the initial $\left(x_{i_x}, y_{i_y}\right)$ and the final element $\left(x_{f_x}, y_{f_y}\right)$ of the match.

EPS results in a more compact strategy for handling the partial overlapping problem with respect to the SW approach, because it is directly embedded into the DTW technique. Additionally, the initial and ending frames of a correspondence need to be computed only once. Hence, given that the computational complexity of the DTW algorithm is $\mathcal{O}(n_x n_y)$, the computational complexity of EPS is $\mathcal{O}(3n_x n_y)$, while for the SW approach it is $\mathcal{O}((n_x + n_y)n_x n_y)$, where n_x and n_y are the number of gated frames of X and Y (around 100 images).

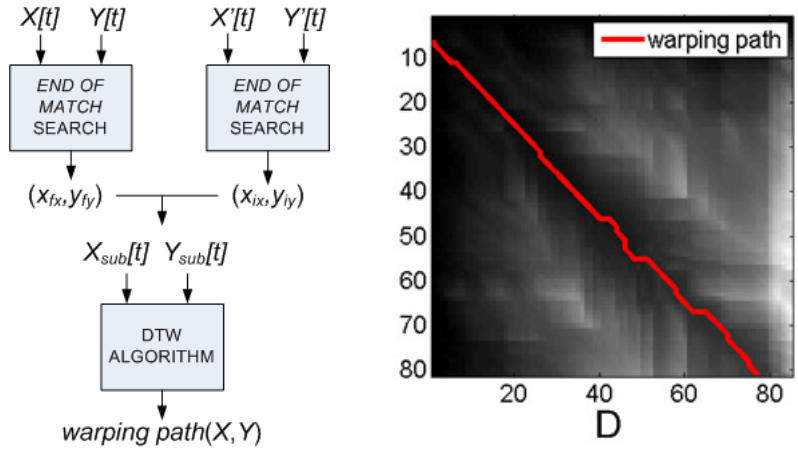

Figure 4.6: (a) General scheme of the EPS approach and (b) example of output *warping path* obtained by the final stage of DTW algorithm, shown superimposed to the MCD matrix D.

4.3 Experimental Results

4.3.1 Materials

A set of IVUS sequences consisting of 42 *in-vivo* pullbacks from human coronary arteries has been used in this study. The sequences have been acquired from 21 patients by means of iLab IVUS Imaging System (Boston Scientific). Sequences have been recorded with constant pullback (0.5 mm/sec). The method has been validated on two different clinical data-sets, consisting of sequences acquired during the same phase of the surgical intervention (Data-set A) and at different intervention stages (Data-set B), respectively. Pairs of corresponding frames have been labeled by a physician. The data-sets and the ground-truth are described in Appendix B.

4.3.2 Methodological Comparison

The performance of the proposed approach is tested by applying the two developed strategies for partial overlapping, and DTW is compared to two other *state-of-the-art* techniques, CTW [122] and COW [77].

To ensure a fair comparison, all the alignment algorithms (DTW, CTW, and COW) will benefit from the following robustness improvements: (1) adapting the original framework [94, 122, 77] to multidimensional signals, using the same weight for the different features, (2) integrating the alignment algorithms into the partial overlapping strategy and (3) applying the path regularization term RC. Regarding (2), the EPS approach has been specifically designed for the DTW technique, hence

Table 4.1: Quantitative results ($MEAN \pm STD$) for E (number of gated frames) on synthetic data, as a function of dim (number of morphological features).

	$dim = 1$	$dim = 2$	$dim = 3$	$dim = 4$	$dim = 5$
CTW	9.36 ± 9.15	4.24 ± 4.28	2.52 ± 2.03	1.87 ± 1.18	1.52 ± 0.63
$CTW - SW$	6.56 ± 9.33	2.53 ± 3.15	1.74 ± 1.95	1.23 ± 0.63	1.12 ± 0.49
$CTW - SW - RC$	5.5 ± 8.32	2.23 ± 2.33	1.55 ± 1.05	1.21 ± 0.59	0.98 ± 0.38
COW	8.01 ± 3.75	9.21 ± 4.16	9.51 ± 4.36	9.78 ± 4.42	9.45 ± 4.16
$COW - SW$	4.36 ± 5.44	2.4 ± 1.31	2.13 ± 0.94	2.09 ± 0.85	2.16 ± 0.88
$COW - SW - RC$	4.05 ± 4.95	2.33 ± 1.22	2.09 ± 0.93	2.02 ± 0.89	1.98 ± 1.04
DTW	9.03 ± 9.45	4.05 ± 4.16	2.4 ± 2.21	1.6 ± 1.02	1.26 ± 0.58
$DTW - SW$	7.54 ± 10.64	3.25 ± 5.28	1.87 ± 2.79	1.2 ± 1.09	0.96 ± 0.41
$DTW - SW - RC$	3.75 ± 5.8	1.79 ± 1.37	1.24 ± 0.77	0.96 ± 0.42	0.8 ± 0.29
$DTW - EPS - RC$	7.04 ± 10.02	2.67 ± 3.97	1.51 ± 2.01	1.04 ± 1.24	0.76 ± 0.29

the other alignment algorithms will employ the SW strategy. A list of all possible combinations is reported in the first column of Table 4.1.

In order to validate the method, the performance of the automatic alignment is evaluated in terms of the *alignment error* E, defined as the distance between the ground-truth reference and the output *warping path*. E is computed as the average error for all the ground-truth points and is expressed in number of gated frames. The evaluation is performed using both synthetic data with applied controlled distortion and *in-vivo* data.

4.3.3 Experiments on Synthetic Data

Synthetic Morphological Signals Pairs of sequences (X, Y) are synthetically generated by modifying the morphological profiles extracted from *in-vivo* pullbacks. The scheme in Figure 4.7 summarizes the applied types of distortion:

1. Amplitude distortion: additive zero-mean random noise is applied to the morphological profiles. The noise amplitude w_1 is computed as a percentage of the mean value of the signal (Figure 4.7(a)).

2. Partial overlapping: a portion of the original sequence is selected, whose length is a percentage w_2 of the initial profile (Figure 4.7(b)).

3. Temporal distortion: a temporal expansion/compression generates vertical or horizontal transitions in the *warping path*, i.e., multiple correspondences between the frames of X and Y. Three cases can be distinguished, in which are randomly introduced:

   (a) the same number (w_3) of multiple correspondences from X to Y and vice-versa (Figure 4.7(c)). A randomly generated time transformation matrix

for time warping is used, M_T, as in [122]. M_T is initialized as $M_T = I_n$, where n is the length of the matching portions of the signals. Then, w_3 columns of M_T are randomly chosen and replicated and w_3 columns are randomly chosen and deleted.

(b) w_4 additional multiple correspondences from X to Y (Figure 4.7(d)).

(c) w_5 additional multiple correspondences from Y to X (Figure 4.7(e)).

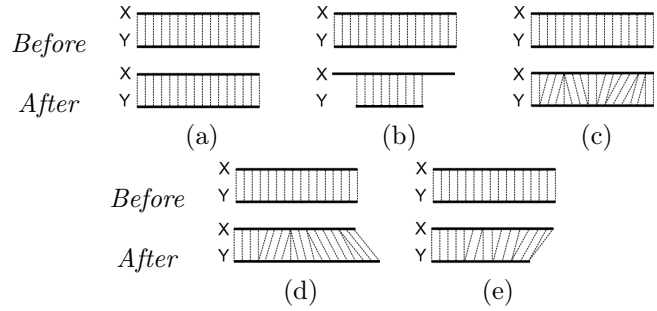

Figure 4.7: Idealized pairs of sequences (X, Y) (continuous lines), and frame-to-frame correspondences (dotted lines), before and after the distortion simulation: (a) amplitude distortion, (b) partial overlapping, (c), (d) and (e) temporal distortions.

The parameters w_1, w_2, w_3, w_4, w_5 model the signal distortion simulation. Their default values and ranges, which represent average *in-vivo* conditions and realistic variations, respectively, are suggested by a medical expert and empirically measured on the whole ground-truth: $w_1 = (100 \pm 100)\%$, $w_2 = (75 \pm 25)\%$, $w_3 = 60$ $(0 - 120)$ frames, $w_4 = 5$ $(0 - 20)$ frames, $w_5 = 0$ $(0 - 20)$ frames.

The tuning of the parameters of the alignment methods, Seg, $Slack$, w_{elast} and C, is performed by minimizing the mean value of E over $N_{exp} = 40$ experiments, setting the distortion parameters to default values. The parameters are estimated by exhaustive search: $Seg \in [16, 30]$, $Slack \in [6, Seg - 9]$, $w_{elast} \in [0, 35]$ and $C \in [0, 0.1]$. It is worth noticing that both DTW and CTW are fully automatic, while COW requires the setting of the initial segment length Seg and the maximum segment length variation $Slack$.

A first synthetic experiment focuses on assessing the robustness of the framework to variations in the number of morphological features. A second experiment evaluates the robustness to each of the previously described simulated distortions.

Multidimensional Alignment In order to evaluate the robustness of the framework as a function of the number of morphological profiles, E is computed by varying the number of acquired signals dim in the range $[1, 5]$. Pairs of synthetic signals are generated by setting w_1, w_2, w_3, w_4, w_5 to default values. For each value of

$dim \in [1, 5]$, all the possible feature combinations are tested and then the error is computed as the average by repeating the test $N_{exp} = 40$ times. As expected, Table 4.1 shows that E decreases at the increase of dim. The error reduction is particularly significant when more than one signal are considered, confirming the interest of a multidimensional extension of the method. Similarly, all the methods improve their robustness when combined with RC and partial overlapping strategies (SW or EPS). As observed by comparing the last two columns of Table 4.1, when the number of features is high (more than four) the *DTW-SW-RC* and the *DTW-EPS-RC* approaches have comparable performances and they are both superior with respect to *CTW-SW-RC* and *COW-SW-RC*. On the other hand, for a low number of features *DTW-SW-RC* is the most robust approach.

Robustness to Signal Noise and Distortion In the second set of experiments, the robustness of the framework to noise and distortion is assessed. Figure 4.8 shows E as a function of the distortion parameters $w_{1...5}$. When one of the distortion parameters is varied in the chosen range, the others are set to default values. In general, COW shows the highest error, indicating that a segment-wise alignment is the least suited for the IVUS pullback alignment. The performance of CTW is comparable to DTW, but this latter is computationally less expensive, since CTW requires the iterative use of CCA. It is worth noticing that, in this study, the two sequences have the same dimension (i.e., the same number of morphological profiles), therefore the advantage given by CTW of aligning signals with different dimensionality is not relevant in this application. Moreover, this experiment demonstrates that the partial overlapping strategy is effective, since CTW and COW are robust to partial overlapping only when integrated in the SW framework. Similarly, DTW improves its robustness only when combined with the SW or EPS strategies (see Figure 4.8(b)). The synthetic experiments show that both versions of DTW (embedded into the SW and EPS strategies) are the most performing among *state-of-the-art* algorithms. Regarding the partial overlapping solution, as observed in Figure 4.8(d) and (e), EPS is advantageous over SW in case of temporal distortion of different intensity in the two pullbacks, since it is extremely robust to variations of w_4 and w_5. The performances of SW and EPS are similar with respect to the additive noise w_1, and only for a large amount of noise the SW strategy is slightly superior (Figure 4.8(a)).

4.3.4 Experiments on In-Vivo Data

The *in-vivo* validation is performed on Data-set A, used to reliably validate the proposed method, and on Data-set B, created to reflect the clinical application. The parameter tuning is performed by means of *Leave-One-Patient-Out* (LOPO) cross-validation technique in each data-set, over N folds corresponding to different patients (pullback pairs). For each fold, one of the pullback pairs is iteratively used as test set and the parameters are optimized by minimizing E over all the other pairs.

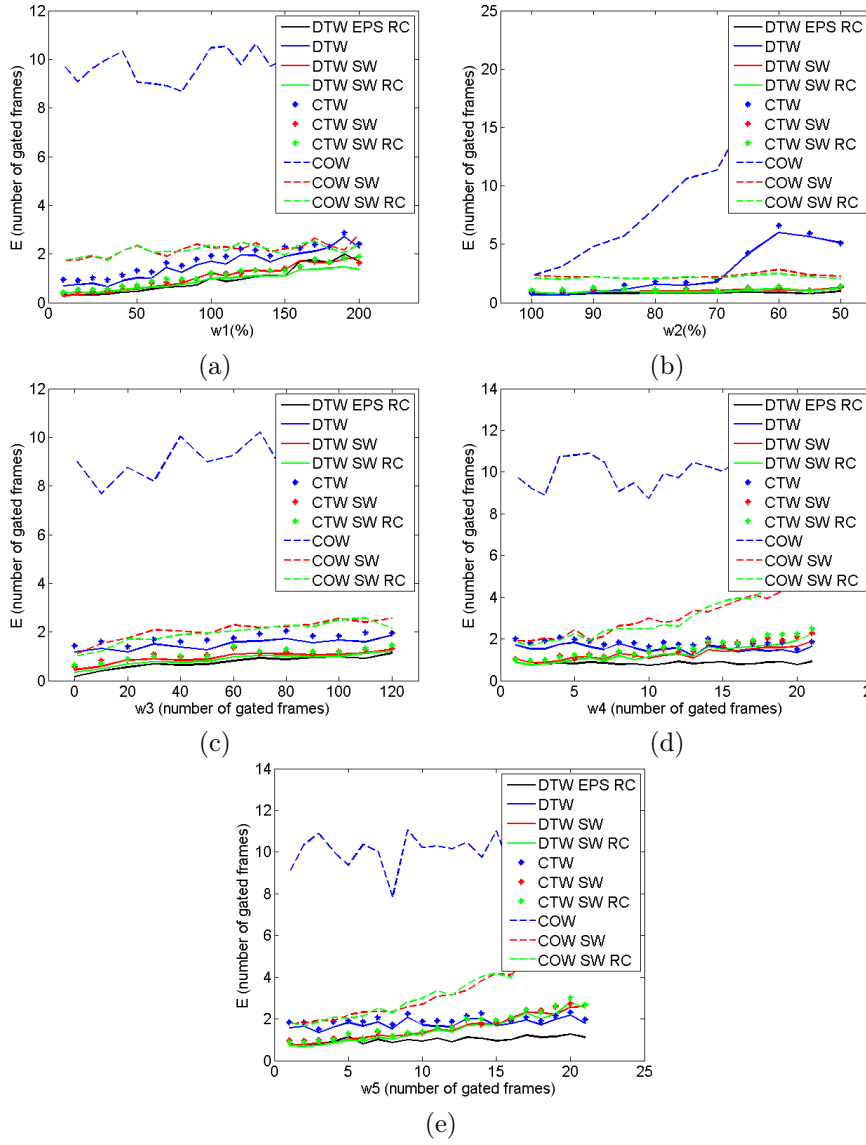

Figure 4.8: E as a function of (a) amplitude distortion w_1, (b) partial overlapping w_2, (c), (d) and (e) temporal distortions w_3, w_4 and w_5.

Table 4.2: Quantitative *in-vivo* results ($MEAN \pm STD$) for E (number of gated frames) on Data-sets A and B.

	$Data-set\ A$	$Data-set\ B$
CTW	2.75 ± 4.11	2.33 ± 1.99
$CTW-SW$	1.33 ± 1.11	2.37 ± 2.92
$CTW-SW-RC$	1.08 ± 0.72	1.56 ± 1.27
COW	6.94 ± 8.19	5.92 ± 3.92
$COW-SW$	2.15 ± 0.98	1.88 ± 0.98
$COW-SW+-RC$	1.83 ± 0.79	2.08 ± 0.8
DTW	2.63 ± 3.72	2.07 ± 2.38
$DTW-SW$	1.19 ± 0.62	2.17 ± 2.72
$DTW-SW-RC$	1.21 ± 0.55	1.47 ± 1.02
$DTW-EPS-RC$	0.85 ± 0.37	1.53 ± 0.92
$inter-observer$		1.2 ± 1.41

Quantitative Results Table 4.2 reports the *in-vivo* results of the compared approaches. Similarly to what observed in the synthetic experiments, DTW can be selected among state-of-the-art alignment techniques for reasons of superior performance and lower computational cost. The statistical significance of the results is evaluated according to the Wilcoxon side-ranks test [28]. At a significance level $\alpha = 0.05$, the null hypothesis that the mean values of the two distributions are equal can be rejected if $z <= 1.96$, where z is the value of the Wilcoxon statistics. The results of the *DTW-EPS-RC* and *DTW-SW-RC* approaches are comparable in both data-sets. Moreover, both *DTW-EPS-RC* and *DTW-SW-RC* reach performances comparable to the inter-observer variability, assessed by using side-branch locations labeled by a second physician, in Data-set B. The direct comparison between the two approaches can be appreciated in Figure 4.9, where the *warping paths*, computed by means of *DTW-SW-RC* (Figure 4.9(a)) and *DTW-EPS-RC* (Figure 4.9(b)), respectively, are superimposed to ground-truth annotations (blue crosses). It can be noticed that errors of the *DTW-SW-RC* alignment are located at the extremes of the *warping path* (where the path becomes vertical in the top-left corner of the image), while in the *DTW-EPS-RC* alignment the *warping path* is smoother and closer to the manual annotation (blue cross in the top-left corner). The incorrect solution is due to the rigid constraint of the SW technique, which forces the matching windows selected on each pullback to be of the same length, in terms of number of frames. Additionally, the computational cost of *DTW-EPS-RC* is lower with respect to *DTW-SW-RC*. Indeed in *DTW-SW-RC*, the DTW algorithm is iteratively applied N_{slide} times, whereas in *DTW-EPS-RC*, only three times.

The quantitative results illustrated in these Sections (both on synthetic and *in-vivo* data) show that the algorithms based on the DTW approach are superior to other state-of-the-art methods. Although comparable performances are obtained by averaging the results of *DTW-SW-RC* and *DTW-EPS-RC*, it can be stated that EPS is the best suited partially overlapping strategy because of its robustness at the

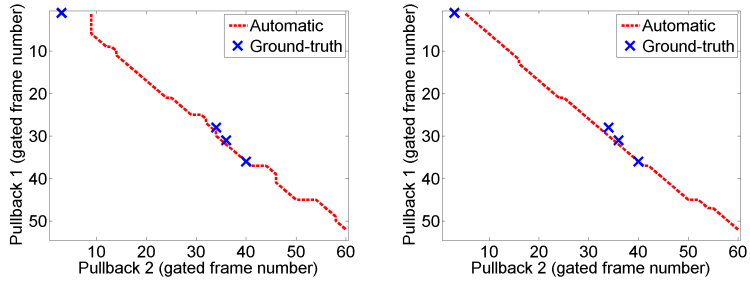

Figure 4.9: Ground-truth and automatic *warping path* for an *in-vivo* pullback pair in Data-set B, computed (a) by *DTW-SW-RC* and (b) by *DTW-EPS-RC*. Note that the closer the red line is to the blue crosses, the smaller the error.

boundary of the matching (Figure 4.9) and for the lower computational cost, hence the most appropriate solution for the IVUS alignment task.

The performance of the chosen method can be further appreciated in Figure 4.10, illustrating the results of the alignment on several pullback pairs from Data-set A (first and second rows) and B (third and fourth rows). The mean value for E is 0.85 gated frames in Data-set A and 1.53 gated frames in Data-set B, which can be estimated as approximately 0.43 and 0.77 mm, respectively.

Qualitative Results The images in Figures 4.11 and 4.12 illustrate several examples of frame-to-frame correspondences identified by *DTW-EPS-RC* in Data-sets A and B, respectively. In order to qualitatively assess the interest of the proposed *non-linear* alignment method, the automatic results are compared to frames identified by considering a *linear* correspondence between pullbacks.

In Data-set A, the rigid matching between frames is simulated by estimating a *linear warping path* as linear regression of the ground-truth landmarks coordinates. Since in Data-set B the landmarks are limited to few side-branch positions, the linear fitting is performed on the *non-linear warping path*.

Figures 4.11 and 4.12 qualitatively compare the automatic and rigid matching results on Data-sets A and B, respectively. The first column of Figures 4.11 and 4.12 reports, for each pair of pullbacks (P1 and P2), a warping matrix in which the ground-truth, the *non-linear warping path* and the *linear* alignment are depicted. The analyzed frame on P1 is indicated by a green horizontal line. The selected frame of P1 (second column), is compared versus the frames of P2 which are identified by *non-linear* (third column) and by *linear* (fourth column) alignment, respectively. As it can be qualitatively observed in Figures 4.11 and 4.12, the *DTW-EPS-RC* technique correctly identifies corresponding frames in both data-sets. A higher similarity between the columns two and three can be visually assessed. In particular, the presence of the same calcifications (Figure 4.11(row 3), Figure 4.12(row 1)), bifurcations

Data-set A

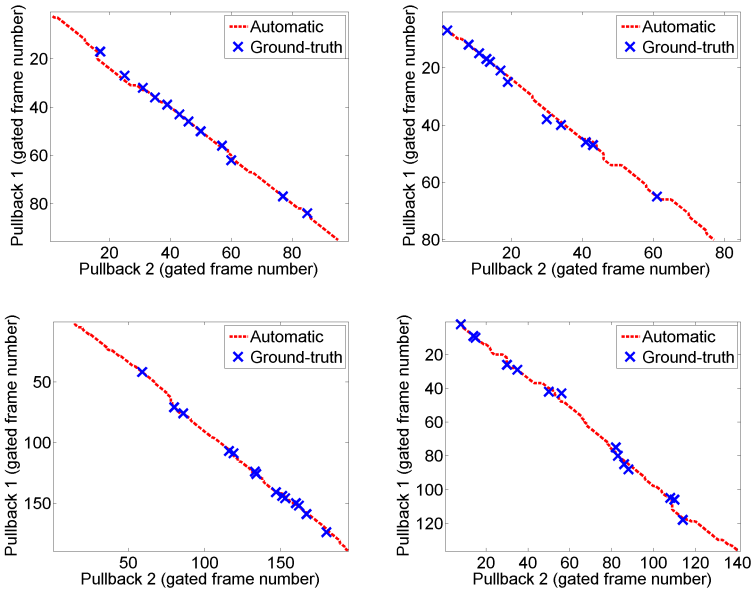

Data-set B

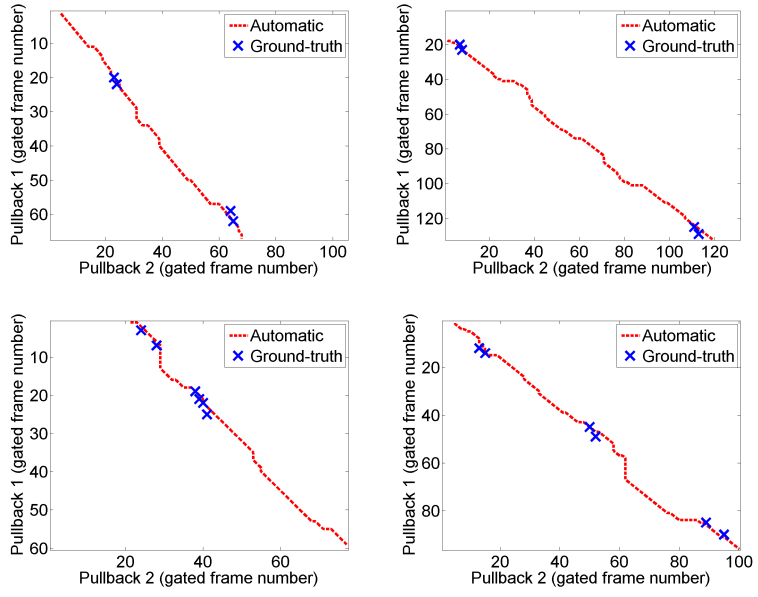

Figure 4.10: Ground-truth and automatic *warping path* for *in-vivo* pullback pairs in Data-sets A and B, computed by *DTW-EPS-RC*. Note that the closer the red line is to the blue crosses, the smaller the error.

(Figure 4.11(row 1), Figure 4.12(rows 2 and 3)), external vessels (Figure 4.11(row 4)), and a similar shape of the vessel structures (Figure 4.11(row 2), Figure 4.12(row 4)) can be recognized.

4.4 Discussion

It must be noticed that in some challenging cases in Data-set B, the morphological changes induced by stent deployment make it impossible to visually compare the corresponding frames extracted from the pullbacks P1 (pre-operative) and P2 (after stent deployment), even for an expert physician. For instance, such ambiguity can be observed in the frames of Figure 4.13, where the changes in vessel appearance caused by stent placement prevent from estimating which of the two frames of P2 (third and fourth columns) is more similar to the corresponding frame of P1 (second column). If we observe the position along the pullback of the two analyzed frames of P1 (first column), it can be noticed that the first frame lies close to the manual landmarks (first row), while the second frame is located in a segment where the landmarks are less dense (second row). In the first case, it is reasonable to believe that the *non-linear* warping is correct, while in the second case it is extremely difficult to assess if the *non-linear* deformation computed by the algorithm is real or if it is an artifact produced by the algorithm. This issue cannot be directly addressed, because of the lack of visual or morphological landmarks. However, it can be noticed that the non-straight path obtained between frames 45-80 and 80-100 of P1, approximately, corresponds to the portion of the vessel where the stent has been implanted (red region in Figure 4.10(first column)), hence it is presumable that the *non-linear* behavior is actually induced by stent deployment.

Moreover, in order to assess if the *non-linearity* in Data-set B is excessive or lies in an acceptable range, the amount of *non-linearity* in both Data-sets A and B (NL_A and NL_B, respectively) can be assessed. To do so, the reference amount of *non-linearity* (NL_A) is estimated as the average distance between the *linear* fitting and the ground-truth landmarks. Since in Data-set B the number of manual annotations is too low, NL_B is computed as the average distance between the *linear* fitting and the *DTW-EPS-RC warping path*. The amount of *non-linearity* is estimated as $NL_A = 1.79 \pm 1$ gated frames and $NL_B = 2.4 \pm 1$ gated frames. As expected, in Data-set B the *non-linearity* of the *warping path* is slightly (but not excessively) higher than the reference measurement NL_A, since the vessel dilations and the stent deployment have a higher impact on the catheter path. However, it is interesting to note that NL_A is non-negligible, demonstrating that a *non-linear* alignment is necessary for pullback alignment.

4.5 Tool for Results Visualization

An interface has been developed for displaying the automatic results of the method, similarly to the interface that facilitates the manual labeling of pairs of corresponding

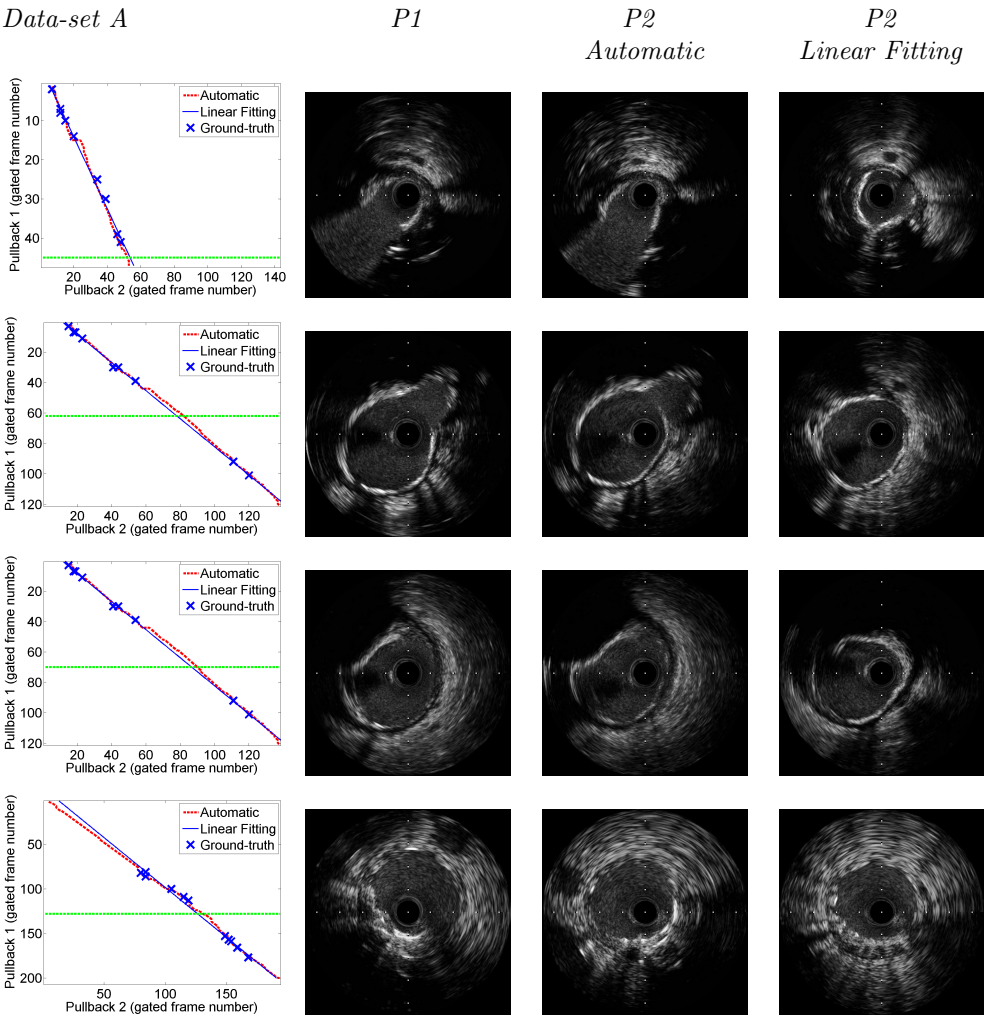

Figure 4.11: Examples of frame-to-frame correspondences in Data-set A. A matrix reporting the ground-truth, the automatic *warping path* and the *linear* alignment (first column), a frame on P1 (second column), the corresponding frames on P2 identified by automatic alignment (third column) and by *linear* fitting (fourth column) are shown.

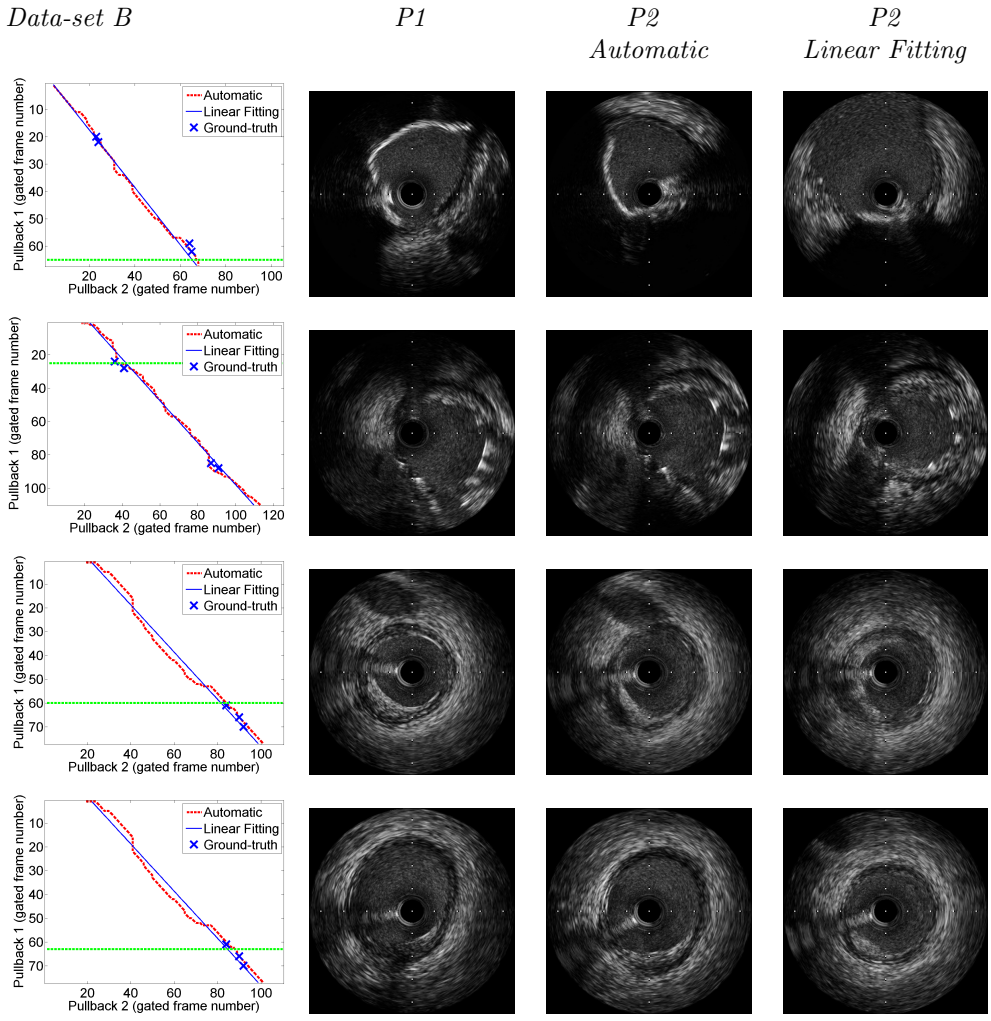

Figure 4.12: Examples of frame-to-frame correspondences in Data-set B. A matrix reporting the ground-truth, the automatic *warping path* and the *linear* alignment (first column), a frame on P1 (second column), the corresponding frames on P2 identified by automatic alignment (third column) and by *linear* fitting (fourth column) are shown.

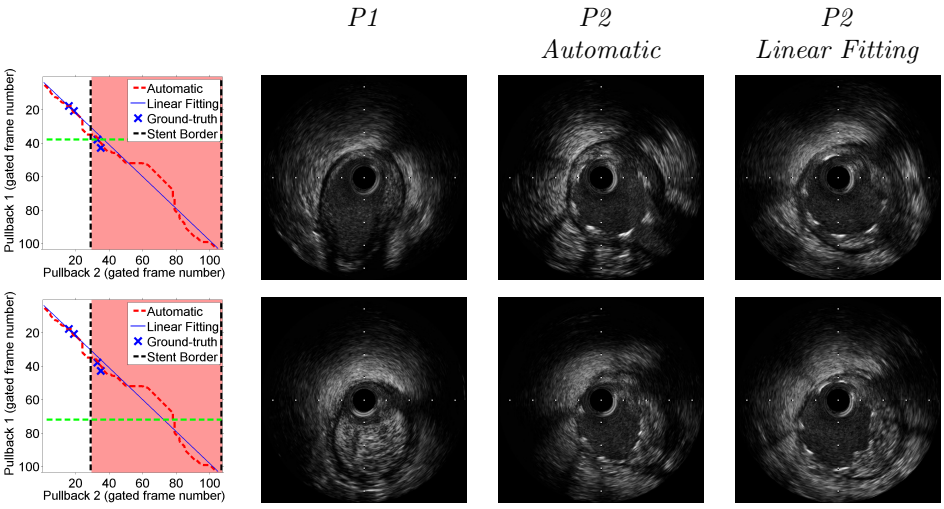

Figure 4.13: Frame-to-frame correspondences in a vessel segment pre/post stent deployment. A matrix reporting the ground-truth, the automatic *warping path*, the *linear* alignment and the extension of the stent segment (first column), a frame on P1 (second column), the corresponding frames on P2 identified by automatic alignment (third column) and by *linear* fitting (fourth column) are shown.

frames, which is described in Appendix B.

The proposed visualization tool allows physicians to easily inspect the correspondences identified by the automatic method. The interface shows, for both pullbacks, a *short-axis view* of the frames and two *longitudinal views* of the sequences, perpendicular to each other. The two pullbacks can be navigated manually by the user, in both longitudinal and angular directions. Moreover, the correspondences which have been automatically identified can be displayed in a sequential order, moving in both the proximal and the distal directions by using the buttons for the automatic *warping path* visualization. In Figure 4.14, the automatic alignment results are visualized through the interface.

4.6 Conclusions

In this chapter, a fully automatic framework for the temporal alignment of IVUS acquisitions of the same vessel is presented. This goal is reached by identifying a continuous non-rigid frame-to-frame correspondence between the two pullbacks. The IVUS sequences are described by means of multiple temporal profiles representing their morphological content. The DTW technique for non-rigid alignment is embedded into a multidimensional framework, specifically developed for addressing the challenges of IVUS alignment. The proposed solution includes two alternative robust strategies to handle the partial overlapping problem and a regularization term to

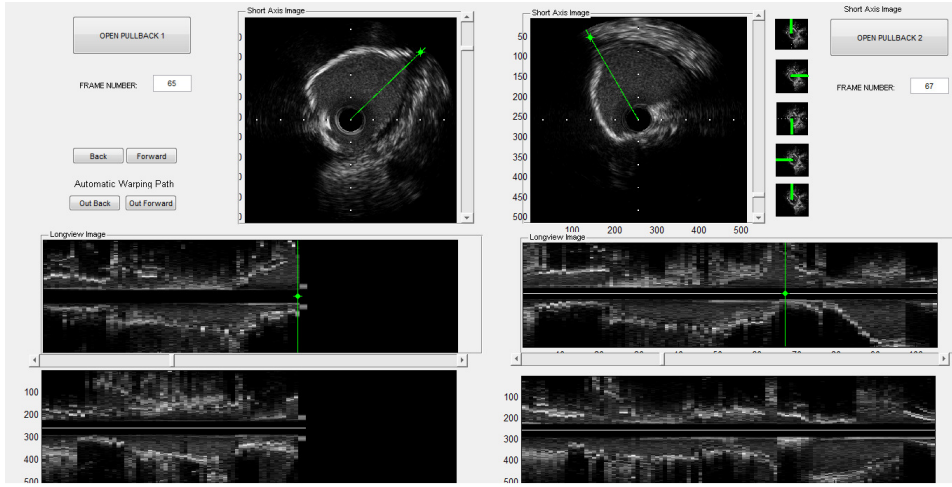

Figure 4.14: The interface for results visualization. Matching frames show the same calcification.

avoid a non-physiological temporal compression/expansion of the two sequences and to compensate for possible noise in the acquired signals.

An exhaustive validation is performed, both on synthetic data and on two *in-vivo* data-sets, one of which consists of multiple acquisitions of the same vessel without any morphological change, while the other contains pre/post intervention cases. The proposed approach reaches an average alignment error of approximately 0.43 and 0.77 mm on the two data-sets, respectively. Synthetic and *in-vivo* results show the robustness increase obtained by the proposed solutions with respect to the baseline DTW alignment. Qualitative *in-vivo* results illustrate the interest of the proposed *non-linear* alignment and show the clinical value of the method. An ad-hoc interface facilitates the visualization of the automatic results by physicians.

The alignment framework is robust to morphological changes induced by stent deployment and post dilation and is invariant to rotations of the probe and to the catheter or imaging system employed.

Moreover, given the extracted morphological profiles, the average computational time is less than 0.2 seconds per sequence pair, making the application suitable for intra-operative procedures. The method has been implemented in MATLAB and it has been executed on a PC equipped with an Intel Core 2 Duo 2.13 GHz processor and 4 GB RAM. It is worth noticing that, when fully automatic segmentation methods are employed, the morphological signals can be extracted in a first moment (in an offline segmentation), for instance after acquiring an IVUS sequence, while the proposed method for sequence alignment can be run in almost real-time, for instance when comparing two IVUS pullbacks.

Chapter 5

Automatic 2-D+T Lumen Border Extraction in IVUS Sequences

5.1 Introduction

The lumen is the interior part of the vessel, containing the blood. The luminal border or *tunica intima* is the innermost layer of the vessel and it is in direct contact with the blood flow. The *intima* is composed of simple squamous epithelial cells, that form a flat slick surface inside the vessel, minimizing the friction as the blood moves through the lumen.

The extraction of the lumen boundary from IVUS sequences is important for assessing the lumen size and consequently the severity of the atherosclerotic disease. In particular, detecting the lumen border allows to derive measurements such as the minimum and maximum lumen diameter and the luminal area stenosis (a measure of luminal compromise relative to a reference lumen, analogous to the angiographic diameter stenosis). For this reason, the segmentation of the luminal border in IVUS frames is crucial. Due to the high number of images in IVUS sequences (typically thousands of frames), manual annotation is extremely time-consuming. An automated analysis can reduce the time for manual interaction and at the same time can limit the subjectivity of the measurements, which is due to different interpretations by different physicians. Figure 5.1 illustrates an example of lumen segmentation in the cartesian and polar representation of an IVUS frame.

Several automatic methods for segmentation of the arterial lumen from IVUS images have been proposed since the early 1990s. In this chapter, we limit the bibliography to the most recent contributions. Most of the proposed approaches are based on active contour models (snakes). In [115, 121, 106], pixel intensity and gradient information (edges) combined with computational methods, including graph search, are used. In [57, 55, 85], the authors propose solutions based on active surfaces, active contours and neural networks. Downe *et al.* [32] presented a method based on active

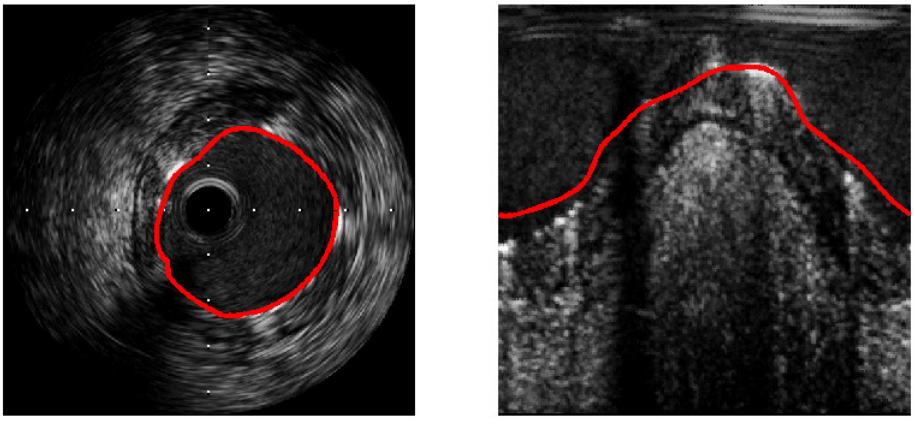

(a) (b)

Figure 5.1: IVUS image in (a) cartesian (x, y) and (b) polar (ρ, θ) domains. The luminal border is shown by a red line.

contour models, which provides an initial segmentation for a 3-D graph search, while Principal Component Analysis (PCA) is used for image pre-processing.

Ad-hoc solutions, statistical and probabilistic models which include *a-priori* knowledge about the vessel geometry have also been considered. In [16, 13] the gray level probability density function of the vessel structures, following Rayleigh distribution, is used.

Cardinal *et al.* [16] proposed a 3-D segmentation model based on the fast-marching method, which uses gray level probability density functions (PDFs) of the vessel structures, including the lumen. The gray level distribution of the whole IVUS pullback is modeled with a mixture of Rayleigh PDFs. With a multiple interface fast-marching segmentation, the lumen, intima plus plaque structure and media layers of the vessel wall are computed simultaneously. The fronts are initialized from manually traced lumen and media borders, and then they propagate with different speeds proportional to each PDF. Successively, Wennogle *et al.* [116] presented some improvements with respect to the method in [16], consisting in a pre-processing step to remove motion artifacts, a new directional gradient velocity term and a post-processing method based on level-sets.

In Taki *et al.* [108], the IVUS images are de-speckled by an anisotropic diffusion filter. Then, the initial locations of the borders are roughly estimated using ordinary edge detection methods. The final borders are successively identified using both geometric and parametric deformable models.

Methods based on discrete wavelet decomposition have also been proposed. Papadogiorgaki *et al.* [84] used wavelet analysis to generate texture information which,

combined with intensity information, initializes the contour. Similarly, Katouzian *et al.* [51] presented a method where texture information is obtained by wavelet analysis. A multiscale expansion approach uses wavelet packet analysis to differentiate between blood and non-blood regions of the IVUS images. The multi-channel texture segmentation algorithm based on discrete wavelet packet frames (DWPF) is used. A k-means clustering algorithm is employed to partition the extracted textural features into blood and non-blood regions, in an unsupervised fashion. Finally, the geometric and statistical information of the segmented regions is used to estimate the closest set of pixels to the lumen border and a spline curve is fitted to the set.

Another approach based on a learning process was presented in Rotger *et al.* [93], where the lumen detection is achieved by means of the classification of blood areas in a supervised learning fashion, by using AdaBoost. O'Malley *et al.* [83] presented a 3-D supervised classification approach (one-class SVM) for blood detection using spatial, temporal and spectral features, extracted on 3-D windows of fixed size. Mendizabal *et al.* [66] presented a semi-automated approach using a parametrization of the lumen with a mixture of Gaussians PDFs. The sum of such Gaussian functions is deformed by the minimization of a cost function formulated using a probabilistic approach. An optimization method is developed that linearly combines the descent directions of the steepest descent technique and the Broyden-Fletcher-Goldfarb-Shanno optimization method within a trust region that improves convergence. Successively, the same group presented a robust approach based on the RF signal processing [65].

Unal *et al.* [111] presented an automated shape-driven approach for the segmentation of the arterial wall from 2-D IVUS images in the polar domain. In a statistical shape space, properly built through PCA by using training data, the lumen contours are constrained to a smooth, closed geometry. In addition to a shape prior, an intensity prior is used through a non-parametric probabilistic energy function, with global image measurements. A detection step is included to address the challenges introduced by side branches and calcifications.

A different strategy is explored in [59, 6], where the following phenomenon is exploited: in successive frames of the IVUS sequence, the texture in the lumen region exhibits a large variability of the speckle pattern, due to the blood flow, while the speckle pattern changes slowly in the tissue area. Based on this observation, Kudo *et al.* [59] introduced a model-based approach, exploiting the de-correlation generated by the blood flow. The feasibility of this approach is illustrated by an *in-vitro* experiment, using an acrylic tube phantom, but not *in-vivo*. Balocco *et al.* [6] presented an extension of this approach along with validation on *in-vivo* cases. This method combines model-based temporal information extracted from successive frames of the sequence with spatial classification using the Growcut algorithm. Spatio-temporal information provides discriminative features for blood speckle.

In other approaches, segmentation is accomplished by the use of global region information including texture features [70, 86], gray level variances to model ultrasound speckle [43, 62], contrast of regions [125]. Finally, Zhua *et al.* [127] recently proposed an approach where a linear-filtered gradient vector flow drives the deformation of a balloon snake, while Sun *et al.* [107] presented a two-step method which first detects

the contours of interest on a number of *L*-mode cuts of the sequence and then evolves contours on the B-mode images until they reach the target points given by the first step.

Despite the relevant contributions in the literature, lumen segmentation is still an open problem in IVUS [50]. In particular, there is the need of a robust method able to perform well also with the most challenging data. With this motivation, in this chapter we propose a novel approach for lumen detection based on *supervised learning*. The recently proposed MSSL method [38] is applied and adapted to the specific clinical problem. Moreover, the difference in the temporal correlation of blood and tissue is exploited, as in [6]. The method presented in this chapter is fully automatic and does not require any initialization.

The approach is based on MSSL, consisting in a two-level stacked classification scheme, used for distinguishing between lumen and non-lumen regions of the IVUS frames. The lumen detection methodology takes into account the 2-D+T context of the IVUS sequences in a two-fold way: (1) by using the cross-correlation between successive frames of a sequence, as a feature for the binary lumen vs. non-lumen classification and (2) by exploiting the spatial and temporal neighborhood relation among the pixels, using the MSSL algorithm as a meta-classification technique. After the classification stage, the luminal border is identified by applying an active contour model to the output classification map.

The method has been validated on a large and challenging data-set, composed of sequences from 7 different patients, all characterized by the presence of deployed stent. Quantitative and qualitative results show the behavior of the framework in different clinical cases. Moreover, the algorithm has been tested on the data-sets provided during the "Lumen + External Elastic Laminae (Vessel Inner and Outer Wall) Border Detection in IVUS Challenge" associated with the MICCAI 2011 workshop on Computing and Visualization for (Intra)Vascular Imaging (CVII). The participation to the challenge was aimed at obtaining a quantitative comparison with *state-of-the-art* methods on lumen segmentation in IVUS. Such analysis is still pending, since the results of the challenge have not been disclosed yet. Meanwhile, a qualitative comparison with the *state-of-the-art* is provided in this chapter.

5.2 Method for Lumen Border Detection

The proposed framework for lumen border detection is divided into two main sequential stages. A binary classification problem is defined, aimed at distinguishing between lumen and non-lumen regions of the IVUS images. The binary classification task is addressed by means of a two-level stacked classification scheme. Then, the luminal border is identified by applying an active contour model to the obtained binary classification map.

5.2.1 Classification

The approach relies on a *pattern recognition* technique, in which a binary classifier is firstly trained on a data-set of IVUS images, previously labeled by physicians (training phase). Then it is used to identify lumen and non-lumen regions in new images (test phase). The *ground-truth* consists in a reliable data-set of labeled samples (lumen vs. non-lumen pixels of the IVUS images). Numeric information describing each pixel of the frames is computed by *feature extraction*.

In this study, a *discriminative* classification method (i.e., a classification method which aims to maximize the quality of the output on a given training set) is applied, in order to avoid the need to formulate hypotheses on the feature space. The AdaBoost algorithm [35] with decision stumps is used as the base classifier, in the context of the two-level stacked classification scheme (applied as a meta-classification technique). Apart from the classification labels, an additional output provided by AdaBoost is the classification margin $mar \in [-\infty, +\infty]$, representing, in the feature space, the distance from a sample to the decision boundary.

Feature Extraction The cartesian IVUS image $I(x, y)$ is first converted into polar coordinates:

$$\widetilde{I}(\rho, \theta) = I(\rho \cdot \cos\theta, \rho \cdot \sin\theta), \tag{5.1}$$

where x and y are the horizontal and vertical coordinates in the cartesian system, ρ and θ are the radial and angular coordinates in the polar system.

The description of blood and tissue properties is obtained by extracting a set of textural features, obtained from previous studies on borders segmentation and tissue characterization in IVUS [21, 22, 20, 6]. The following features are extracted from the polar image:

- Gabor filters [10] can extract the textural properties of the image according to a particular filter orientation. A set of 4 configurations of Gabor filters, which have demonstrated their ability to characterize the tissue in IVUS images [21], are used.
- *External accumulation* (A_e) [20] can be related the cumulative gray level of the polar image, and therefore to the blood accumulation, in the range $[\rho\ \rho_{MAX}]$, where ρ_{MAX} is the maximum value of the radial coordinate in the image:

$$A_e(\rho, \theta) = \rho \frac{\sum_{m=\rho}^{\rho_{MAX}} \widetilde{I}(\rho, \theta)}{\rho_{MAX} - \rho}. \tag{5.2}$$

- *Internal accumulation* (A_i) [20] gives information about the amount of blood accumulated in the range $[1\ \rho]$:

$$A_i(\rho, \theta) = \frac{\sum_{m=1}^{\rho} \widetilde{I}(\rho, \theta)}{\rho}. \tag{5.3}$$

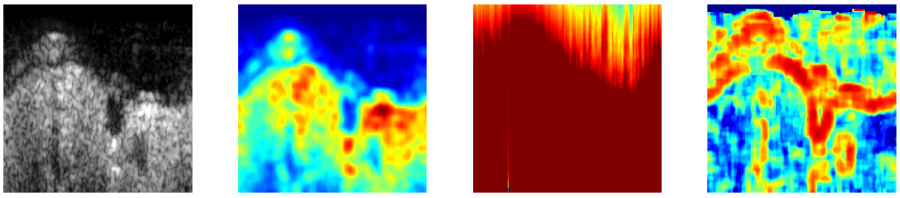

(a) (b) (c) (d)

Figure 5.2: Examples of features used for the lumen vs. non-lumen classification: (a) original image and maps obtained by using (b) Gabor filter, (c) *external accumulation*, (d) cross-correlation.

- Cross-correlation between the considered frame and the previous and successive frames of the sequence is used to exploit the low correlation expected in the blood region with respect to the tissue, due to the flow motion [59, 60, 6].
- The gray level value in the original IVUS image is used as a feature as well.

As a result, for each pixel of the polar image, a feature vector $\mathbf{x} \in \mathbb{R}^8$ is obtained.

MSSL In this chapter, the MSSL scheme [38] is applied, as a way of capturing and exploiting spatial and temporal sequential label relationships, extended over multiple scales. Details on the methodology presented in [38] and on its application to the lumen detection task are reported in this section. The generic MSSL method has been described in Chapter 2.

In the first stage of the MSSL algorithm, classification is based on the assumption that each pixel of the IVUS images is independent of the others. The continuity of the luminal region in IVUS sequences can be additionally taken into account to enhance the classifier capabilities. For this reason, the spatial and temporal neighborhood relation among the pixels of IVUS sequences is exploited in a second stage of classification. The second classification stage makes use of the feature set used in the first classification stage $\mathbf{x}(\rho, \theta)$ and of the classification margin provided as an output by the first classifier, $mar(\rho, \theta)$. For each image, the classification margin values are converted into an estimate of the likelihood that a sample belongs to the lumen class and organized in a *pseudo-probability map*, $p_l(\rho, \theta) \in [0, 1]$. In the MSSL scheme, the *pseudo-probability map* is represented according to a multi-scale (multi-resolution) decomposition. In the original formulation [38], the MSSL algorithm is bi-dimensional. Given $p_l(\overrightarrow{q})$ the likelihood at position $\overrightarrow{q} = (\rho, \theta)$, the multi-resolution decomposition Φ is defined as follows:

$$\Phi(\overrightarrow{q}, s) = p_l(\overrightarrow{q}) * G\left(0, \gamma^{s-1}\right), \tag{5.4}$$

where $s \in \{1, 2, \ldots, S\}$ represents the scale, G is a bi-dimensional Gaussian with zero mean and $\sigma = \gamma^s$ and γ is the "step" of the decomposition. The multi-resolution

decomposition is then sampled following a grid, with regular sampling step, consisting of a set of $N_{displ} = s^2_{sampling}$ displacements. As a result, an additional set of features $\mathbf{z}$ is obtained, of length $S \times N_{displ}$. Wrap-around issues in the polar IVUS image are handled by using a circular padding in the horizontal (angular) dimension and by setting the values of the extended set outside the map in the vertical (radial) dimension to 1 (lumen) on the top and 0 (non-lumen) on the bottom. An extended feature set is created, $\mathbf{x}^{\mathbf{est}} = [\mathbf{x}, \mathbf{z}]$, by joining the original feature set to the additional features from the sampling. Finally, the extended set is analyzed by a second classifier and classification labels are produced.

The two classifiers are trained separately and after training they can be applied to new images inside the same scheme. In both MSSL stages, the AdaBoost algorithm with decision stumps is used as a base classifier.

In Figure 5.3, the binary classification output at the first (b) and second (c) stages of sequential learning is shown for a sample frame, together with the corresponding *pseudo-probability maps* (e), (f).

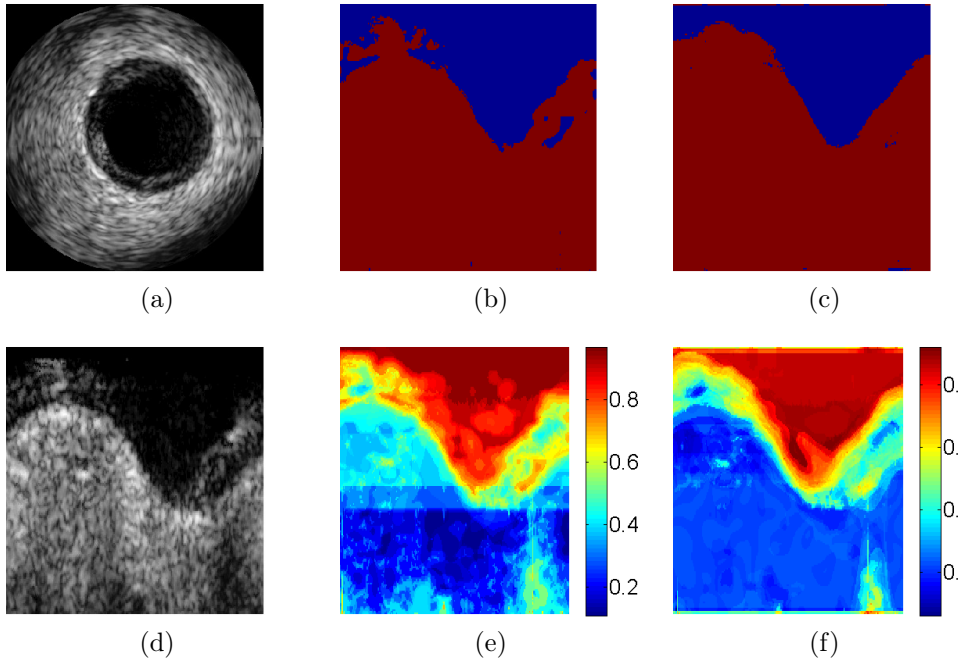

Figure 5.3: A frame in (a) cartesian and (d) polar representations; classification maps, after (b) the first and (c) the second classification stages of the MSSL scheme, where the luminal region is represented in blue; (e) and (f) *pseudo-probability maps* corresponding to the two stages, respectively.

2-D+T MSSL The originally bi-dimensional MSSL approach is extended in this study to three dimensions: the radial, angular and temporal (longitudinal) dimensions of the pullback. This latter is introduced to exploit the temporal coherence of successive frames. Only the gated frames, belonging to the same phase of the cardiac cycle, are considered along the longitudinal dimension. Such frames are selected from the IVUS sequence by applying the image-based gating technique proposed in [37], as described in Chapter 2.

Three-dimensional positions in the IVUS sequence, $\overrightarrow{q} = (\rho, \theta, t)$, are considered, where t is the temporal coordinate. The *pseudo-probability* values of a 2-D+T volume in the three dimensions are analyzed when computing the decomposition and the sampling for the pixels of each image. The multi-resolution decomposition uses a three-dimensional Gaussian kernel. The sampling is performed in the three dimensions, therefore the number of displacements is $N_{disp} = s^3_{sampling}$. In the longitudinal dimension, wrap-around issues are tackled by setting the values of the extended set outside the map equal to those of the corresponding pixels in the most external frames of the sequence. Figure 5.4 shows an example of multi-resolution decomposition for the pixels of a given frame of the sequence (represented in the second column), at three different scales reported in the three rows.

5.2.2 Active Contour Model

An active contour model (snake) is applied to the binary classification map. Snakes [49] (introduced in Chapter 2) are energy-minimizing splines, guided by internal constraint forces and influenced by external forces, used in image segmentation tasks. Given a parametric curve describing the luminal border, $C(v) = (\rho(v), \theta(v))$, representing the snake having arc length v, the energy function to be minimized is given by the following term:

$$E_{acm} = \int_0^1 E_{int}(C(v)) + E_{ext}(C(v))dv. \tag{5.5}$$

Following the traditional formulation [49], E_{int} is the internal energy of the snake due to bending :

$$E_{int} = \alpha \left(\frac{\partial C(v)}{\partial v} \right)^2 + \beta \left(\frac{\partial^2 C(v)}{\partial v^2} \right)^2. \tag{5.6}$$

The first-order term $\left(\frac{\partial C(v)}{\partial v}\right)^2$ represents the energy of the contour and makes the snake act like a membrane, while the second-order term $\left(\frac{\partial^2 C(v)}{\partial v^2}\right)^2$ represents the energy of the curvature and makes the snake act like a thin plate [49]. Large values of α will increase the internal energy of the snake as it stretches more, whereas small values of α will make the energy function insensitive to the amount of stretch.

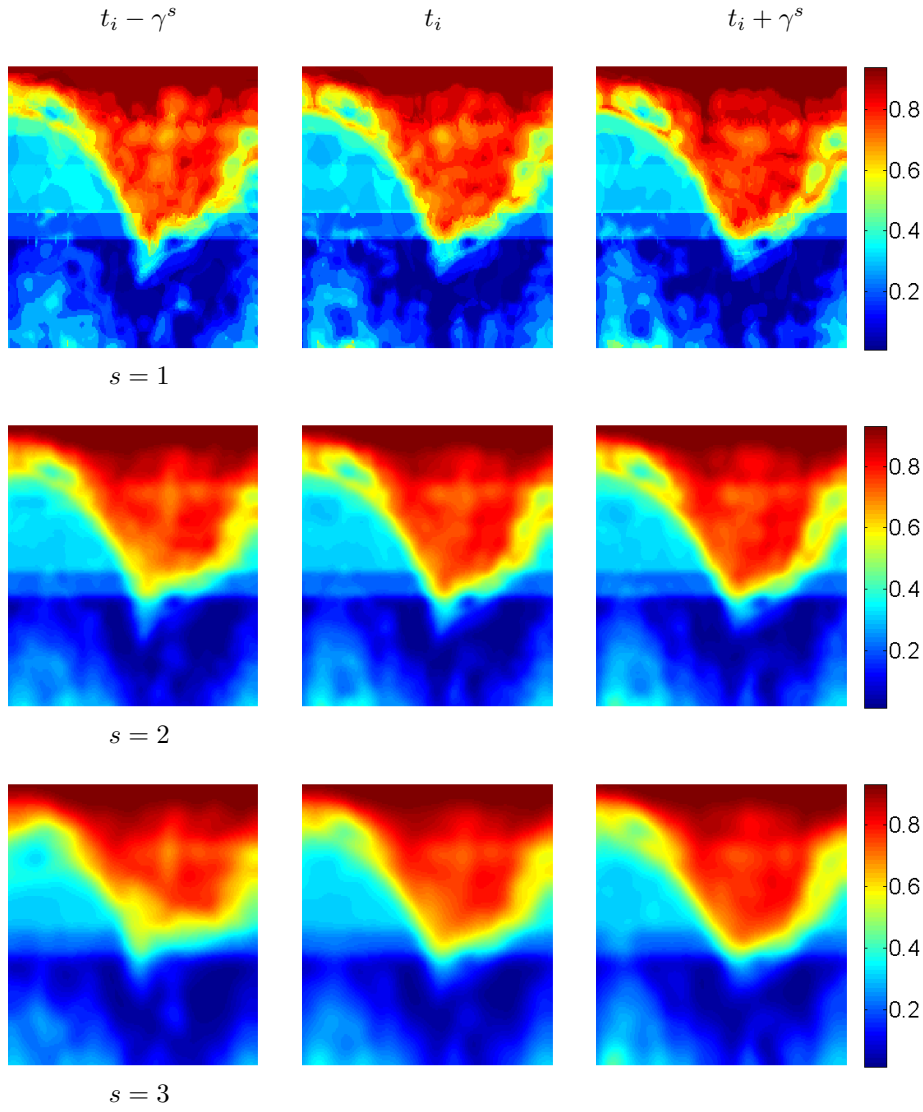

Figure 5.4: 2-D+T Multi-scale decomposition at three different scales: $s = 1$ (first row), $s = 2$ (second row), $s = 3$ (third row). Given the analyzed frame at position t_i in the sequence (second column), the previous and successive frames of the sequence at distance γ^s will be sampled (first and third columns, respectively).

Similarly, large values of β will increase the internal energy of the snake as it develops more curves, whereas small values of β will make the energy function insensitive to curves in the snake.

E_{ext} represents the external energy of the active contour model, which in this study is computed as:

$$E_{ext} = \frac{\partial(M_l(\rho,\theta)*G(0,\sigma_{acm}))}{\partial\rho}\Big|_{(l\to nl)} + \frac{\partial(M_l(\rho,\theta)*G(0,\sigma_{acm}))}{\partial\theta}\Big|_{(nl\to l)} + \\ + \frac{\partial(M_l(\rho,\theta)*G(0,\sigma_{acm}))}{\partial\theta}\Big|_{(l\to nl)}, \tag{5.7}$$

where $M_l(\rho,\theta)$ is the output classification map obtained in the previous stage, $G(0,\sigma_{acm})$ is a bi-dimensional Gaussian, $(l \to nl)$ and $(nl \to l)$ represent "lumen (l) to non-lumen (nl)" and "non-lumen to lumen" transitions, respectively. E_{ext} is computed as the first derivative of the classification map, previously blurred by Gaussian filtering, in both the vertical (radial) and the horizontal (angular) dimensions (see Figure 5.5(a)). Vertical derivatives of non-lumen to lumen transitions are discarded, since they do not represent lumen borders.

The fitting of a snake is repeated twice. In the first stage, a rough detection is achieved by initializing the snake horizontally, along the radius where the cumulative sum of the derivative image over all the angular positions reaches its maximum value, and by using a large window for Gaussian blurring (see Figure 5.3(b)). In the second stage, the first results are refined (see Figure 5.3(c),(e)); the snake is initialized in the final position reached in the previous stage and σ_{acm} is halved.

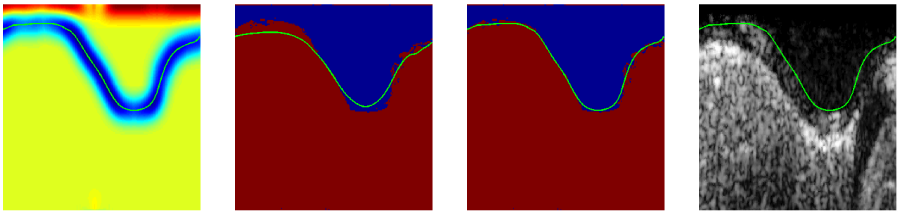

(a) (b) (c) (d)

Figure 5.5: (a) The map used as the external energy E_{ext} of the active contour model; (b) first results and (c) refinement of the luminal contour, superimposed to the classification map, where the luminal region is represented in blue; (d) refinement superimposed to the original IVUS image.

5.3 Experimental Results

The proposed approach for luminal border detection has been validated on a data-set provided by the Hospital "German Trias i Pujol" (Data-set A), consisting in 7

sequences from 7 different patients, acquired with an iLab IVUS Imaging System (Boston Scientific) using a 40 MHz catheter Atlantis SR 40 Pro (Boston Scientific). For each pullback, a vessel segment of 60 successive gated frames has been considered, for the validation of the proposed 2-D+T approach. Moreover, the method has been tested on two data-sets, provided in the "Lumen + External Elastic Laminae (Vessel Inner and Outer Wall) Border Detection in IVUS Challenge" associated with the MICCAI 2011 workshop on Computing and Visualization for (Intra)Vascular Imaging (CVII). The data-sets have been acquired with a Boston Scientific iLab IVUS Imaging System (Data-set B) and a Volcano Imaging System (Data-set C), respectively. The data-sets are described in detail in Appendix B.

5.3.1 Experiments on Data-set A

Data-set A is characterized by the presence of stent in all the sequences. Stent covers a significant portion of the pullbacks, for a total 221 stent frames over 420 frames. It is worth noticing that a challenging data-set has been created for this study, aimed at reflecting the clinical application of lumen border detection. In particular, detecting the lumen in stent frames is important to identify stent malapposition and stent under-expansion.

In this data-set, the lumen border has been labeled in the gated frames by a clinician. The performance is assessed by means of *Leave-One-Patient-Out* (LOPO) cross-validation technique over $N_P = 7$ folds, corresponding to the patients. For each fold, the training is performed on samples from all the other folds and the trained classifier is tested on the fold itself. The parameters of the MSSL algorithm have been set to the values: $S = 5$, $\gamma = 2$, $s_{sampling} = 3$, while the parameters of the active contour model have been set to the weights: $\alpha = 0,2$ and $\beta = 0,5$.

The first part of the method, i.e., the classification of lumen and non-lumen regions of the images, is validated by using classification performance measures, in terms of:

$$\begin{array}{rc} \text{Accuracy:} & A = \frac{TP+TN}{TP+TN+FP+FN} \\ \text{Sensitivity:} & S = \frac{TP}{TP+FN} \\ \text{Specificity:} & K = \frac{TN}{TN+FP} \\ \text{Precision:} & P = \frac{TP}{TP+FP} \\ \text{False Alarm Ratio:} & FAR = \frac{FP}{TP+FN} \end{array}$$

where TP = True Positive, TN = True Negative, FP = False Positive, and FN = False Negative.

Table 5.1 reports the overall performance ($MEAN \pm STD$) of the lumen vs. non-lumen classification. In order to demonstrate the advantage given by the use of contextual information, the results achieved by applying the MSSL scheme are compared to the results obtained by only using the first stage of the scheme, where each pixel of the sequence images is classified independently. As it can be observed in Table 5.1, the second MSSL step yields an overall performance improvement. The Wilcoxon test

proves that, with a significance level $\alpha = 0.1$, the performance in the second stage is significantly better than in the first stage in terms of accuracy, precision, specificity, false alarm ratio, and it is comparable in terms of sensitivity.

Table 5.1: Classification performance ($MEAN \pm STD$) on Data-set A, at the first and the second classification stages of the MSSL scheme.

	Stage 1	*Stage* 2
A (%)	92.49 ± 1.98	94.99 ± 1.55
S (%)	92.24 ± 5.01	90.42 ± 4.76
P (%)	81.73 ± 7.49	90.52 ± 6.25
K (%)	92.81 ± 2.06	96.62 ± 1.96
FAR (%)	21.66 ± 11.45	9.95 ± 7.07

The complete framework for luminal border detection, leading to the definition of the lumen border contour, is validated by using the following error measures:

- Jaccard Measure (JM), is the Jaccard measure computed over the two vessel areas defined by the automatic (R_{auto}) and the manual curve (R_{man}):

$$JM(R_{auto}, R_{man}) = \frac{|R_{auto} \bigcap R_{man}|}{|R_{auto} \bigcup R_{man}|}, \tag{5.8}$$

  where R_{man} and R_{auto} are the regions of the manually annotated contours C_{man} and of the automatic contours C_{auto}, respectively.

- Percentage of Area Difference (PAD), is the difference between the lumen areas for the automatic (A_{auto}) and manual (A_{man}) borders, expressed as a measure relative to the manual annotation:

$$PAD = \frac{|A_{auto} - A_{man}|}{A_{man}}. \tag{5.9}$$

- Hausdorff Distance (HD) between the automatic and the manual curve annotation, computed as follows:

$$HD(C_{auto}, C_{man}) = max_{a \epsilon C_{auto}} \left\{ max_{_{b \epsilon C_{man}}} \left[d\left(a, b\right) \right] \right\}, \tag{5.10}$$

  where a and b are points of the curves C_{auto} and C_{man}, respectively, and $d\left(a, b\right)$ is the euclidean distance.

- Mean radial distance (mrd), is the average absolute distance between the automatic and the manual curve, computed over all the radii in polar coordinates.

In Table 5.2, the performance of the framework is illustrated. The results on the whole data-set (considering all the frames) are reported in the second column. It is worth noticing that, in an IVUS pullback, not all the frames have the same segmentation complexity, since echographic reflexions, vascular bifurcations, artifacts due to

the guide-wire, stent, and plaque appearance may make the segmentation task more challenging. For this reason, the performance of the method can be evaluated by considering different image categories. Table 5.2 additionally reports the results of the algorithm by grouping the frames according to their morphological and clinical condition, in the 3rd to 6th columns. The following categories are considered: stent, bifurcation, calcified plaque, and catheter touching the lumen (i.e., "eccentric" lumen). The presence of the asterisk in the third to sixth columns of Table 5.2 denotes a statistically significant difference between the performance on these categories and the same measures computed on all the frames, by applying the Wilcoxon test with significance level $\alpha = 0.1$. It can be observed that the method is robust to presence of deployed stent, with results comparable to those on the whole data-set. In presence of calcifications and eccentric lumen, the performance is comparable for most of the parameters, while the results are significantly worse in bifurcation frames.

Table 5.2: Performance of lumen border detection ($MEAN \pm STD$) on Data-set A. The columns represent the following cases: all the frames, stent, bifurcation, calcification, and eccentric lumen (i.e., catheter close to the luminal border).

	all	$stent$	$bifurcation$	$calcium$	$eccentric$
JM (%)	81.08 ± 11.93	81.64 ± 12.57	$75.08 \pm 15.76*$	$79.67 \pm 10.43*$	$78.03 \pm 14.03*$
HD (mm)	0.31 ± 0.28	0.33 ± 0.31	$0.51 \pm 0.4*$	0.27 ± 0.17	0.36 ± 0.36
PAD (%)	13.93 ± 12.52	13.91 ± 10.76	$18.55 \pm 12.93*$	15.90 ± 14.40	13.77 ± 12.33
mrd (mm)	0.15 ± 0.1	0.16 ± 0.12	$0.22 \pm 0.15*$	0.14 ± 0.08	0.16 ± 0.12

A further analysis is performed on the scores obtained on the whole data-set. We consider a certain value for each of the performance parameters, and compute in how many frames, as a percentage of the data-set, the selected requirement is fulfilled. The characteristic profiles are depicted in Figure 5.6, where the performance measures are represented on the horizontal axis and they vary from the value 0 to the maximum value, obtained when 100% of frames are considered. For example, an mrd measure ≤ 0.3 mm is obtained in 91% of the frames (see Figure 5.6-d).

In Figure 5.7, qualitative results of lumen detection are illustrated. As it can be observed, the proposed method performs well in case of stent deployment (Figure 5.7(d-f)). In bifurcation frames, the tendency of the method is to identify a smaller contour than the ground-truth, i.e., to delineate only the lumen of the main vessel, without segmenting the side-branch vessel (Figure 5.7(g-h)). It can be noticed that, in our data-set, the manual annotation in bifurcation frames always includes the side-branch lumen into the segmented lumen, but this interpretation is subjective. The method is robust to the guidewire artifacts (Figure 5.7(i)), although few errors can be noticed (Figure 5.7(l)). Errors can be observed in case of large vessels (Figure 5.7(m)), or when a vein close to the inspected artery resembles the appearance of a bifurcation (Figure 5.7(n)).

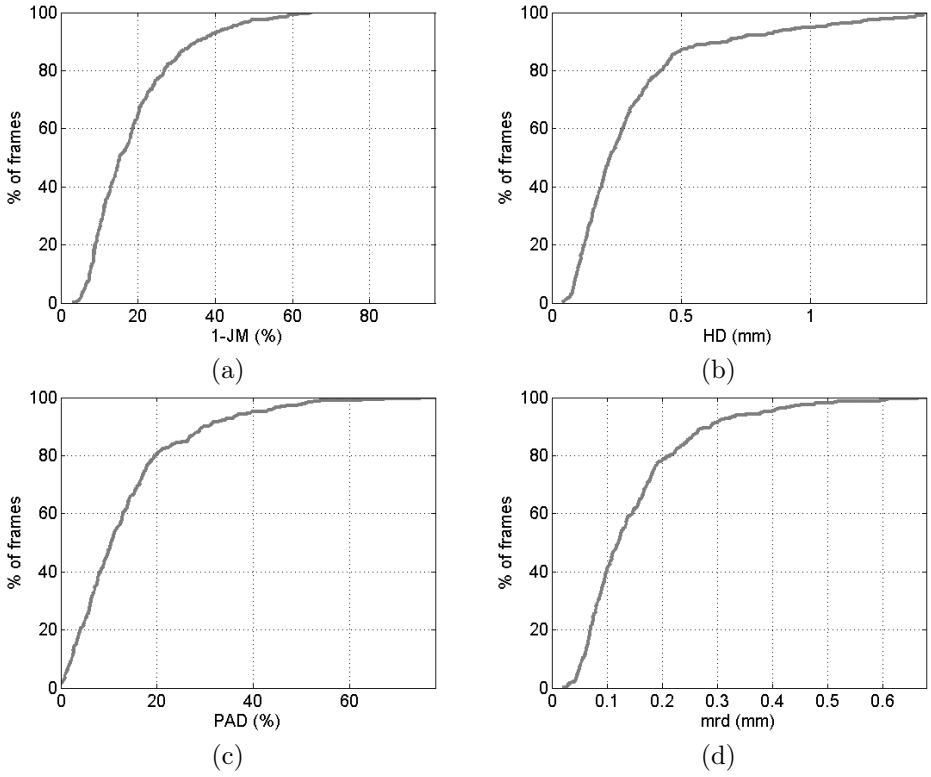

Figure 5.6: Performance of the proposed methodology with respect to the JM, HD, PAD, and mrd measures. Profiles detailing the number of frames (y-axis) that fulfill the performance measures (a) (1-JM), (b) HD, (c) PAD, and (d) mrd (x-axis) are shown for the automatic detection.

5.3.2 Experiments on Challenge Data-sets

In the MICCAI Challenge, the MSSL approach has been applied in 2-D+T only on Data-set C (Volcano images), where consecutive gated frames have been provided, while in Data-set B (iLab images) the technique has been applied only in the radial and angular dimensions. Both data-sets have been divided into a training set, representing 25% of the data, and a test set, representing 75% of the data, as required for the Challenge. The binary classifier has been trained separately for each data-set, by using a *ground-truth* for the luminal border labeled by physicians, which defines lumen and non-lumen regions of the images.

Since a journal article describing the results of the MICCAI Challenge is currently under review, the results could not be reported in this thesis. The test results of all participants, the different sets of lumen contour labels annotated by different physicians, and the inter- and intra-observer variability have not been disclosed yet. For this reason, in this chapter the algorithm performance is only briefly described

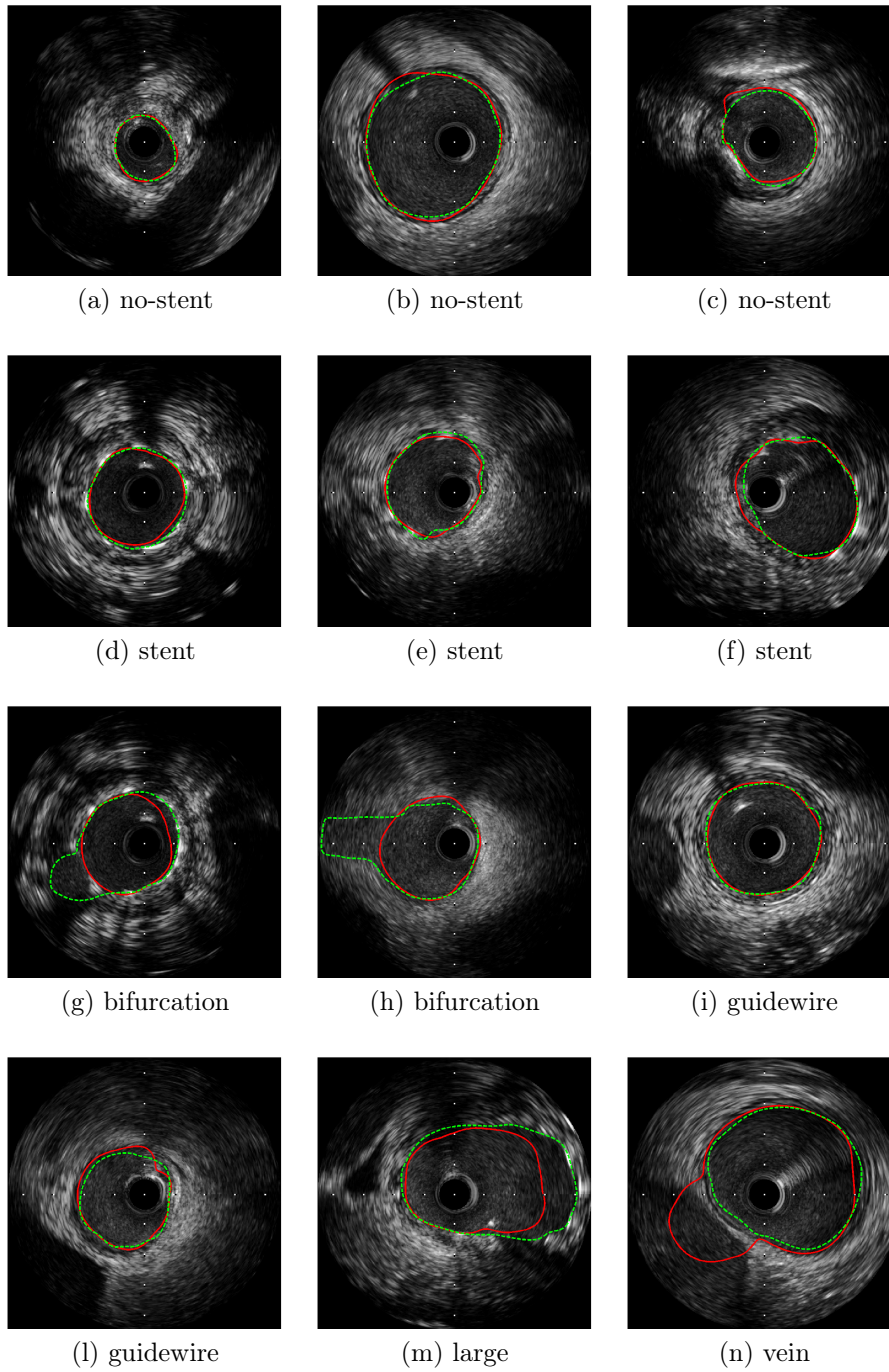

(a) no-stent (b) no-stent (c) no-stent

(d) stent (e) stent (f) stent

(g) bifurcation (h) bifurcation (i) guidewire

(l) guidewire (m) large (n) vein

Figure 5.7: Segmented images from Data-set C. The automatic and manual contours are depicted with a continuous and dotted line, respectively. Frames belong to the following categories: (a-c) no-stent, (d-f) stent, (g-h) bifurcation, (i-l) guidewire artifact, (m) large vessel, (n) vein close to the inspected artery.

from a qualitative point of view.

The overall performance is better in Data-set C than in Data-set B. This can be due to different factors. First, the penetration is higher for the 20 MHz images of Data-set C: the 20 MHz transducer allows higher tissue penetration while losing details, but also artifacts, in the image formation. Instead, the 40 MHz probe produces more speckle noise. The guide-wire effect is not present in Volcano data. Moreover, Data-set B is more challenging from the clinical point of view. Finally, the method is applied in 2-D+T only in Data-set C, where successive gated frames are available. The proposed approach provides acceptable segmentation of the lumen contour in frames belonging to both data-sets. The method is robust and particularly suited for challenging clinical cases. Robustness to artifacts, such as the guide-wire artifact in Data-set B, is high. In case of errors, the general tendency of the automatic method is to provide a smaller contour than the actual luminal border. This is particularly evident in the presence of bifurcations.

5.3.3 Comparison with *State-of-the-Art*

Finally, a qualitative comparison with *state-of-the-art* methods on lumen segmentation is presented, by considering for our method the validation performed on Data-set A. Several of the most recent methods described in the first section of the chapter have been chosen, by selecting the techniques that are representative of different families of approaches. Following, the specifications and results of the different methods are reported: the IVUS technology (20/40 MHz catheter), the level of automation, the advantages, the limitations, the validation data-sets, the performance. The comparison is summarized in Table 5.3.

The semi-automated method proposed in Cardinal *et al.* [16] is applied to 9 *in-vivo* IVUS pullbacks and to a simulated IVUS pullback. On *in-vivo* IVUS, the average distance between segmentation results and manually traced contours is less than 0.16 mm, while the HD is less than 0.4 mm.

Mendizabal *et al.* [66] presented a semi-automated approach which is evaluated on a set of 100 IVUS images acquired with a 20 MHz catheter. The average accuracy is 98.28%±0.49%, the average true negative rate is 99.43%±0.29%, and the average true positive rate is 95.57%±1.69%. The authors remark that on higher-frequency IVUS images (i.e., 30-40 MHz) the speckle noise will be higher, making it difficult to use this method, since it employs only gray level histograms to compute the likelihoods.

In Taki *et al.* [108], a 20 MHz technology is used. The automated method is tested on 7 cases totaling 60 IVUS images and it reaches an absolute difference of the areas of 6.26 ± 1.72 mm^2, a HD of 0.7 ± 0.25 mm and an average distance of 0.2 ± 0.15 mm, by using the (better performing) geometric deformable model.

In Unal *et al.* [111] an automated approach segments the arterial wall from 2-D IVUS images in the polar domain. By testing the method on 20 MHz images, the mean distance statistics is 0.08 ± 0.10 mm and the maximum distance is 0.44 ± 0.76 mm in an easier data-set, which excludes large calcifications and side-branch openings,

while, in a more challenging data-set, the two statistics become 0.09 ± 0.12 mm and 0.65 ± 1.27 mm, respectively.

The fully automatic method proposed in Katouzian *et al.* [51] is tested on 40 MHz images. The data-set consists of three *in-vivo* cases and two cadaver cases. The results show that manual and automated luminal borders are well correlated ($r = 0.9854$).

O'Malley *et al.* [83] presented a 3-D supervised classification approach (one-class SVM) for blood detection. Three cases, acquired *in-vivo* in swine with a 40 MHz catheter, are used for training and testing, each case consisting of 30 frames. Statistics related to the classification accuracy (sensitivity S and specificity K) are reported: (1) $S = 97\%$ and $K = 82.3\%$ and (2) $S = 95.4\%$ and $K = 100\%$, for two cases.

Balocco *et al.* [6] presented an automated method. Performance is evaluated on 300 *in-vivo* frames acquired from three sequences with a 40 MHz catheter. The average segmentation error in alll the frames, stent frames and bifurcation frames is 0.17 ± 0.08 mm, 0.18 ± 0.07 mm and 0.31 ± 0.12 mm, respectively.

When comparing our method to the *state-of-the-art*, it can be observed that the validation proposed in this chapter is among the most extensive, using 420 images from 7 patients (see Table 5.3, 5th column). Moreover, our data-set is particularly challenging due to the signicant presence of stent. The method is fully automatic, and validation is performed on the most challenging type of images, acquired with a 40 MHz catheter (see Table 5.3, 3rd column). It is important to note that the use of different types of catheters, the different level of automation, and the different performance measures limit the possibility of a direct quantitative comparison between our method and *state-of-the-art* methods, as discussed at the beginning of this chapter. However, it can be observed in Table 5.3 that the obtained Hausdorff distance is lower than in Cardinal *et al.* [16] and Taki *et al.* [108]. Moreover, the mean radial distance is lower than in Cardinal *et al.* [16], Taki *et al.* [108], and Balocco *et al.* [6], but higher than in Unal *et al.* [111].

5.4 Conclusions

In this chapter, the problem of lumen segmentation is addressed by means of a novel *pattern recognition* approach, which uses a two-level stacked classification algorithm. The methodology is extended in 2-D+T and takes advantage of the continuity of the luminal region in IVUS sequences to enhance the results. The method is fully automatic. The framework is independent of the acquisition system of the machine and has been tested on images from two different echographs. The results show robustness to different challenging clinical cases. The main limitation of this approach consists in the application of the active contour model in 2-D. The extension of this last step of the framework to the temporal dimension is pending, and it has been planned for the next months investigation.

The method has been implemented in MATLAB and it has been executed on a PC equipped with an Intel Core 2 Duo 2.13 GHz processor and 4 GB RAM. The average execution time for every frame is 8 seconds for feature extraction, 0.44 seconds for classification and 4.5 seconds for luminal border identification.

Table 5.3: List of *state-of-the-art* lumen segmentation algorithms, and their specifications and performance.

Authors [Ref.], Year	Implemented technique	Freq. (MHz)	Automation level	Data	Performance measures	Results
Proposed method	3-D, MSSL, deformable model	40	aut.	7 cases (420 images tot.)	A S P K FAR Jaccard Measure Hausdorff distance PAD mrd	$94.99\% \pm 1.55\%$ $90.42\% \pm 4.76\%$ $90.52\% \pm 6.25\%$ $96.62\% \pm 1.96\%$ $9.95\% \pm 7.07\%$ $81.08\% \pm 11.93\%$ 0.31 ± 0.28 mm $13.93\% \pm 12.52\%$ 0.15 ± 0.1 mm
Cardinal *et al.* [16], 2006	3-D, Rayleigh mixture PDFs, fast marching	20	semi-aut.	(a) 9 *in-vivo* cases, (b) 1 simulated case	average distance Hausdorff distance area difference	(a) / (b) 0.16 ± 0.1 mm / 0.072 ± 0.062 mm 0.4 ± 0.25 mm / 0.226 ± 0.074 mm 0.4 ± 2.1 mm^2
Mendizabal *et al.* [66], 2008	2-D, mixture of Gaussians PDFs, Bayesian cost function, novel minimization	20	semi-aut.	100 images	accuracy true negative rate true positive rate	98.28% 99.43% 95.57%
Taki *et al.* [108], 2008	2-D, statistical analysis, deformable model	30	aut.	7 cases (60 images tot.)	average distance Hausdorff distance absolute area diff.	0.2 ± 0.15 mm 0.7 ± 0.25 mm 6.26 ± 1.72 mm^2
Unal *et al.* [111], 2008	2-D, statistical shape model	20	aut.	(a) easy data-set, (b) challenging data-set	average distance maximum distance	(a) / (b) 0.08 ± 0.10 mm / 0.09 ± 0.12 mm 0.44 ± 0.76 mm / 0.65 ± 1.27 mm
Katouzian *et al.* [51] , 2008	2-D, Multiscale	40	aut.	3 *in-vivo* cases, 2 cadaver cases	correlation coefficient	0.9854
O'Malley *et al.* [83], 2007	3-D, one-class SVM	40	aut.	3 cases (30 frames each) from swine	sensitivity specificity	97% / 95.4% 82.3% / 100%
Balocco *et al.* [6], 2011	temporal correlation, Growcut algorithm	40	aut.	3 cases (300 images tot.): (a) all, (b) stent, (c) bifurcation	average distance maximum distance	(a) / (b) 0.17 ± 0.08 mm / 0.18 ± 0.07 mm 0.57 ± 0.24 mm / 0.62 ± 0.19 mm (c) 0.31 ± 0.12 mm 1.12 ± 0.44 mm

Chapter 6

Conclusions and Future Work

In this thesis, several methods for automated analysis of IVUS sequences are presented, aimed at assisting physicians in the treatment of coronary disease. The first section of this chapter summarizes each main chapter, by revisiting the contributions, strengths and weaknesses of the proposed methods. Then, a brief overview of the future research possibilities opened by this thesis in the area of IVUS analysis is presented.

6.1 Summary and Contributions

Chapter 1 introduces the medical context of this thesis and the IVUS technology. First, coronary disease and coronary interventional procedures are described. Then, the role of IVUS in the diagnosis, the planning and evaluation of the coronary intervention, and the patient monitoring is illustrated, along with the challenges in IVUS image analysis.

In Chapter 2, the background in IVUS is delineated. The taxonomy of the IVUS technology in medical imaging is defined according the thesis scope, by analyzing: (1) the image acquisition techniques, (2) the preprocessing methods that compensate for the dynamic artifacts due to catheter motion and heart beating, and (3) the approaches for automatic IVUS analysis, which include methods for segmenting lumen and media-adventitia borders and different plaque types, bifurcation detection approaches, and alignment/fusion of data acquired from coronary imaging modalities. A literature review in each of these topics is presented, along with our contributions to the *state-of-the-art*.

In Chapter 3, a novel approach for automatic bifurcation detection in IVUS is presented. The method identifies every bifurcation in an IVUS sequence, the corresponding frames, the angular orientation with respect to the IVUS acquisition, and the extension. This goal is reached using the multi scale stacked sequential learning

scheme, and the results are then refined using a-priori information about branching dimensions and geometry. The method is validated on *in-vivo* sequences and the performance is compared to inter- and intra-observer variability. Satisfactory results are obtained in most frames, while the performance slightly decreases when stent, vein, ostium and small bifurcation frames are analyzed. This study presents a new visualization map for IVUS sequences, summarizing the vessel characteristics in a compact representation. The proposed framework for automatic bifurcation detection is an accepted US patent, commonly signed with *Boston Scientific Corporation*.

In Chapter 4, we propose an automatic approach for IVUS alignment, based on the DTW technique. The non-rigid alignment algorithm is adapted to the specific IVUS alignment task by applying it to multidimensional temporal signals describing the morphological content of the vessel. DTW is embedded into an ad-hoc framework, comprising two alternative robust strategies to address partial overlapping between acquisitions. Extensive validation is performed on both synthetic and *in-vivo* data. The results show the robustness increase obtained by the proposed solution with respect to the baseline DTW alignment. Qualitative results illustrate the interest of the proposed *non-linear* alignment and show the clinical value of the method. An ad-hoc interface facilitates the visualization of the automatic results by physicians. The alignment framework is robust to morphological changes induced by stent deployment and post dilation, and it is invariant to rotations of the probe.

In Chapter 5, the problem of lumen segmentation in IVUS is addressed by proposing a novel pattern recognition approach. The classification of lumen and non-lumen regions of the images is performed by using the two-step multi scale stacked sequential learning algorithm. The methodology is extended in this study to three dimensions, including the longitudinal (temporal) dimension of the sequence. Therefore the method takes advantage of the continuity of the luminal region in IVUS sequences. The framework is fully automatic. The method is independent of the acquisition system of the machine. It has been validated on a challenging data-set, representitive of the range of conditions in the clinical practice, and it has been tested on images from two different echographs. The results show robustness to different challenging clinical cases.

6.2 Future Work

Throughout this thesis, various approaches to IVUS analysis are proposed. The contributions and limitations of each of these methods are opening future research lines:

Automatic Bifurcation Detection The bifurcation detection framework could be extended to additionally provide a *characterization* of the identified bifurcations. In particular, a future research direction could involve the automatic identification of the *optimal longitudinal view* for each bifurcation in an IVUS sequence, i.e., the optimal longitudinal cut from which the *angle of incidence* (the angle between the main vessel and the side-branch) is visible. Moreover, information about the *angle of incidence*

could be automatically provided, for instance by defining several discrete classes for the amplitude of the angle, and then assigning each bifurcation to one of these classes. In fact, it might be noticed that an accurate identification of the *angle of incidence* cannot be achieved using only the IVUS modality, since it is impossible to recover the 3-D geometry of the vessel. A three-dimensional vessel reconstruction using X-ray and IVUS imaging techniques could contribute to the fluid dynamic analysis of the vessel, with main focus on bifurcation sites. Finally, the automatic bifurcation detection method can be applied in large clinical studies investigating the correlation between bifurcation and plaque.

Automatic Non-rigid Temporal Alignment Although satisfactory performances have already been obtained, the framework can be extended in future studies, by investigating the use of different weights for the various morphological features. Moreover, image-based measurements (for instance, entropy) could complete the set of profiles. The developed framework can be applied in clinical studies on atherosclerotic plaque regression/progression by IVUS, to automatically align cases acquired at different times. This method can be a baseline in the research on alignment and fusion of coronary data. Future work can be addressed towards automatic inter-modality alignments, for instance between IVUS and angiographic or Optical Coherence Tomography (OCT) data. Finally, the proposed EPS strategy for partial overlapping has been applied solely to the alignment of the IVUS temporal morphological profiles. As a further step, it would be interesting to apply this generic method to other sequence alignment problems, characterized by partial overlapping between sequences.

Automatic 2-D+T Lumen Border Extraction The main limitation of the lumen detection method consists in the application of the active contour model in 2-D. A future step in this study deals with extending also the last step of the method, i.e., the identification of the luminal contour (which follows the classification phase), to 2-D+T, thus taking into account the lumen continuity in the longitudinal dimension of the sequence. Such study has been planned for the next months investigation.

Appendix A

Medical Imaging Glossary

- **Angiography**: Angiography or arteriography is a medical imaging technique used to visualize the lumen of vessels and organs of the body, with particular interest in the arteries, veins and heart chambers. This is traditionally done by injecting a radio-opaque contrast agent into the blood vessel, and imaging using X-ray based techniques such as fluoroscopy.

- **Atherosclerosis**: A condition in which an artery wall thickens as a result of the accumulation of fatty materials such as cholesterol. It is a chronic inflammatory response in the walls of arteries, caused largely by the accumulation of macrophage cells and promoted by low-density lipoproteins (LDL, plasma proteins that carry cholesterol and triglycerides) without adequate removal of fats and cholesterol from the macrophages. It is commonly referred to as a hardening of the arteries. It evolves with the formation of multiple plaques within the arteries.

- **Blood speckle**: The ultrasound reflection from aggregated blood cells.

- **Collagen**: Elastic protein of the connective tissue, stiffer than elastin. It is responsible for the elasticity of the skin.

- **CT**: X-ray computed tomography, also computed tomography (CT scan) or computed axial tomography (CAT scan), is a medical imaging procedure that uses computer-processed X-rays to produce tomographic images or "slices" of specific areas of the body. These cross-sectional images are used for diagnostic and therapeutic purposes in various medical disciplines. Digital geometry processing is used to generate a three-dimensional image of the inside of an object from a large series of two-dimensional X-ray images, taken around a single axis of rotation.

- **DICOM**: DICOM (Digital Imaging and Communications in Medicine) is a standard for handling, storing, printing, and transmitting information in medical imaging. It includes a file format definition and a network communications protocol.

- **Echogenicity:** The tendency of a tissue to reflect ultrasound. The higher the echogenicity, the brighter the tissue will appear.
- **Elastin**: Protein in connective tissue that is elastic and allows tissues to resume their shape after stretching or contracting.
- **Elastography**: Method using stiffness or strain images of soft tissue for detecting soft tissue tumors. A tumor or cancerous growth is normally 5 to 10 times harder than a normal soft tissue. When a mechanical compression is applied, the tumor is deformed less than the surrounding tissue.
- **Fibrous cap**: A layer of fibrous connective tissue, which is thicker and less cellular than the normal intima. The fibrous cap contains macrophages and smooth muscle cells. The fibrous cap of an atheroma is composed of smooth muscle cells, macrophages, foam cells, lymphocytes, collagen and elastin.
- **Follow-up**: A series of periodic checks after an intervention.
- **Infarction**: Infarction refers to tissue death (necrosis) caused by an obstruction of the tissue blood supply, which leads to a local lack of oxygen.
- **OCT**: Optical coherence tomography (OCT) is an optical signal acquisition and processing method. It captures micrometer-resolution, three-dimensional images from within optical scattering media (e.g., biological tissue). Optical coherence tomography is an interferometric technique, typically employing near-infrared light.
- **Thrombus**: A thrombus, or blood clot, is the final product of the blood coagulation step in hemostasis. A thrombus is normal in cases of injury, but pathologic in instances of thrombosis. When a thrombus occupies more than 75% of the cross-sectional area of the lumen of an artery, blood flow to the tissue supplied is reduced enough to cause symptoms because of decreased oxygen (hypoxia) and accumulation of metabolic products like lactic acid. More than 90% obstruction can result in anoxia, the complete deprivation of oxygen, and infarction, a mode of cell death.
- **Ultrasound**: Sound waves having a frequency 20,000 cycles per second (i.e., above the audible range). For medical diagnostic purposes, ultrasound frequencies in the range of millions of cycles per second (MHz) are used.
- **Ultrasound transducer**: A device that converts energy into ultrasound. Medical ultrasonic transducers (probes) come in a variety of different shapes and sizes, for acquiring images of different parts of the body. The principle behind the technology is that the transmit signal consists of short bursts of ultrasonic energy. After each burst, the electronics looks for a return signal within a window of time.

Appendix B

IVUS Data-sets

In this Appendix, the data-sets of IVUS images used for the validation of the proposed methodologies are described in detail.

B.1 Data-set for Bifurcation Detection

The data-set consists in 22 *in-vivo* pullbacks of coronary arteries, acquired from 22 patients. The sequences have been recorded by means of the iLab IVUS Imaging System (Boston Scientific), available in the Hospital "Germans Trias i Pujol", Badalona (Spain), using a 40 MHz catheter Atlantis SR 40 Pro (Boston Scientific).

The data have been chosen randomly without any exclusion criteria from the hospital database. 14 patients have been monitored pre-operatively, and 8 after PCI. The patient population is composed of 18 men and 4 women ranging in age from 31 to 81 (median 54); there are 4 diabetic patients.

In order to validate the proposed method for bifurcation detection, ground-truth bifurcation labels have been created by manual segmentation performed by two medical experts. To this aim, an ad-hoc interface has been developed, where the user can navigate into the sequence in both longitudinal and angular directions (see Figure B.1). The interface displays the *short-axis view* and the *longitudinal view* of the pullback. The physicians selected the *angular sector* comprising the bifurcation in the *short-axis view*, by selecting the extremes of the angular sector, using the buttons "ALPHA1" and "ALPHA2" in the interface (see Figure B.1). The observers were careful to choose the smallest possible angular extension, thus ensuring the correctness of the training samples for the bifurcation class. Moreover, the interface allows the annotation of the initial and final bifurcation frames (by using the two buttons "INIT" and "END", respectively).

The intersection between the two physicians' segmentations has been used as ground-truth, hence making the most conservative choice. The most experienced of the two observers performed the segmentation of the whole data-set twice, to allow the computation of intra-observer variability.

Each IVUS frame is composed of 360 *angular sector* samples, corresponding to angular degrees and to columns in the polar representation, leading to an average

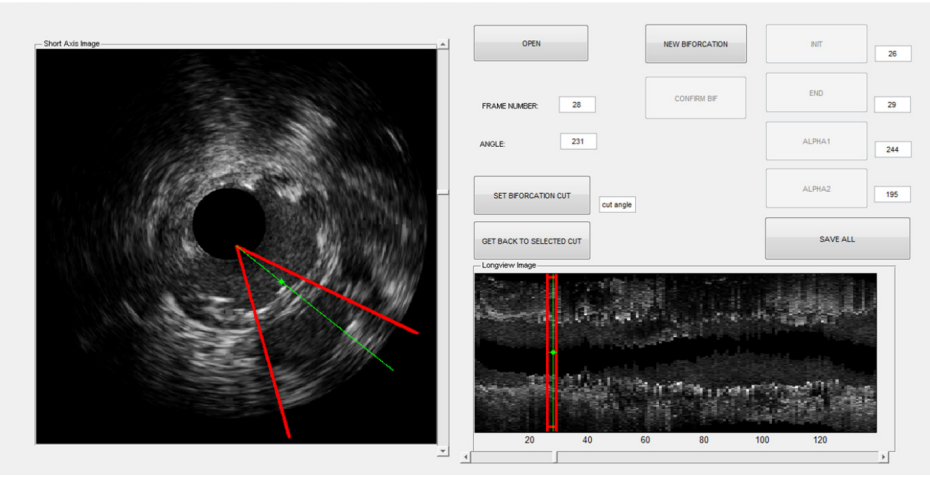

Figure B.1: The interface for labeling the longitudinal and angular position/extension of vascular bifurcations in IVUS.

32,645 data samples per gated sequence. The ground-truth contains a total amount of 72 bifurcation regions, with an average 3.2 bifurcations per sequence. Given that the amount of samples and the variety of bifurcation structures and sizes are large, the data-set can be considered as representative of the possible range of vascular branchings.

B.2 Data-set for Sequence Alignment

The data-set consists of 42 *in-vivo* IVUS pullbacks from human coronary arteries, from 21 patients. The sequences have been acquired in the Hospital "Germans Trias i Pujol", Badalona (Spain) by means of iLab IVUS Imaging System (Boston Scientific). Sequences have been recorded with constant pullback (0.5 mm/sec) using a 40 MHz catheter Atlantis SR 40 Pro (Boston Scientific). All the acquisitions have been performed strictly following the clinical protocol approved by the hospital ethical committee and informed consent for the study has been obtained from all patients.

The clinical data have been randomly chosen without any exclusion criteria. The study population is composed of patients ranging in age from 32 to 82 (median 70); there are 3 diabetic patients. In particular, 37 of the 42 sequences contain a stent, resulting in 20 of the 21 pullback pairs containing stent. In some patients stent is present from previous interventions, while in others it has been deployed during PCI.

The 42 sequences constitute two data-sets aimed at different purposes:

- *Data-set A* is specifically used for the validation of the sequence alignment method only. It consists of 8 pairs of corresponding IVUS pullbacks (16 sequences) acquired at the same stage of the percutaneous intervention (i.e. angioplasty, stent deployment, and/or stent post-dilatation), either before or afterward. Since there are no morphological changes due to intervention, a high

number of manually annotated ground-truth landmarks could be defined. To this aim, the presence of morphological structures, such as small calcifications and external vessels, and the initial and end positions of deployed stent have been considered.

- *Data-set B* reflects the clinical application of the IVUS sequence alignment study, and it contains 13 pairs of corresponding pullbacks (26 sequences), all characterized by significant morphological changes due to percutaneous intervention. Following the same validation strategy employed in [102, 31], only bifurcation locations (initial and end positions) are used as ground-truth. Indeed side branches are the only immutable landmarks, since lumen and media size, stent and plaque might vary due to surgical artery dilatation or stent deployment.

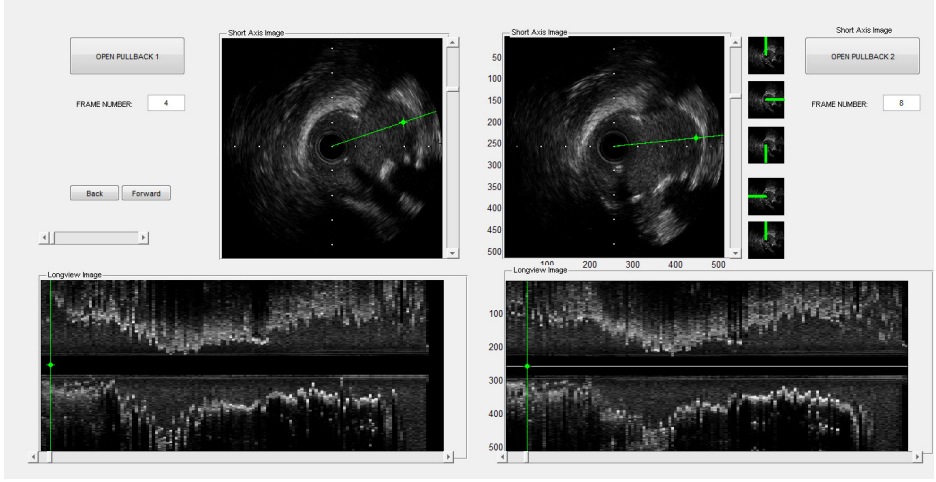

Figure B.2: The interface for labeling pairs of corresponding frames in two IVUS sequences.

Manual annotations have been performed by an expert clinician. The interface for navigating in two pullbacks and visualizing the corresponding frames is shown in Figure B.2. For each sequence, both *short-axis view* and *longitudinal view* are displayed and, in each sequence, the user can navigate in the longitudinal and angular dimensions.

Finally, the *in-vivo* ground-truth consists of a total 98 landmarks in Data-set A (averaging 12.2 landmarks per sequence) and 60 side-branch locations in Data-set B (4.6 landmarks per sequence).

B.3 Data-set for Lumen Border Extraction

The approach for luminal border detection is validated on a data-set provided by the Hospital "German Trias i Pujol" (Data-set A), consisting in 7 sequences from 7

different patients, acquired with an iLab IVUS Imaging System. For each pullback, a vessel segment of 60 successive gated frames, extracted by the image-based gating method proposed in [37], has been considered, for the validation of the proposed 2-D+T approach. *Data-set A* is characterized by the presence of stent in all the sequences. Stent covers a significant amount of frames in the pullback, for a total of 221 stent frames over 420 frames. A challenging data-set has been created for the lumen border detection study, aimed at reflecting the clinical application of lumen border detection. Detecting the lumen in stent frames is particularly important to identify stent malapposition and stent under-expansion. The reference annotation of the luminal border has been manually performed by a physician.

Moreover, the approach has been tested on two data-sets, provided in the context of the "Lumen + External Elastic Laminae (Vessel Inner and Outer Wall) Border Detection in IVUS Challenge" associated with the MICCAI 2011 workshop on Computing and Visualization for (Intra)Vascular Imaging (CVII).

The data-sets contain data extracted from *in-vivo* pullbacks of human coronary arteries performed during PCI, acquired with a 40 MHz probe (Data-set B) and with a 20 MHz probe (Data-set C), respectively:

- *Data-set B* is composed of 77 frames, from 22 patients. The data are obtained from a digital iLab IVUS Imaging System (Boston Scientific) equipped with a 40 MHz catheter Atlantis SR 40 Pro (Boston Scientific). The images have been used in DICOM (40 MHz) format. For each frame, four adjacent images (two previous and two successive to the extracted frame) are also provided. The groups of adjacent frames have been chosen at random instants of the cardiac cycle (not gated).

- *Data-set C* is composed of 435 frames, from 10 patients. The data are obtained from a 20 MHz Volcano IVUS scanner (Volcano Corporation) equipped with a 20 MHz 2.9 F Eagle Eye monorail catheter. The images have been provided in DICOM (20 MHz) format. For each frame, four adjacent images are also available. The data-set contains 2-D+T gated sequences, consisting of 20-50 frames extracted at the end diastolic phase, which provide sufficient spatial context for the proposed 2-D+T methodology.

Ground-truth labels have been created by manual segmentation of the luminal border performed by two observers.

Appendix C

Publications

Refereed journals

- Marina Alberti, Simone Balocco, Carlo Gatta, Francesco Ciompi, Oriol Pujol, Joana Silva, Xavier Carrillo and Petia Radeva, Automatic Bifurcation Detection in Coronary IVUS Sequences. *IEEE Transactions on Biomedical Engineering*, 59 (4), pages: 1022-2031, 2012.

- Francesco Ciompi, Oriol Pujol, Carlo Gatta, Marina Alberti, Simone Balocco, Xavier Carrillo, Josepa Mauri-Ferre and Petia Radeva, HoliMAb: A holistic approach for MediaAdventitia border detection in intravascular ultrasound. *Medical Image Analysis*, 16 (6), pages: 1085-1100, 2012.

- Simone Balocco, Carlo Gatta, Marina Alberti, Xavier Carrillo, Juan Rigla and Petia Radeva, Relation between plaque type, plaque thickness, blood shear stress and plaque stress in coronary arteries assessed by X-ray Angiography and Intravascular Ultrasound. *Medical Physics*, 39 (12), pages: 7430-7445, 2012.

- Marina Alberti, Simone Balocco, Xavier Carrillo, Josepa Mauri and Petia Radeva, Automatic non-rigid temporal alignment of IVUS sequences: method and quantitative validation. *Ultrasound in Medicine and Biology*. Under review.

- S. Balocco, C. Gatta, F. Ciompi, A. Wahle, P. Radeva, S. Carlier, G. Unal, E. Sanidas, F. Mauri, X. Carillo, T. Kovarnik, C. Wang, H. Chen, T. P. Exarchos, D. I. Fotiadis, F. Destrempes, G. Cloutier, O. Pujol, M. Alberti, E. G. Mendizabal-Ruiz, M. Rivera, T. Aksoy, R. W. Downe and I. Kakadiaris, Standardized evaluation methodology and reference database for evaluating IVUS image segmentation, *Computerized Medical Imaging and Graphics*. Under review.

Refereed major conferences

- Marina Alberti, Simone Balocco, Xavier Carrillo, Josepa Mauri and Petia Radeva, Automatic Non-Rigid Temporal Alignment of IVUS Sequences, *MICCAI 2012: 15th International Conference on Medical Image Computing and Computer Assisted Intervention*, Nice, France, Volume 1, pages: 642-650. October, 2012.
- Marina Alberti, Simone Balocco, Carlo Gatta, Francesco Ciompi, Oriol Pujol, Joana Silva, Xavier Carrillo and Petia Radeva, Automatic Branching Detection in IVUS Sequences, *IBPRIA 2011: 5th Iberian Conference on Pattern Recognition and Image Analisis*, Las Palmas de Gran Canaria, Spain, pages: 126-133. June, 2011.

Patents

- SYSTEMS AND METHODS FOR DETECTING AND DISPLAYING BODY LUMEN BIFURCATIONS
  U.S. Patent Application No. 61/510,014
  Filing date: September 23, 2011
  Publication date: May 31, 2012
  Owner: Boston Scientific Corporation
  Inventor(s): S. Balocco, M. Alberti, C. Gatta, F. Ciompi, O. Pujol, X. Carrillo, J. Mauri, P. Radeva, O. Rodriguez, E. Fernandez-Nofrerias.
- SYSTEMS AND METHODS FOR NAVIGATING AND VISUALIZING INTRAVASCULAR ULTRASOUND SEQUENCES
  U.S. Patent Application No. 13/462,733
  Filing date: May 2, 2012
  Publication date: November 8, 2012
  Owner: Boston Scientific Corporation
  Inventor(s): F. Ciompi, J. Mauri Ferre, O. Pujol, X. Carrillo, P. Radeva, C. Gatta, S. Balocco, E. Fernandez-Nofrerias, M. Alberti, O. Rodriguez.

Workshops

- Rui Hua, Oriol Pujol, Francesco Ciompi, Marina Alberti, Simone Balocco, Josepa Mauri and Petia Radeva, Stent Strut Detection by Classifying a Wide Set of IVUS Features. *Computed Assisted Stenting Workshop, MICCAI 2012: 15th International Conference on Medical Image Computing and Computer Assisted Intervention*, Nice, France, October, 2012.
- Marina Alberti, Simone Balocco, Xavier Carrillo, Josepa Mauri and Petia Radeva, Automatic Non-Rigid Temporal Alignment of IVUS Sequences, *CVCRD'12: Seventh CVC Workshop on Advances in Theory and Application of Computer Vision*, Barcelona, Spain, October, 2012.

- Marina Alberti, Simone Balocco, Xavier Carrillo, Josepa Mauri and Petia Radeva, 3D Automatic Luminal Border Detection in IVUS Sequences, *MICCAT 2011: The second workshop on Medical Imaging in Catalunya*, Barcelona, Spain, December, 2011.
- Marina Alberti, Simone Balocco, Xavier Carrillo, Josepa Mauri and Petia Radeva, 3D Automatic Lumen Detection, *CVCRD'11: State of the art of Research and Development*, Barcelona, Spain, October, 2011.
- Marina Alberti, Carlo Gatta, Simone Balocco, Francesco Ciompi, Oriol Pujol and Petia Radeva, Towards Automatic Branching Detection in IVUS Sequences. *CVCRD'10: Progress of Research and Development*, Barcelona, Spain, October, 2010.

Projects

- **CONSOLIDER-INGENIO 2010 MIPRCV**: Multimodal interaction in pattern recognition and computer vision.
- **CICYT TIN2009-14404-C02-02**: Machine learning techniques for large scale vision systems: application to medical image analysis.
- **Lumen Border Detection**: Reseach activities based on pre-determined, prioritized list of IVUS-Related research topic of interest of BSS.

Bibliography

[1] M. Alberti, S. Balocco, X. Carrillo, J. Mauri, and P. Radeva. Automatic non-rigid temporal alignment of ivus sequences. In *MICCAI*, volume 1, pages 642–650, 2012.

[2] M. Alberti, S. Balocco, C. Gatta, F. Ciompi, O. Pujol, J. Silva, X. Carrillo, and P. Radeva. Automatic bifurcation detection in coronary ivus sequences. *IEEE Trans. Biomed. Engineering*, 59(4):1022–1031, 2012.

[3] J. Amores and P. Radeva. Registration and retrieval of highly elastic bodies using contextual information. *Pattern Recognition Letters*, 26:1720–1731, 2005.

[4] T. Asakura and T. Karino. Flow patterns and spatial distribution of atherosclerotic lesions in human coronary arteries. *Circulation Research*, 66(4):1045–1066, April 1990.

[5] S. Balocco, C. Gatta, M. Alberti, J. Rigla, and P. Radeva. Relation between plaque type, plaque thickness, blood shear stress and plaque stress in coronary arteries assessed by x-ray angiography and intravascular ultrasound. *Medical Physics*, In press, 2012.

[6] S. Balocco, C. Gatta, F. Ciompi, O. Pujol, X. Carrillo, J. Mauri, and P. Radeva. Combining growcut and temporal correlation for ivus lumen segmentation. In *IbPRIA*, pages 556–563, 2011.

[7] J. Barajas, K. L. Caballero, O. Rodriguez, and P. Radeva. Cardiac phase extraction in ivus sequences using 1-d gabor filters. In *IEEE EMBS*, pages 343–346, 2007.

[8] D. Bedekar. Atherosclerotic plaque characterization by acoustic impedance analysis of intravascular ultrasound data. In *IEEE Ultrasonic Symposium*, 2003.

[9] Ernst G. P. Bovenkamp, Jouke Dijkstra, Johan G. Bosch, and Johan H. C. Reiber. Multi-agent segmentation of ivus images. *Pattern Recognition*, 37(4):647–663, 2004.

[10] A.C. Bovik, M. Clark, and W.S. Geisler. Multichannel texture analysis using localized spatial filters. *PAMI*, 12:55–73, 1990.

[11] Leo Breiman. Random forests. *Machine Learning*, 45:5–32, 2001.

[12] N. Bruining, C. von Birgelen, F. Prati, M.T. Mallus, W. Li, W. Den Hoed, M. Patijn, P.J. de Feyter, P.W. Serruys, and J.R.T.C. Roelandt. Dynamic three-dimensional reconstruction of icus images based on an ecg-gated pull-back device. In *EMBS*, 1996.

[13] E. Brusseau and C.L. de Korte. Fully automatic luminal contour segmentation in intracoronary ultrasound imaging - a statistical approach. *IEEE Transactions on Medical Imaging*, 23(5):554–566, May 2004.

[14] Karla L. Caballero, Joel Barajas, Oriol Pujol, Oriol Rodriguez, and Petia Radeva. Using reconstructed ivus images for coronary plaque classification. In *EMBS*, pages 2167–2170, 2007.

[15] C. Canero, F. Vilarino, J. Mauri, and P. Radeva. Predictive (un)distortion model and 3-d reconstruction by biplane snakes. *IEEE Trans Med Imaging*, 21:1188–1201, 2002.

[16] M.H. Cardinal, J. Meunier, G. Soulez, R.L. Maurice, E. Therasse, and G. Cloutier. Intravascular ultrasound image segmentation: A three-dimensional fast-marching method based on gray level distributions. *IEEE Transactions on Medical Imaging*, 25(5):590–601, 2006.

[17] Stéphane G. Carlier, Kaoru Tanaka, and Amin Katouzian. Atherosclerotic plaque characterization from radio frequency ultrasound signal processing. *US Cardiology*, 4:54–56, 2007.

[18] E. Castro and C. Morandi. Registration of translated and rotated images using finite fourier transforms. *IEEE PAMI*, 9:700–703, 1987.

[19] F. Ciompi, C. Gatta, O. Pujol, O.Rodríguez-Leor, J.Mauri-Ferré, and P. Radeva. *Reconstruction and Analysis of Intravascular Ultrasound Sequences*, chapter 15, pages 223–243. Bentham Science, 2010.

[20] F. Ciompi, O. Pujol, C. Gatta, O. R. Leor, J. M. Ferre, and P. Radeva. Fusing in-vitro and in.vivo intravascular ultrasound data for plaque characterization. *Int J Cardiovasc Imaging*, 26:763–779, 2010.

[21] Francesco Ciompi, Oriol Pujol, Eduard Fernández-Nofrerías, Josepa Mauri, and Petia Radeva. Ecoc random fields for lumen segmentation in radial artery ivus sequences. In *MICCAI '09: Proceedings of the 12th International Conference on Medical Image Computing and Computer-Assisted Intervention*, pages 869–876, Berlin, Heidelberg, 2009. Springer-Verlag.

[22] Francesco Ciompi, Oriol Pujol, Carlo Gatta, Marina Alberti, Simone Balocco, Xavier Carrillo, Josepa Mauri-Ferre, and Petia Radeva. Holimab: a holistic approach for media-adventitia border detection in intravascular ultrasound. *Medical Image Analysis*, 16(6):1085–1100, 2012.

[23] Corinna Cortes and Vladimir Vapnik. Support-vector networks. In *Machine Learning*, volume 20, pages 273–297, 1995.

[24] M. Danilouchkine, F. Mastik, and A. van der Steen. Accuracy in prediction of catheter rotation in ivus with feature-based optical flow: A phantom study. *IEEE TITB*, 13:356–365, 2008.

[25] Sanmay Das. Filters, wrappers and a boosting-based hybrid for feature selection. In *Proceedings of the Eighteenth International Conference on Machine Learning*, pages 74–81, 2001.

[26] M. J. Davies and A. C. Thomas. Plaque fissuring–the cause of acute myocardial infarction, sudden ischaemic death, and crescendo angina. *British Heart Journal*, 53:363–373, 1985.

[27] C. L. de Korte, G. Pasterkamp, A. F. W. van der Steen, H. A. Woutman, and N. Bom. Characterization of plaque components with intravascular ultrasound elastography in human femoral and coronary arteries in vitro. *Circulation*, 102:617–623, 2000.

[28] Janez Demsar. Statistical comparisons of classifiers over multiple data sets. *Journal of Machine Learning Research*, 7:1–30, 2006.

[29] A. Van der Steen, C. de Korte, J. Schaar, F. Mastik, R. Baldewsing, and P. Serruys. 3d intravascular ultrasounds palpography for vulnerable plaque detection. In *IEEE International Symposium on Biomedical Imaging: Nano to Macro*, 2005.

[30] S. deWinter, R. Hamers, M. Degertekin, K. Tanabe, P. A. Lemos, P. W. Serruys, J. R. Roelandt, and N. Bruining. Retrospective imagebased gating of intracoronary ultrasound images for improved quantitative analysis: The intelligate method. *Catheterization and Cardiovascular Diagnosis*, 61:84–94, 2006.

[31] R. Diletti, H. M. Garcia-Garcia, J. Gomez-Lara, S. Brugaletta, J. J. Wykrzykowska, N. van Ditzhuijzen, R. J. van Geuns, E. Regar, G. Ambrosio, and P. W. Serruys. Assessment of coronary atherosclerosis progression and regression at bifurcations using combined ivus and oct. *JACC Cardiovasc Imaging*, 4:774–780, 2011.

[32] R. W. Downe, A. Wahle, T. Kovarnik, H. Skalicka, J. J. Lopez, J. Horak, and M. Sonka. Segmentation of intravascular ultrasound images using graph search and a novel cost function. In *Proc. 2nd MICCAI Workshop on Computer Vision for Intravascular and Intracardiac Imaging*, pages 71–79, New York, NY, Sep. 10 2008.

[33] S. G. Ellis. *Strategic Approaches in Coronary Intervention.* Lippincott Williams and Wilkins, 2006.

[34] Erling Falk, Prediman K. Shah, and Valentin Fuster. Coronary plaque disruption. *Circulation*, 92:657–671, 1995.

[35] Yoav Freund and Robert E. Schapire. A decision-theoretic generalization of online learning and an application to boosting. *Journal of Computer and System Sciences*, 55(1):119–139, 1997.

[36] V. Fuster, P. R. Moreno, Z. A. Fayad, R. Corti, and J. J. Badimon. Atherothrombosis and high-risk plaque. *Journal of the American College of Cardiology*, 46:937–954, 2005.

[37] Carlo Gatta, Simone Balocco, Francesco Ciompi, Rayyan Hemetsberger, Oriol Rodriguez-Leor, and Petia Radeva. Real-time gating of ivus sequences based on motion blur analysis: Method and quantitative validation. In *MICCAI*, pages 59–67, 2010.

[38] Carlo Gatta, Eloi Puertas, and Oriol Pujol. Multi-scale stacked sequential learning. *Pattern Recognition*, 44:2414 – 2426, 2011.

[39] Carlo Gatta, Oriol Pujol, Oriol Rodriguez Leor, Josepa Mauri Ferre, and Petia Radeva. Robust image-based ivus pullbacks gating. In *MICCAI '08: Proceedings of the 11th International Conference on Medical Image Computing and Computer-Assisted Intervention, Part II*, pages 518–525, Berlin, Heidelberg, 2008. Springer-Verlag.

[40] Carlo Gatta, Oriol Pujol, Oriol Rodriguez Leor, Josepa Mauri Ferre, and Petia Radeva. Fast rigid registration of vascular structures in ivus sequences. *TITB*, 13(6):1006–1011, 2009.

[41] G. D. Giannoglu, Y. S. Chatzizisis, V. Koutkias, I. Kompatsiaris, M. Papa, V. Mezaris, E. Parissi, P. Diamantopoulus, M. G. Strintzis, N. Maglaveras, G. E. Parcharidis, and G. E. Louridas. A novel active countour model for fully automated segmentation of intravascular ultrasound images: in vivo validation in human coronary arteries. *Computers in Biology and Medicine*, 37:1292–1302, 2007.

[42] D. Gil, A. Hernandez, O. Rodriguez, J. Mauri, and P. Radeva. Statistical strategy for anisotropic adventitia modelling in IVUS. *IEEE Transactions on Medical Imaging*, 25(6):768–78, 2006.

[43] C. Haas, H. Ermert, S. Holt, P. Grewe, A. Machraoui, and J. Barmeyer. Segmentation of 3D intravascular ultrasonic images based on a random field model. *Ultrasound in Medicine and Biology*, 26(2):297–306, 2000.

[44] G. K. Hansson. Inflammation, atherosclerosis, and coronary artery disease. *N eng J Med*, 352:1685–1695, 2005.

[45] A. Hernandez, P. Radeva, A. Tovar, and D. Gil. Vessel structures alignment by spectral analysis of ivus sequences. In *Proceedings of Computer Vision for Intravascular and Intracardiac Imaging (CVII)*, 2006.

[46] D. M. Herrington, T. Johnson, P. Santago, and W. E. Snyder. Semi-automated boundary detection for intravascular ultrasound. *Computers in Cardiology*, pages 103–106, 1992.

[47] J. N. Holmes. *Speech Synthesis and Recognition.* Taylor & Francis, Inc., 1988.

[48] P. Radeva J. Amores, N. Sebe. Context-based object-class recognition and retrieval by generalized correlograms. *IEEE PAMI*, 29:1818–1833, 2007.

[49] Michael Kass, Andrew P. Witkin, and Demetri Terzopoulos. Snakes: Active contour models. *International Journal of Computer Vision*, 1(4):321–331, 1988.

[50] A. Katouzian, E. D. Angelini, S. G. Carlier, J. S. Suri, N. Navab, and A. F. Laine. A state-of-the-art review on segmentation algorithms in intravascular ultrasound (ivus) images. *IEEE Trans Inf Technol Biomed*, 15(5):823–834, 2012.

[51] A. Katouzian, B. Baseri, E.E. Konofagou, and A.F. Laine. Automatic detection of blood versus non-blood regions on intravascular ultrasound (IVUS) images using wavelet packet signatures. In *Proc. SPIE Medical Imaging 2008: Ultrasonic Imaging and Signal Processing*, San Diego, CA, Feb. 16 - 21 2008.

[52] A. Katouzian, S. Sathyanarayana, B. Baseri, E. E. Konofagou, and S. G. Carlier. Challenges in atherosclerotic plaque characterization with intravascular ultrasound (ivus): from data collection to classification. *IEEE TITB*, 12:315–327, 2008.

[53] D. G. Katritsis, E. P. Efstathopoulos, J. Pantos, S. Korovesis, G. Kourlaba, S. Kazantzidis, V. Marmarelis, and E. Voridis. Anatomic characteristics of culprit sites in acute coronary syndromes. *Journal of Interventional Cardiology*, 21(2):140–150, 2008.

[54] B. J. Kimura, R. J. Russo, V. Bhargava, M. B. McDaniel, K. L. Peterson, and A. N. DeMaria. Atheroma morphology and distribution in proximal left anterior descending coronary artery: in vivo observations. *Journal of the American College of Cardiology*, 27:825–831, 1996.

[55] J. D. Klingensmith, R. Shekhar, and D. G. Vince. Evaluation of three-dimensional segmentation algorithms for the identification of luminal and medial-adventitial borders in intravascular ultrasound images. *IEEE Trans Med Imaging*, 19(10):996–1011, Oct 2000.

[56] Hildegard Koehler, Michel Couprie, Sahla Bouattour, and Dietrich Paulus. Extraction and analysis of coronary tree from single x-ray angiographies. In *ISMI*, pages 810–819, 2004.

[57] G. Kovalski, R. Beyar, R. Shofti, and H. Azhari. Three-dimensional automatic quantitative analysis of intravascular ultrasound images. *Ultrasound in Medicine and Biology*, 26(4):527–537, 2000.

[58] T. Kovarnik, A. Wahle, R. W. Downe, and M. Sonka. *Intrvascular Ultrasound*, chapter IVUS Role in Studies Assessing Atherosclerosis Development, pages 53–68. InTech, 2012.

[59] N. Kudo, T. Kanenari, X. Zhang, and K. Yamamoto. In vitro study on arterial lumen detection using a correlation technique in ivus. In *EMBS*, volume 2, pages 830 –831 vol.2, 29 1998.

[60] W. Li, A.F.W. van der Steen, C.T. Lancée, J. Honkoop, E. J. Gussenhoven, and N. Bom. Temporal correlation of blood scattering signals in vivo from radio frequency intravascular ultrasound. *Ultrasound in Medicine and Biology*, 22(5):583–590, 1996.

[61] Gareth Loy and Er Zelinsky. A fast radial symmetry transform for detecting points of interest. In *Proceeding ot the 7th Euproean Conference on Computer Vision*, page 358. Springer, 2002.

[62] Z. Luo, Y. Wang, and W. Wang. Estimating coronary artery lumen area with optimization-based contour detection. *IEEE Transactions on Medical Imaging*, 22:564–546, Apr. 2003.

[63] H. A. Marquering, J. Dijkstra, Q. J. A. Besnehard, Julien P. M. Duthè, Joanne D Schuijf, J. J. Bax, and J. H. C. Reiber. Coronary ct angiography: Ivus image fusion for quantitative plaque and stenosis analyses. In *SPIE*, 2008.

[64] R. L. Maurice, J. Fromageau, M. H. R. Cardinal, M. Doyley, E. de Muinck, and G. Cloutier J. Robb. Characterization of atherosclerotic plaques and mural thrombi with intravascular ultrasound elastography: a potential method evaluated in an aortic rabbit model and a human coronary artery. *IEEE TITB*, 12:290–298, 2008.

[65] E. G. Mendizabal-Ruiz, G. Biros, and I. A. Kakadiaris. An inverse scattering algorithm for the segmentation of the luminal border on intravascular ultrasound data. In *MICCAI*, 2009.

[66] E.G. Mendizabal-Ruiz, M. Rivera, and I.A. Kakadiaris. A probabilistic segmentation method for the identification of luminal borders in intravascular ultrasound images. In *Proc. IEEE Computer Society Conference on Computer Vision and Pattern Recognition*, pages 1–8, Anchorage, AK, Jun. 24-26 2008.

[67] A.B. Merle, G. Finet, J. Lienard, and I.E. Magnin. 3d reconstruction of the deformable coronary tree skeleton from two x-ray angiographic views. In *Computers in Cardiology*, pages 757 –760, 1998.

[68] M. Milunski, G. Mohr, J. Perez, Z. Vered, K. A. Wear, C. J. Gessler, B. E. Sobel, J. Miller, and S. A. Wickline. Ultrasonic tissue characterization with integrated backscatter. acute myocardial ischemia, reperfusion, and stunned myocardium in patients. *Circulation*, 80:491–503, 1989.

[69] Gary S Mintz, Steven E Nissen, William D Anderson, Steven R Bailey, Raimund Erbel, Peter J Fitzgerald, Fausto J Pinto, Kenneth Rosenfield, Robert J Siegel, E.Murat Tuzcu, Paul G Yock, Robert A O'Rourke, Jonathan Abrams, Eric R Bates, Bruce R Brodie, Pamela S Douglas, Gabriel Gregoratos, Mark A Hlatky, Judith S Hochman, Sanjiv Kaul, Cynthia M Tracy, David D Waters, and William L Winters. American college of cardiology clinical expert consensus document on standards for acquisition, measurement and reporting of intravascular ultrasound studies. *J Am Coll Cardiol*, 37:1478–1492, 2001.

[70] A. Mojsilovic, M. Popovic, N. Amodaj, R. Babic, and M. Ostojic. Automatic segmentation of intravascular ultrasound images: A texture-based approach. *Annals of Biomedical Engineering*, 25(6):1059–1071, Nov. 1997.

[71] James E Moore, Lucas H Timmins, and John F Ladisa. Coronary artery bifurcation biomechanics and implications for interventional strategies. *Catheterization and Cardiovascular Interventions*, 76:836–843, 2010.

[72] A. Murashige, T. Hiro, T. Fujii, K. Imoto, T. Murata, Y. Fukumoto, and M. Matsuzaki. Detection of lipid-laden atherosclerotic plaque by wavelet analysis of radiofrequency intravascular ultrasound signals: In vitro validation and preliminary in vivo application. *Journal of the American College of Cardiology*, 45:1954–1960, 2005.

[73] A. Nair, B. D. Kuban, N. Obuchowski, and G. D. Vince. Assessing spectral algorithms to predict atherosclerotic plaque composition with normalized and raw intravascular ultrasound data. *Ultrasounf in Medicine and Biology*, 27:1319–1331, 2001.

[74] Anuja Nair, Barry D. Kuban, E. Murat Tuzcu, Paul Shoenhagen, Steven E. Nissen, and D. Geoffrey Vince. Coronary plaque classification with intravascular ultrasound radiofrequency data analysis. *Circulation*, 106:2200–2206, 2002.

[75] T. Nakayama, N. Komiyama, M. Yokoyama, S. Namikawa, N. Kuroda, Y. Kobayashi, and I. Komuro. Pioglitazone induces regression of coronary atherosclerotic plaques in patients with type 2 diabetes mellitus or impaired glucose tolerance: a randomized prospective study using intravascular ultrasound. *Int J Cardiol*, 138:157–165, 2010.

[76] Gonzalo Navarro. A guided tour to approximate string matching. *ACM Comput. Surv.*, 33:31–88, 2001.

[77] N. P. V. Nielsen, J. M. Carstensen, and J. Smedsgaard. Aligning of single and multiple wavelength chromatographic profiles for chemometric data analysis using correlation optimised warping. *J Chromatogr*, 805:17–35, 1998.

[78] S. E. Nissen, S. J. Nicholls, I. Sipahi, and et al. Effect of very high-intensity statin therapy on regression of coronary atherosclerosis: The asteroid trial. *JAMA: The Journal of the American Medical Association*, 295(13):1556–1565, 2006.

[79] Timo Ojala, Matti Pietikäinen, and Topi Mäenpää. Multiresolution gray-scale and rotation invariant texture classification with local binary patterns. *PAMI*, 24(7):971–987, 2002.

[80] M. Olszewski, A. Wahle, S. Mitchell, and M. Sonka. Segmentation of intravascular ultrasound images: a machine learning approach mimicking human vision. In *International Congress Series*, 2004.

[81] S. M. O'Malley, S. G. Carlier, M. Naghavi, and I. A. Kakadiaris. Image-based frame gating of ivus pullbacks: A surrogate for ecg. In *IEEE International Conference on Acoustics, Speech and Signal Processing*, 2007.

[82] S. M. O'Malley, J. F. Granada, S. Carlier, M. Naghavi, and I. A. Kakadiaris. Image-based gating of intravascular ultrasound pullback sequences. *IEEE Trans. Inf. Technol. Biomed.*, 12:299–306, 2008.

[83] Sean M. O'Malley, Morteza Naghavi, and Ioannis A. Kakadiaris. One-class acoustic characterization applied to blood detection in ivus. In *MICCAI*, pages 202–209, 2007.

[84] Maria Papadogiorgaki, Vasileios Mezaris, Yiannis S Chatzizisis, George D Giannoglou, and Ioannis Kompatsiaris. Image analysis techniques for automated IVUS contour detection. *Ultrasound in medicine & biology*, 34(9):1482–98, September 2008.

[85] M.E. Plissiti, D.I. Fotiadis, L.K. Michalis, and G.E. Bozios. An automated method for lumen and media-adventitia border detection in a sequence of IVUS frames. *IEEE Transactions on Information Technilogy in Biomedicine*, 8(2):131–141, Jun. 2004.

[86] O. Pujol, P. Radeva, J. Mauri, and E. Nofrerias-Fernandez. Automatic segmentation of lumen in intravascular ultrasound images: An evaluation of texture feature extractors. In *Proc. Iberamia*, 2002.

[87] Oriol Pujol and Petia Radeva. Near real time plaque segmentation of ivus. In *Proceedings of Computers in Cardiology*, 2003.

[88] H. Ramaker, E. N. M. van Sprang, J. A. Westerhuis, and A. K. Smilde. Dynamic time warping of spectroscopic batch data. *Analytica Chimica Acta*, 498:133–153, 2003.

[89] Ryan Rifkin and Aldebaro Klautau. In defense of one-vs-all classification. *Journal of Machine Learning Research*, 5:101–141, 2004.

[90] V. L. Roger, A. S. Go, D. M. Lloyd-Jones, E. J. Benjamin, J. D. Berry JD, W. B. Borden, D. M. Bravata, S. Dai, E. S. Ford, C. S. Fox, H. J. Fullerton, C. Gillespie, S. M. Hailpern, J. A. Heit, V. J. Howard, B. M. Kissela, S. J. Kittner, D. T. Lackland, J. H. Lichtman, L. D. Lisabeth, D. M. Makuc, G. M. Marcus, A. Marelli, D. B. Matchar, C. S. Moy, D. Mozaffarian, M. E. Mussolino, G. Nichol, N. P. Paynter, E. Z. Soliman, P. D. Sorlie, N. Sotoodehnia, T. N. Turan, S. S. Virani, N. D. Wong, D. Woo, and M. B. Turner. Heart disease and stroke statistics–2012 update: a report from the american heart association. *Circulation*, 125:e1002, 2012.

[91] M. Rosales, P. Radeva, O. Rodriguez-Leor, and D. Gil. Modelling of image-catheter motion for 3-d ivus. *Medical Image Analysis*, 13:91–104, 2009.

[92] D. Rotger, M. Rosales, J. García, O. Pujol, J. Mauri, and P. Radeva. Active vessel: A new multimedia workstation for intravascular ultrasound and angiography fusion. *Computers in Cardiology*, 30:65–68, 2003.

[93] David Rotger, Petia Radeva, Eduard Fernandez-Nofrerias, and Josepa Mauri. Blood detection in ivus images for 3d volume of lumen changes measurement due to different drugs administration. In *Proceedings of the 12th international conference on Computer Analysis of Images and Patterns*, pages 285–292, 2007.

[94] H. Sakoe and S. Chiba. Dynamic programming algorithm optimization for spoken word recognition. *IEEE Transactions on Acoustics, Speech and Signal Processing*, 26:43–49, 1978.

[95] S. Sathyanarayana, S. Carlier, W. Li, and Lewis Thomas. Characterization of atheroscelrotic plaque by spectral similarity of radiofrequency intravascular ultrasound signals. *EuroIntervention*, 5:133–139, 2009.

[96] S. Sathyaranayana, S. Carlier, L. Wenguang, and L. Thomas. Characterization of atherosclerotic plaque by spectral similarity of radiofrequency intravascular ultrasound. *EuroIntervention*, 5:133–139, 2009.

[97] J. A. Schaar, E. Regar, F. Mastik, E. P. McFadden, F. Saia, C. Disco, C. L. deKorte, P. J. de Feyter, A. F. van der Steen, and P.W. Serruys. Characterizing vulnerable plaque features with intravascular elastography. *Circulation*, 109:2716–2719, 2004.

[98] P. Schoenhagen, R. D. White, S. E. Nissen, and E. M. Tuzcu. Coronary imaging: Angiography shows the stenosis, but ivus, ct, and mri show the plaque. *Cleveland Clinic JournalL of Medicine*, 70:713–719, 2003.

[99] P. Sellers. The theory and computation of evolutionary distances: Pattern recognition. *J Algorithm*, 1:359–373, 1980.

[100] Jean Serra. *Image Analysis and Mathematical Morphology.* Academic Press, Inc., Orlando, FL, USA, 1983.

[101] Shahriar Shariat and Vladimir Pavlovic. Isotonic cca for sequence alignment and activity recognition. In *ICCV*, 2011.

[102] E. S. Shin, H. M. Garcia-Garcia, T. Okamura, and P. W. Serruys. Effect of statins on coronary bifurcation atherosclerosis: an intravascular ultrasound virtual histology study. *Int J Cardiovasc Imaging*, In press, 2011.

[103] C. J. Slager, M. Laban, C. von Birgelen, R. Krams, J. A. F. Oomen, A. den Boer, L. Wenguang, P. J. deFeyter, P. J. Serruys, and J. R. T. C. Roelandt. Angus: a new approach to three-dimensional reconstruction of geometry and orientation of conoary lumen and plaque by combined use of conoary angiography and ivus. *J Am Coll Cardiol*, 25:144A, 1995.

[104] Cornelis J. Slager, Jolanda J. Wentzel, Johan C. H. Schuurbiers, Jan A. F. Oomen, MD Jeroen Kloet, Rob Krams, Clemens von Birgelen, Willem J. van der Giessen Patrick W. Serruys, and Pim J. de Feyter. True 3-dimensional reconstruction of coronary arteries in patients by fusion of angiography and ivus (angus) and its quantitative validation. *Circulation*, 102:511–516, 2000.

[105] T. F. Smith and M. S. Waterman. Identification of common molecular subsequences. *J Mol Biol*, 147:195–197, 1981.

[106] M. Sonka, X. Xhang, M. Siebes, M. S. Bissing, S. C. Dejong, S. M. Collins, and C. R. McKay. Segmentation of intravascular ultrasound images: a knowledge-based approach. *IEEE TMI*, 14:719–732, 1995.

[107] Zheng Sun and Cun Liu. A parallel method for segmenting intravascular ultrasound image sequence. *Applied Mechanics and Materials*, 130-134:2051–2055, 2011.

[108] Arash Taki, Zahra Najafi, Alireza Roodaki, S. K. Setarehdan, R. a. Zoroofi, Andreas Konig, and Nassir Navab. Automatic segmentation of calcified plaques and vessel borders in IVUS images. *International Journal of Computer Assisted Radiology and Surgery*, 3(3-4):347–354, June 2008.

[109] T. Thim, M. K. Hagensen, D. Wallace-Bradley, J. F. Granada, G. L. Kaluza, L. Drouet, W. P. Paaske, H. E. Botker, and E. Falk. Unreliable assessment of necrotic core by virtual histology intravascular ultrasound in porcine coronary artery disease. *Circ Cardiovasc Imaging*, 3:384–391, 2010.

[110] S. Tu, N. R. Holm, G. Koning, Z. Huang, and J. H. C. Reiber. Fusion of 3d qca and ivus/oct. *Int J Cardiovasc Imaging*, 27:197–207, 2011.

[111] G. Unal, S. Bucher, S. Carlier, G. Slabaugh, T. Fang, and K. Tanaka. Shape-driven segmentation of the arterial wall in intravascular ultrasound images. *IEEE Transactions on Information Technology in Biomedicine*, 12(3):335–347, May 2008.

[112] G. Unal, S. Lankton, and G. Slabaugh. Fusion of ivus and oct trough semi automatic registration. In *MICCAI CVII*, 2006.

[113] A. G. van der Giessen, M. Schaap, F. J. Gijsen, H. C. Groen, T. van Walsum, N. R. Mollet, J. Dijkstra, F. N. van de Vosse, W. J. Niessen, P. J. de Feyter, A. F. van der Steen, and J. J. Wentzel. 3d fusion of intravascular ultrasound and coronary computed tomography for in-vivo wall shear stress analysis: a feasibility study. *Int J Cardiovasc Imaging*, 26:781–796, 2010.

[114] M. Vlachos, M. Hadjieleftheriou, D. Gunopoulos, and E. Keogh. Indexing multidimensional time-series with support for multiple distance measures. In *Proceedings of ACM SIGKDD*, pages 216–225, 2003.

[115] C. von Birgelen, C.D. Mario, W. Li, J.C.H. Schuurbiers, C.J. Slager, P.J. de Feyter, P.W. Serruys, and J.R.T.C. Roelandt. Morphometric analysis in

three-dimensional intracoronary ultrasound: An in vitro and in vivo study using a novel system for the contour detection of lumen and plaque. *American Heart Journal*, 132(2):516–527, 1996.

[116] M. Wennogle and W. Hoff. Three dimensional segmentation of intravascular ultrasound data. In *Proc. 6^{th} International Conference on Image Analysis and Recognitio*, pages 772–781, Toronto, Canada, 2009.

[117] P. Wette, S. Arens, A. Elsner, and G. Domik. Extending the corkscrew algorithm to find bifurcations of vessels. In *Computer Graphics and Imaging*, 2010.

[118] A. Whale, G. P. M. Prause, S. G. Dejong, and M. Sonka. Geomatrically correct 3-d reconstruction of intravascular ultrasound images by fusion with biplane angiography: methods and validation. *IEEE TMI*, pages 686–699, 1990.

[119] C. K. Zarins, D. P. Giddens, B. K. Bharadvaj, V. S. Sottiurai, R. F. Mabon, and S. Glagov. Carotid bifurcation atherosclerosis. quantitative correlation of plaque localization with flow velocity profiles and wall shear stress. *Circulation Research*, 53:502–514, 1983.

[120] X. Zhang, C. R. McKay, and M. Sonka. Tissue characterization in intravascular ultrasound images. *IEEE TMI*, 17:889–899, 1998.

[121] X. Zhang, C.R. McKay, and M. Sonka. Tissue characterization in intravascular ultrasound images. *IEEE Transactions on Medical Imaging*, 17(6):889–899, Dec. 1998.

[122] F. Zhou and F. de la Torre. Canonical time warping for alignment of human behavior. In *NIPS*, pages 2286–2294, 2009.

[123] Jinghao Zhou, Sukmoon Chang, D. Metaxas, and L. Axel. Vascular structure segmentation and bifurcation detection. In *ISBI*, pages 872 –875, 2007.

[124] H. Zhu, K. D. Oakeson, and M. H. Friedman. Retrieval of cardiac phase from ivus sequences. In *Medical Imaging 2003: Ultrasonic Imaging and Signal Processing*, 2003.

[125] Hui Zhu, Yun Liang, and Morton H Friedman. IVUS image segmentation based on contrast. *SPIE*, 4684:1727–1733, 2002.

[126] Hui Zhu, Kevin D. Oakeson, and Morton H. Friedman. Retrieval of cardiac phase from ivus sequences. In *ISMI*, pages 135–146, 2003.

[127] Xinjian Zhua, Pengfei Zhangc, Jinhua Shaoa, Yuanzhi Chenga, Yun Zhangc, and Carlier SG Suri JS Navab N Laine AF. Abstract Jing BaiKatouzian A, Angelini ED. A snake-based method for segmentation of intravascular ultrasound images and its in vivo validation. *Ultrasonics*, 51(2):181–189, 2011.